THE ASTROPHYSICAL JOURNAL SUPPLEMENT SERIES, 72:335–386, 1990 February

EVOLUTIONARY MODELS FOR PULSATION STUDIES OF WHITE DWARFS

M. TASSOUL
6000 Chemin Deacon, Montréal, Québec
G. FONTAINE[1]
Département de Physique, Université de Montréal
AND
D. E. WINGET[2]
Department of Astronomy, University of Texas at Austin
Received 1989 February 24; accepted 1989 July 28

ABSTRACT

A large grid of equilibrium models suitable for adiabatic and nonadiabatic seismological investigations of pulsating white dwarfs of the DAV and DBV types is presented. The models are computed with the help of an evolution code which is described in detail. An interpolation code which is used to generate all the variables needed for pulsation studies and to increase, as needed, the number of shells by an interpolation technique is also described. The basic structure of the models is that of a layered configuration consisting of an almost pure carbon core surrounded by an almost pure helium layer (DB stars) itself surrounded by an almost pure hydrogen layer (DA stars). The composition transition zones are treated under the assumption of diffusive equilibrium. Some 56 different evolutionary sequences have been calculated to allow an exploration of a sufficiently large volume of parameter space. The emphasis has been put on the DAV phenomenon and the effects of various parameters on the pulsation properties of models of DA white dwarfs. Models have been computed for three masses: $M/M_{\odot} = 0.4$, 0.6, and 0.8, respectively. In addition, the helium layer mass has been varied in the range $-10 \leq \log[M(\mathrm{He})/M] \leq -2$, and the hydrogen layer mass in the range $-14 \leq \log[M(\mathrm{H})/M] \leq -4$. The effects of varying the assumed convective efficiency have been investigated by calculating models with three different versions of the mixing-length theory. This is particularly important in the context of pulsating white dwarfs because mode driving occurs near the base of the superficial convection zone associated with the partial ionization zone of the main atmospheric constituent (either H in DA stars or He in DB stars). A special sequence has been computed to explore the effects of changing the composition gradient scale height in transition regions. Furthermore, models using two different sets of radiative opacities for the same compositions have been obtained to test the sensitivity of the pulsation properties to this component of the constitutive physics. Coupled with the excellent effective temperature coverage of the instability strips provided by the evolutionary sequences, these experiments constitute, by far, the most extensive study that has been carried out to provide suitable models for pulsating white dwarfs. The equilibrium models are also of interest for and have been used in studies of meridional circulation and differential rotation in white dwarfs. They are likewise of direct relevance to the theory of the spectral evolution of white dwarfs. In particular, the models provide ideal backgrounds in which to study diffusion processes of trace heavy elements in white dwarfs. The models also bear on the question of convective mixing in DA white dwarfs, which is of interest for both the pulsating DAV stars and the spectral evolution of white dwarfs in general.

The basic cooling and structural properties of the evolutionary models are discussed extensively. It is first established that the cooling characteristics of the models compare well with those of contemporary white dwarf evolutionary calculations in the range of luminosities of interest. Advantage is next taken of the fact that several parameters have been varied to study, in a differential sense, the effects of these parameters on the cooling properties of the models. In particular, an important characteristic of white dwarf cooling is the relationship between the luminosity and the core temperature, and the effects of model parameters on this relationship are thoroughly discussed. The changing structure of the superficial convection zone, which appears as a white dwarf cools, is also discussed in the context of pulsating white dwarfs. Short of full-fledged pulsation calculations, use is made of a simple physical argument which suggests that there exists a relationship between the location of the base of the convection zone (associated with a potential driving region) and the corresponding value of the effective temperature at the blue edge of the instability strip. In this context, it is found that the expected theoretical blue edge temperature is mostly sensitive to the assumed convective efficiency, raising the possibility

[1]E. W. R. Steacie Memorial Fellow.
[2]Alfred P. Sloan Fellow.

of calibrating the mixing-length theory in pulsating white dwarfs as already claimed by our group. The evolution of the profiles of several variables is next presented in extensive graphical form for typical sequences of cooling white dwarfs. This provides typical values for these variables as well as a thorough qualitative understanding of the main features of white dwarf evolution at intermediate luminosities. Finally, a potentially very useful seismological tool for white dwarfs is discussed: asymptotic pulsation theory shows that, in a first approximation, period spacings for high-order modes should be uniform, and that the magnitudes of the spacings depend uniquely on the structural properties of a model. Asymptotic period spacings are computed for a very large number of models, their dependence on model parameters is investigated, and their usefulness as seismological probes is assessed.

Subject headings: stars: interiors — stars: pulsation — stars: white dwarfs

I. INTRODUCTION

It is now well established that single and noninteracting white dwarfs go through instability strips during their cooling history. The instabilities manifest themselves in terms of multiperiodic luminosity variations which are caused by nonradial pulsations. Typical light curves show peak-to-peak variations ranging from about 0.005 to 0.30 mag. The periods of the pulsation modes are found in the range 100–1200 s. The identification of the crucial role played by partial ionization zones in triggering nonradial pulsations has been a key ingredient in our theoretical understanding of variable white dwarfs. Indeed, it has been shown independently by several groups that the pulsation modes are driven at the base of the partial ionization zone of the main atmospheric constituent (either H or He here), and that the blue edge of the instability strip is a natural consequence of the recombination of this constituent as cooling proceeds (Winget 1981; Dziembowski and Koester 1981; Dolez and Vauclair 1981; Winget *et al.* 1982*a*; Winget and Fontaine 1982; Starrfield *et al.* 1982; Winget *et al.* 1983; Koester *et al.* 1985; Cox *et al.* 1987).

The first category of isolated variable white dwarfs (members of interacting binary systems are excluded here) has been put in evidence by the remarkable observational work carried out by McGraw (1977, 1979). The so-called ZZ Ceti stars (also named DAV in the more concise notation introduced by Sion *et al.* 1983) are, except for their variability, perfectly ordinary DA white dwarfs, i.e., stars with an almost pure hydrogen surface composition. (Those make up roughly 80% of the known white dwarf population.) Evidence is now strong in favor of the idea that the DAV instability strip corresponds to an evolutionary phase in the life of a majority of, and possibly all, DA white dwarfs (Fontaine *et al.* 1982; Greenstein 1982; Weidemann and Koester 1984; Fontaine *et al.* 1985). The latest analyses, based on *IUE* observations, locate the DAV instability strip in the range of effective temperature 13,000 K $\gtrsim T_e \gtrsim$ 11,400 K (Wesemael, Lamontagne, and Fontaine 1986; Lamontagne, Wesemael, and Fontaine 1987). By the time a cooling DA white dwarf first enters the ZZ Ceti phase, its effective temperature has dropped sufficiently low that hydrogen in the superficial layers is recombining. As mentioned previously, this partial ionization phenomenon triggers instabilities against nonradial pulsation modes in this type of star. The actual observed value of the effective temperature at the blue edge can be accounted for by adjusting appropriately the parameters of representative models (see below). By contrast, no completely convincing explanation has been put forward to account for the existence of the red edge, although several possibilities exist and have been suggested.

By direct analogy, one can expect that those white dwarfs with surface composition made of essentially pure helium—they constitute ~ 20%, or the rest of the white dwarf population—also go through an instability strip, except that helium must recombine at higher effective temperatures than hydrogen because of its much larger ionization potential. This prompted Winget (1981) and Winget *et al.* (1982*a*; see also Winget and Fontaine 1982) to *postulate* the existence of a second, hotter class of pulsating white dwarfs: the variable He-rich (DB) white dwarfs or DBV. The subsequent discovery of a DBV star with the expected characteristics (Winget *et al.* 1982*b*) was an important confirmation of both the important role played by partial ionization zones in pulsating white dwarfs and the basic validity of the equilibrium models used in the calculations. A total of six DBV stars are now known (as compared with 20 DAV objects); they empirically define an instability strip spanning the range 29,000 K $\gtrsim T_e \gtrsim$ 24,000 K according to the analyses of *IUE* observations by Liebert *et al.* (1986). The current data are consistent with the idea that *all* DB white dwarfs become unstable against nonradial pulsations in the DBV instability strip, but, because of small-number statistics, this is not yet as firmly established as in the case of DAV stars.

The existence of instability strips for white dwarfs allows us to use the powerful tools of asteroseismology for studying these stars. The DBV instability strip allows us, in principle, to probe the internal structure of relatively young white dwarfs with typical cooling times of the order of 10^7 yr. Complementary to that, the DAV strip allows us to study much older white dwarfs with typical ages of the order of 10^9 yr.[3] What is within reach, and is of particular interest here, is a determination of fundamental properties such as total mass, gravity, effective temperature, core composition, rotation rate, and masses of the outer helium and hydrogen layers which surround the core in a typical white dwarf. Recent progress in this field has been reviewed by Winget (1986, 1988), and we refer the reader to these papers for further details.

[3]There is yet a third instability strip for degenerate stars defined by the very young, variable PG 1159 (or DOV) stars, which have typical effective temperatures above 100,000 K. Kawaler (1987*a*) has recently presented an excellent review of the properties of these interesting stars. Strictly speaking, however, these objects are not fully degenerate, still contract substantially, and should be dubbed pre–white dwarfs. We will not consider them in this paper.

In order to take full advantage of the immense potential offered by white dwarf seismology, a complete exploration of parameter space for equilibrium models must be carried out. In the present paper, we report the results of an attempt at such an endeavor: a very large grid of chemically stratified models appropriate for pulsation studies of DAV and DBV stars has been computed with the help of an evolution code especially developed for that purpose. We have calculated some 56 evolutionary sequences which permit detailed explorations of the effects of various parameters on the pulsation properties of white dwarf models. Specifically, we have varied the total mass of the models, the mass of both the outer helium layer (DA and DB models) and the hydrogen layer (DA models), the assumed efficiency of convective transport (as described by mixing-length theory) in regions intimately related to partial ionization zones, the composition gradient scale height in transition regions, and the radiative opacity.

One of the most powerful tools of white dwarf seismology is the measurement of rates of period change and its eventual comparison with predicted rates obtained from evolution theory. In this context, surprisingly few investigations of pulsating white dwarfs have, so far, been carried out with *full evolutionary models*. Indeed, along with the equilibrium models used by Winget, Van Horn, and Hansen (1981) and those used by Kawaler *et al.* (1986), ours remain the only ones which were obtained from an evolution code and which have been used in published pulsation studies of white dwarfs. While the current work of M. A. Wood at the University of Texas promises a substantial improvement of the situation, *all* other investigations of the pulsation properties of white dwarfs have been based on either envelope or static stellar models.

Most of the calculations described in the present paper were done some years ago when our group started a collaborative effort aimed at understanding the pulsating white dwarfs. A subset of these equilibrium models has been used by Winget (1981), Winget *et al.* (1982*a*), Winget and Fontaine (1982), Saio, Winget, and Robinson (1983), Winget *et al.* (1983), Van Horn (1984), Fontaine, Tassoul, and Wesemael (1984), Pesnell (1987), Bradley and Winget (1987), Bradley, Winget, and Wood (1989), and Brassard *et al.* (1989) in a number of pulsation studies including nonadiabatic, nonradial, and radial investigations. Despite all these efforts, the grid of models has not yet been fully exploited, and further investigations are currently being carried out by P. A. Bradley at the University of Texas and P. Brassard at the Université de Montréal.

In addition to providing fundamental data for studies of pulsating white dwarfs, our large grid of models is being used to study further aspects of white dwarf physics. For example, our extensive exploration of parameter space allows us to study in a differential sense the effects of various parameters on the internal structure and cooling of white dwarfs. This question is discussed at some length in this paper. As part of their exhaustive study of meridional circulation and differential rotation in stars, Tassoul and Tassoul (1983) have also used some of the present models to discuss these processes in white dwarfs. Likewise, our grid of models provides the ideal theoretical framework for detailed investigations of diffusion processes of trace elements in the context of the theory of the spectral evolution of white dwarfs. Finally, the models have a lot to reveal about the conditions under which convective mixing (caused by the merging of a superficial H convection zone with a subphotospheric He convection zone) occurs in DA white dwarfs. This phenomenon is relevant both to the spectral evolution of white dwarfs and to pulsating white dwarfs, as, in the latter case, it is a possible explanation for the red edge. These issues, however, are beyond the scope of the present paper and must await the results of future investigations.

The main goals of this paper are thus (1) to describe in detail how equilibrium models appropriate for white dwarf seismology are obtained and (2) to discuss the main characteristics and properties of these models. Section II is concerned with the computational aspects of our program. The basic assumptions and simplifications used in the calculations are reviewed. Next, the salient features of our evolution code are discussed, and a detailed description of the constitutive physics is given. An interpolation scheme used to increase the number of shells (which is necessary to achieve the spatial resolution needed to study high-order pulsation modes) is also presented. The section concludes with a presentation of our grid of models in parameter space. The basic properties of our evolutionary models are discussed in § III. In particular, the cooling characteristics of typical sequences are discussed and compared with the results of other investigators. The changes on the luminosity-core temperature relation and on the cooling curve brought about by varying model parameters are also discussed. Next, the structure of the important superficial convection zones associated with regions of partial ionization is reviewed in the context of pulsating stars. The evolution of representative key variables is then presented in detail for typical sequences of cooling white dwarf models. The section ends with a discussion of a seismological tool which can be directly applied to equilibrium stellar models: the relationship between asymptotic period spacings and model parameters (cf. Kawaler 1986, 1987*b*). Finally, § IV summarizes our findings.

II. COMPUTATIONAL METHODS

a) *Basic Assumptions and Hypotheses*

The evidence gathered over the last two decades strongly suggests that the basic structure of a typical isolated white dwarf consists of a $\sim 0.6\ M_\odot$ C/O core containing most of the mass and surrounded by a thin layer of He-rich material itself surrounded, in DA stars, by an outermost layer of H-rich material. The case of the typical mass of an isolated white dwarf is particularly well documented, as a number of independent model atmosphere analyses of photometric and spectroscopic data reveal a remarkably narrow mass distribution around a mean value of $\sim 0.6\ M_\odot$ (Koester, Schulz, and Weidemann 1979; Wegner 1979; Shipman and Sass 1980; Weidemann and Koester 1984; Oke, Weidemann, and Koester 1984). Among others, Wegner (1979) has shown that the mass distribution for DA white dwarfs can be fitted with a Gaussian with a dispersion $\sigma = \pm 0.15\ M_\odot$. Weidemann and Koester

(1984) claim an even narrower mass distribution for the same stars. We have thus considered sequences with masses in the range $0.4 \leq M/M_{\odot} \leq 0.8$, which provides excellent coverage of the observed mass range.

The inference about the chemically stratified internal composition is somewhat less certain. Pulsar statistics and the presence of white dwarfs in open clusters (cf. Shipman and Green 1980; Romanishin and Angel 1980; Anthony-Twarog 1982; Weidemann 1987; Reimers and Koester 1988 and references therein) imply that white dwarfs evolve from main-sequence stars with masses less than 7–8 $M_{\odot}$. Those that have already had time to evolve into white dwarfs must have gone through hydrogen and helium core and shell-burning stages (Weidemann 1975; Weidemann and Koester 1983). Thus, the cores of typical white dwarfs are expected to be composed of the products of He burning: carbon and oxygen (see also Lamb 1974; Shaviv and Kovetz 1976; Sweeney 1976). The exact proportions of these products are still unknown because of uncertainties in the rates of He burning.

White dwarfs show spectra bearing the signature of remarkably pure atmospheric compositions: only small traces (if any) of other elements are detected in the hydrogen- (helium-) dominated atmospheres of DA (DB) white dwarfs. It is believed that gravitational settling is responsible for this phenomenon in white dwarfs (Schatzman 1958; Fontaine and Michaud 1979; Vauclair, Vauclair, and Greenstein 1979; Muchmore 1984; Paquette *et al.* 1986). Hence, the likely structure of a typical DA white dwarf consists of an almost pure H layer floating on top of an almost pure He mantle itself surrounding a C/O-rich core. There is, of course, no outer H layer in DB white dwarfs. The masses of the outer H and He layers in white dwarfs are only weakly constrained by theory to lie in the ranges $-16 \lesssim \log q(\mathrm{H}) \equiv \log [M(\mathrm{H})/M] \lesssim -4$ and $-15 \lesssim \log q(\mathrm{He}) \equiv \log [M(\mathrm{He})/M] \lesssim -2$. The lower mass limits arise from the consideration that the surface layer must be optically thick throughout the temperature range in which the white dwarfs are observed (Arcoragi and Fontaine 1980). The upper limits correspond to the maximum masses that can survive the hot, planetary nebula phase (Truran *et al.* 1977; D'Antona and Mazzitelli 1979). We note that the predictions of standard pre–white dwarf evolution theory favor only the larger values of q(H) and q(He) in young white dwarfs (cf. Iben and Tutukov 1984; Koester and Schönberner 1986). However, these predictions depend critically on assumptions about mass loss and are in strong conflict with what has been learned from studying the statistics and the abundance patterns of white dwarfs (Fontaine and Wesemael 1987), so the constraints on q(H) and q(He) have remained weak. Considering the great uncertainties in the values of q(H) and q(He) and their potential importance for the pulsation properties of models, we have decided to treat these basic quantities as essentially free parameters within the above ranges. Indeed, the hope is to *infer* the values of the masses of the outer layers of H and He from pulsation studies of white dwarfs as already claimed by Winget (1981), Winget *et al.* (1982*a*), and Winget and Fontaine (1982). Thus, despite recent progress at constraining q(H) and q(He) from spectral evolution theory (cf. Pelletier *et al.* 1986; Fontaine and Wesemael 1987; Kawaler 1988; Fontaine *et al.* 1990; Vennes *et al.* 1988; Vennes, Fontaine, and Wesemael 1989; Koester 1989), it is still appropriate here, in the context of seismological surveys, to explore the consequences of varying these parameters.

In this paper, real, chemically stratified white dwarfs are idealized by considering models in *diffusive equilibrium* consisting of an almost pure carbon core surrounded by an almost pure helium layer itself surrounded by an almost pure hydrogen layer (in the case of DA stars). For reasons of availability, there is a small admixture of heavy elements ($Z = 0.001$) in the opacity and equation-of-state tables that we have used for H, He, and C, but the effects of these heavy elements on the structure of the models are insignificant in the temperature ranges associated with the instability strips. We have not considered models with O-rich interiors which are suggested by the more efficient α-chain reaction rates of Harris *et al.* (1983). The effects of changing the interior composition of white dwarf models from pure carbon to pure oxygen have been considered recently by Wood, Winget, and Van Horn (1987) and Winget and Van Horn (1987). The pulsation properties of these O-rich models remain to be investigated.

The original motivation for the present work has been our interest in DAV stars. We have adopted the basic philosophy of computing a large enough grid of DA models suitable for a systematic exploration of the effects of free parameters on the pulsation properties of the models. To this end, and to reduce computer costs, we have concentrated on the evolutionary phases near the DAV instability strip. Thus, we have neglected plasma neutrino emission, which is the dominant cooling mechanism in the hot phases of white dwarf evolution but which is totally negligible in the DAV effective temperature range. Likewise, we have ignored the effects of crystallization—specifically, the release of latent heat and the decrease of the specific heat of the ionic system in the quantum regime which leads to the so-called Debye cooling—in our evolutionary calculations. This is again justified, since, generally, our computations would stop at $\log T_e = 3.8$, i.e., at an effective temperature significantly lower than the observed red edge (thus allowing us to study the pulsation properties of models much cooler than actual DAV stars) but just above the onset of crystallization at the center of 0.6 $M_{\odot}$, pure carbon white dwarf models according to Wood, Winget, and Van Horn (1987). For those models with relatively thin layers of hydrogen, the computations have been stopped at even higher effective temperatures when convective mixing and subsequent dilution (caused by the coalescence of an outer H convection zone with a subphotospheric He convection zone) would lead to a drastic change in the compositional character (from DA to a He-dominated atmosphere) of the stellar surface.

Using the same assumptions, and subsequently to the efforts devoted to DA models, we have also computed a grid of models suitable for pulsation studies of DBV stars. This latter grid is less extensive than the previous one, mostly because we have one less parameter [q(H)] to deal with. As in the case of DA models, we have not pursued the computations for effective temperatures below $\log T_e = 3.8$. Likewise, the calculations have also been stopped before reaching $\log T_e = 3.8$ in

cases where the outer layer of helium is so small that it becomes eventually totally convective with cooling and mixes with underlying carbon. The product of such a mixing event is an atmosphere completely dominated by carbon, i.e., a model totally inappropriate for describing a DB star. Unlike the cooler DAV objects, neutrino cooling still contributes some nonnegligible luminosity at the effective temperatures characteristic of the DBV instability strip according to Kawaler *et al.* (1986). We have neglected such residual effects on the structure of our DBV models.

In all of our models, the only sources of energy considered were remaining gravitational contraction and thermal energy release. In particular, residual burning of hydrogen (the only potent fuel in cooling white dwarfs) has been neglected. This is easily justified, since strong evidence has accumulated against the idea that DA white dwarfs retain a thick enough hydrogen layer for burning to be important at its base (see Fontaine and Wesemael 1987 for a review of this). Even the models of standard evolution theory which predict such thick hydrogen layers show that burning is quite sensitive to the exact amount of hydrogen left over from previous evolution; the models of Iben and Tutukov (1984) with $\log q(\mathrm{H}) = -3.60$ show substantial burning down to the DAV range, while the models of Koester and Schönberner (1986) with $\log q(\mathrm{H}) = -3.81$ have negligible residual burning throughout the white dwarf range. In any case, the very existence of the DAV instability strip (which can be naturally associated with a partial ionization phenomenon) indicates that residual hydrogen burning cannot be an important driving mechanism for DAV stars.

b) *The Evolution Code*

The evolution code employs the usual Henyey technique for solution of the equations describing stellar evolution. It has been adapted from the code originally developed by Tassoul (1974) for her studies of carbon-rich models of the nuclei of planetary nebulae. For greater precision, it was decided, at the outset, to include shells from the center all the way to optically thin, radiative regions as part of the stellar "interior" in the Henyey formalism. This is to be contrasted to the usual approach in which the "interior" corresponds only to the deeper, ionized regions and in which the outer, partially ionized envelope is dealt with in terms of a static "atmosphere" generally obtained by interpolation (the so-called triangle or rectangle methods). The point has some importance in the context of pulsating white dwarfs, since virtually all of the driving and most of the damping occur in the outermost, partially ionized regions. Our choice for the "interior" was further dictated by our interest in the spectral evolution of white dwarfs. Thus, the evolution code can, in principle, follow the chemical evolution of the observable layers (in the presence of convective mixing, accretion, and so on), but this feature has not been explicitly used (or needed) in the present calculations.

To describe properly the changes of the structure variables over the many orders of magnitude encountered between the center and the optically thin regions, we have adopted a particular independent (or Henyey) mass variable ξ. In terms of the mass fraction q [$\equiv 1 - M(r)/M$, where $M(r)$ is the mass interior to a sphere of radius r and M is the total mass], we have

$$q = 1 - 2.1825397\xi^3, \qquad 0 \le \xi \le 0.4, \tag{1}$$

$$q = 0.64021163 + 2.6984127\xi - 6.7460317\xi^2 + 3.4391534\xi^3, \qquad 0.4 \le \xi \le 1, \tag{2}$$

$$q = 0.031746031 e^{15(1-\xi)}, \qquad \xi \ge 1. \tag{3}$$

This choice implies that $\xi \propto M(r)^{1/3} \propto r$ near the center, and $\xi \propto -\log q$ in the outermost layers. These relationships are of interest below, where we describe an interpolation scheme aimed at increasing the number of shells of our models. We note, in particular, that both $q(\xi)$ and $q'(\xi)$ are continuous everywhere. Typically, the evolution code computes models with a number of shells in the range 160–190, with about 30–40 of these shells distributed in the deep interior (i.e., $\log q \gtrsim -2$).

In practice, we have specified the mass fraction of the outermost layer, and, in the presence of a superficial convection zone, we have changed it a few times during the evolution to make sure that it was always above the Rosseland photosphere (as defined by $\tau = \frac{2}{3}$ in the gray atmosphere approximation) or above the top of the convection zone. Thus, the last several shells of every model of interest for pulsation studies are radiative and optically thin. For our evolutionary sequences, the mass fraction in the outermost shell ranges from $\log q = -14$ to $\log q = -18$.

As usual in the Henyey technique, the surface boundary conditions are provided by an "atmosphere" strategy designed to minimize the number of calculations. In our particular case, the term "atmosphere" in the Henyey formalism is quite appropriate, since the boundary conditions are obtained by interpolating the atmospheric structure from four calculated *gray atmosphere models* forming a rectangle in the ($\log L$, $\log R$)-plane. The use of the "rectangle" method, changing the rectangle during the evolution, avoids the computation of a gray atmosphere model at each iteration and each time step. The dimensions of the rectangle are $\Delta \log L = 0.06$ and $\Delta \log R = 0.06$. The computations of the gray atmosphere models are inspired by the work of Fontaine and Van Horn (1976), but the method (originally developed for an envelope code) must be adapted to an evolution code. We give a few details here.

First, we assume that the surface of a model is characterized by a density $\rho_0 = 10^{-9}$. This corresponds to very small values of the optical depth τ_0 for all temperatures of interest here. Because τ_0 is quite small, we have approximately (for a gray atmosphere)

$$T_0 = T(\tau_0) \simeq T(0) = T_e\left[\tfrac{3}{4}s(0)\right]^{1/4}, \tag{4}$$

where T_e is the effective temperature (specified by L and R) and

$$s(\tau) = 0.7104 - 0.1331 e^{-3.4488\tau} \tag{5}$$

is the gray atmosphere relation used by Fontaine (1973).

From the equation of hydrostatic equilibrium, an appropriate estimate of the (small) value of the optical depth at the surface is

$$\tau_0 \simeq \frac{\kappa_0 P_0}{2g_0}, \tag{6}$$

where the opacity κ_0 and pressure P_0 have been obtained by interpolation in the opacity and equation-of-state tables, given the pair (ρ_0, T_0), and $g_0 = GM/R^2$ is the (constant) gravity. From the known surface quantities, the inward integration of the gray atmosphere next proceeds in terms of the independent variables (ρ, T) following the simple algorithm

$$\log \rho_{i+1} = \log \rho_i + \Delta_\rho, \tag{7}$$

$$\tau_{i+1} = \tau_i + \left(\frac{d\tau}{d \log \rho}\right)_i \Delta_\rho, \tag{8}$$

$$T_{i+1} = T_e \left\{ \frac{3}{4}\left[\tau_{i+1} + s(\tau_{i+1})\right] \right\}^{1/4}, \tag{9}$$

where the increment Δ_ρ is chosen equal to 0.05, and the derivative is given by

$$\frac{d\tau}{d \log \rho} = (\ln 10)\left\{ \frac{g_0}{P\kappa\chi_\rho} - \frac{\chi_T}{4\chi_\rho}\left[\frac{1+0.459e^{-3.4488\tau}}{\tau + s(\tau)}\right]\right\}^{-1} \tag{10}$$

In this last expression, we recognize the usual pressure derivatives $\chi_T \equiv (\partial \log P/\partial \log T)_\rho$ and $\chi_\rho \equiv (\partial \log P/\partial \log \rho)_T$, and P and κ are the local values of the pressure and opacity, respectively. Given (ρ, T), all these quantities can be directly obtained from the constitutive physics tables. At each integration step, the local mass fraction $\Delta M/M$ and radius fraction $\Delta R/R$ are computed according to the formulae

$$\frac{\Delta M}{M} = \frac{4\pi G}{g_0^2} P \tag{11}$$

and

$$\frac{\Delta R}{R} = \frac{\Delta M}{M} \frac{g_0}{2\pi G R \rho}. \tag{12}$$

These approximate expressions have been derived from the hydrostatic equilibrium equation and the mass conservation equation; they are highly accurate for the compact atmospheres characteristic of white dwarf stars. The integration of the gray atmosphere is pursued until the prespecified value of the mass fraction at the last Henyey shell, $(\Delta M/M)_s$ $(= q_s)$, is reached. At that point, corresponding to $M_s = M - \Delta M_s$, the surface boundary conditions are $P_s, T_s, r_s = R - \Delta R_s$, and L_s $(= L)$.

The initial models which are needed to begin the evolutionary calculations were taken from the work of Tassoul (1974). The models are carbon-rich stars which have evolved through the planetary nebula stage and are assumed to represent pre–white dwarfs with effective temperatures of about 10^5 K. The desired chemical composition of the outer layers is achieved by changing the surface composition to a discontinuous layered configuration in small time steps. Subsequently, the composition profile is allowed to relax into the configuration compatible with the assumption of diffusive equilibrium over several time steps. The models are then allowed to evolve until either compositional mixing or a temperature of $\log T_e = 3.8$ is encountered.

c) *Input Physics*

i) *Equation of State*

The equation of state used in the present calculations is made of three parts which apply to different regions of the (ρ, T)-plane. The first and the most critical part for pulsation studies of white dwarfs is the equation of state necessary to describe partial ionization in the envelope regions where nonideal and partial degeneracy effects are important. We have used the thermodynamic data provided by the tables of Fontaine, Graboske, and Van Horn (1977). A detailed discussion of the relevant input physics may be found in that paper. Given a chemical composition, the evolution code uses a double 3-point Lagrange scheme for interpolating thermodynamic surfaces in terms of the variables $(\log \rho, \log T)$. To reduce computer costs, we have used every other isotherm from the original grid of 54 isotherms; the resulting grid spacing is $\Delta \log T = 0.16$ and $\Delta \log \rho = \frac{1}{3}$. Composition interpolation is performed using the "additive-volume" method of Fontaine, Graboske, and Van Horn (1977) in the three composition tables. The compositions used were the Iben I [X(H) = 0.999], Iben V [X(He) = 0.999], and Weigert V [X(C) = 0.999] mixtures. Each contains a small quantity of heavy elements ($Z = 0.001$) which does not play any significant role as far as thermodynamic properties are concerned but which was considered for consistency with the opacity tables (see below).

The second part of the equation of state is necessary at the hot end of the evolutionary sequences where atmospheric densities become smaller than the low-density limits of the skewed tables of Fontaine, Graboske, and Van Horn (1977). In particular, these tables do not extend to the assumed surface density of $\log \rho = -9$ for $\log T \geq 3.70$. For these monoelemental low-density regions, we have therefore used a simple analytic treatment of the equation of state for a mixture of radiation and an ideal, nondegenerate, partially ionized gas of pure hydrogen (or pure helium for the DB models). This analytic treatment based on the Saha equations is perfectly appropriate for densities lower than those covered by the tabular data of Fontaine, Graboske, and Van Horn (1977), which is fundamentally why these tables have not been extended to lower densities. Not surprisingly, the analytic model matches extremely well the tabular data for both hydrogen and helium at the low-density edges of the tables.

The third part of the equation of state is used for the completely ionized, degenerate stellar interior. In this region, analytic fits are used, with the switch from the tabular data to

the analytic formulae performed at the high-density and high-temperature edges of the equation-of-state tables of Fontaine, Graboske, and Van Horn (1977), i.e., for $(\rho/\mu_e)^{2/3} > 10^{-4}T$ or $\rho > 10^5$, and $T > 10^{7.54}$. The pressure and the internal energy are, respectively, written as

$$P = P_{\rm el} + P_{\rm ion} + P_{\rm Coul} + P_{\rm rad}, \tag{13}$$

and

$$U = U_{\rm el} + U_{\rm ion} + U_{\rm Coul} + U_{\rm rad}, \tag{14}$$

where the subscripts "el," "ion," "Coul," and "rad" indicate the electronic, ionic, Coulombic, and radiative contributions, respectively. Given P and U, all other thermodynamic quantities can of course be derived. $P_{\rm el}$ and $U_{\rm el}$ are given by the fits of Bodenheimer *et al.* (1965). The derivatives with respect to ρ and T are taken from the formulae of Beaudet and Tassoul (1971). These fits are valid over the entire (ρ, T)-plane corresponding to complete ionization, from complete degeneracy to nondegenerate regions, and from nonrelativistic to fully relativistic regions. Following standard notation, the ionic and photon contributions are given by

$$P_{\rm ion} = \frac{N_0 k \rho T}{\mu_i} = \frac{2}{3} U_{\rm ion}, \tag{15}$$

$$P_{\rm rad} = \frac{4\sigma}{3c} T^4 = \frac{1}{3} U_{\rm rad}, \tag{16}$$

with

$$\frac{1}{\mu_i} = \sum_j \left(\frac{X_j}{A_j} \right) \equiv \frac{1}{\langle A \rangle}, \tag{17}$$

where the summation is taken over the ionic species of mass fraction X_j and atomic weight A_j. The only nonideal term considered here, the Coulombic contribution, is treated in an approximate way following Koester (1976; see also Van Horn 1968). We write

$$\frac{P_{\rm Coul}}{P_{\rm ion}} = \frac{U_{\rm Coul}}{2U_{\rm ion}} = \frac{-0.3\Gamma^{3/2}}{\Gamma^{1/2} + 1.03921}, \tag{18}$$

where Γ is the usual Coulomb parameter,

$$\Gamma = 2.275 \times 10^5 < \frac{Z^2}{A^{1/3}} > \frac{\rho^{1/3}}{T}. \tag{19}$$

The adiabatic exponents are evaluated from the relations

$$\Gamma_1 = \left[\frac{\beta + (4 - 3\beta)^2}{\beta + 12(\gamma_1 - 1)(1 - \beta)} \right] (\gamma_1 - 1), \tag{20}$$

where

$$\beta = \frac{P_{\rm el} + P_{\rm ion} + P_{\rm Coul}}{P} \tag{21}$$

and

$$\gamma_1 = \frac{\Gamma_{1e} P_{\rm el} + (5/3) P_{\rm ion} + (4/3) P_{\rm Coul}}{P_{\rm el} + P_{\rm ion} + P_{\rm Coul}}, \tag{22}$$

with Γ_{1e} given by the analytic fit of Beaudet and Tassoul (1971). Γ_3 and $\nabla_{\rm ad}$ are evaluated from the expressions

$$\Gamma_3 = \frac{P(\partial \log P/\partial \log T)_\rho}{U(\partial \log U/\partial \log T)_\rho} + 1, \tag{23}$$

$$\nabla_{\rm ad} = \frac{\Gamma_3 - 1}{\Gamma_1}. \tag{24}$$

Not surprisingly, the match between the tabular data and the analytic fits used to describe the high-density, high-temperature regime is not as good as the match between the first and second parts of our equation of state at the low-density edges of the tables. While the pressure and the energy match very well, higher order thermodynamic quantities such as derivatives, adiabatic exponents, and specific heats can show differences up to several percent. These differences do not affect at all the construction of the models.

In keeping with the main goals of the present investigation, we have not used the detailed tabular equation-of-state data developed by Lamb (1974) for a completely ionized, pure carbon plasma under conditions appropriate for the deep interior of white dwarfs. Although available to us, these data are necessarily much slower to use than analytic fits. What is more important from the point of view of pulsation studies, however, is to recognize that the essential contribution of the interior equation of state is to specify in large part the *mechanical structure* of a model, to which pulsation modes are quite sensitive. Because the pressure is totally dominated by the contribution of the ideal, highly degenerate electron gas in the deep interior of a white dwarf, and because our analytic fits for this leading term are quite accurate, we can expect our equation of state to be perfectly adequate for constructing models of pulsating stars. At the same time, we note that our rather rough treatment of the interacting ion system as compared with the work of Lamb (1974) can be expected to lead to differences in thermal properties, such as specific heats, for example. While the pulsation modes are not sensitive to the behavior of the ions in the deep interior, other properties of the models such as cooling time scales can be affected. Note that uncertainties introduced in this way do not become important until after crystallization takes place, by which time we have stopped our computations. This is discussed further in § III*a*).

ii) *Opacities*

The total opacity has been computed as usual from the radiative and conductive opacities,

$$\frac{1}{\kappa} = \frac{1}{\kappa_r} + \frac{1}{\kappa_c}. \tag{25}$$

In the atmospheres and envelopes two sets of radiative opaci-

ties have been employed. For most of the sequences, data kindly provided to us by Huebner (1980) were used. These opacities were computed using the Los Alamos Opacity Library Program for the Iben I, Iben V, and Weigert V compositions. Because these newer data do not extend to temperatures below 12,000 K, we have supplemented them as necessary with the older Cox and Stewart (1970) opacities for the same mixtures at low temperatures. In addition, we have also computed several evolutionary sequences using the full tables of Cox and Stewart (1970) in order to explore the consequences of radiative opacity uncertainties. Quadratic interpolation (a double 3-point Lagrange scheme) has been used to obtain $\log \kappa_r$ for a given pair $(\log \rho, \log T)$ and for a given composition. For the same composition, the total opacity is obtained according to equation (25) by including the conductive opacity obtained from the analytic fits given by Fontaine and Van Horn (1976). Those fits are based on the calculations of Hubbard and Lampe (1969) for pure H, He, and C plasmas. In composition transition zones, a simple linear formula in terms of the mass fractions of the elements was used to interpolate between compositional tables.

In the deep, completely ionized carbon interior (corresponding to the third part of the equation of state as described above), the radiative opacity is computed from the approximate formulae given by Bodenheimer *et al.* (1965) and Beaudet and Salpeter (1969), which include the effects of electron scattering at high temperatures. A precise description of the radiative opacity is not necessary because the opacity is completely dominated by the strong conductivity of degenerate electrons in this regime. For this case, the analytic fits of Lamb (1974) based on the Hubbard and Lampe (1969) data for pure carbon are used. The validity of these fits extends into the relativistic regime, while the analytic fits of Fontaine and Van Horn (1976) do not.

We have not considered the effects of using the newer conductive opacities computed by Itoh *et al.* (1983, 1984), since these were not available to us at the time our calculations were performed. These are further dimensions, along with the effects of changing the interior composition as discussed above (almost pure carbon is assumed here), which must be eventually added to the region of parameter space explored in the present investigation.

iii) *Composition Transition Zones*

The composition transition zones are regions of continuously varying composition which separate the various compositional layers. Thus, for DA models, there are two composition transition zones: the H to He and the He to C buffer regions. In the vast majority of white dwarf evolutionary calculations carried out so far, these transition zones are treated in a very crude way: the abundance profiles at the composition buffer regions are considered completely discontinuous. Of course, ordinary diffusion induced by the very large artificial concentration gradients at such interfaces would instantaneously smooth the abundance profiles there. Hence, models with discontinuous transition zones must be considered as an extreme theoretical description of layered white dwarfs.

In the present paper we have adopted another extreme, and quite opposite, point of view, i.e., we assume that the abundance profiles in the transition zones are specified by the condition of *diffusive equilibrium* between the processes induced by the gravitational and electric forces (this is globally known as gravitational settling) and those induced by the concentration gradient (ordinary diffusion). The assumption of equilibrium was based upon the results of diffusion time scale estimates in white dwarfs which suggest that complete sorting is possible over the cooling ages of white dwarfs (e.g., Fontaine and Michaud 1979). These suggestions are largely borne out by recent, actual time-dependent calculations of diffusion processes in evolving white dwarfs (Pelletier 1986; Pelletier *et al.* 1986; Vennes *et al.* 1988; and unpublished work by C. Pelletier). Such calculations show that diffusive equilibrium can indeed be reached in layered white dwarf models, especially in the outermost layers of the cooler (older) objects. At the same time, however, it appears that the separation process is not yet completed at large depths ($\log q \gtrsim -3$) for ages characteristic of the DAV stars. We have nevertheless assumed here that diffusive equilibrium applies throughout our models.

We have used the equations developed by Arcoragi and Fontaine (1980) to describe diffusive equilibrium. The reader will find all the details of the method in that reference. Briefly, however, the stellar plasma in a composition transition zone is assumed to consist of *two* ionic species of average charge Z_1 and Z_2. Thermal diffusion and radiative forces are neglected (which is justified in the present context; see Fontaine and Michaud 1979 and Paquette *et al.* 1986), and the only mechanisms of importance are gravitational settling and ordinary diffusion. The condition of equilibrium is obtained by requiring that the relative diffusion velocity of ions of species 2 (the heavy element) with respect to ions of species 1 (the light element) vanishes everywhere. This leads to equation (A5) of Arcoragi and Fontaine (1980), which gives the equilibrium concentration profile for element 2 (and consequently that of element 1, since we are dealing with a two-ion plasma). Basically, the equilibrium abundance is a unique function of the local pressure, as can have been expected from balancing gravitational settling and ordinary diffusion.

Equation (A5) of Arcoragi and Fontaine (1980) cannot be directly implemented in an evolution code. A first transformation from the pressure to a mass variable is necessary because our independent variable is the Henyey quantity ξ defined previously. This transformation is easily done, since the mass fraction $q\ [= q(\xi)]$ is directly proportional to the pressure P in a large part of the envelope of a white dwarf (see, for example, § III*b*). We next approximate the solution given by equation (A5) of Arcoragi and Fontaine (1980) by dividing the transition zone into two parts: an upper one in which element 1 is dominant and element 2 is considered as a trace, and a lower one in which the roles of the respective elements are reversed. The idea here is to match together two very *simple* solutions obtained under the assumption of trace elements instead of using the exact but much more cumbersome nonlinear equation (A5). From equation (A6) of Arcoragi and Fontaine (1980), we then find that the abundance profile of element 2 (considered as a trace) in the upper part of the

transition zone is given by

$$\frac{\partial \ln c_2}{\partial r} = \alpha_2 \frac{\partial \ln q}{\partial r}, \tag{26}$$

with

$$\alpha_2 = \frac{A_2}{A_1}(1+Z_1) - Z_2 - 1. \tag{27}$$

Similarly, the abundance of element 1 (considered as a trace) in the lower part of the transition zone is given by

$$\frac{\partial \ln c_1}{\partial r} = \alpha_1 \frac{\partial \ln q}{\partial r}, \tag{28}$$

with

$$\alpha_1 = \frac{A_1}{A_2}(1+Z_2) - Z_1 - 1. \tag{29}$$

In these expressions, c_i [$\equiv n_i/(n_1+n_2)$] is the number concentration of element i, r is the radial coordinate, q is the mass fraction, and A_i (Z_i) is the atomic weight (average charge evaluated at the middle of the transition zone) of element i ($i=1,2$). At each instant, the abundance profiles are given by the solution of equations (26) and (28):

$$c_2 = k_2 q^{\alpha_2} \quad \text{(upper region)}, \tag{30}$$

$$c_1 = k_1 q^{\alpha_1} \quad \text{(lower region)}. \tag{31}$$

The integration constants k_1 and k_2 are determined by the condition of continuity in the middle of the transition zone, which we choose as the mass fraction q_m where the abundances of the two elements are the same. Thus, we obtain

$$k_2 q_m^{\alpha_2} = k_1 q_m^{\alpha_1} = \tfrac{1}{2}. \tag{32}$$

The problem is closed by determining the exact value of q_m. This is done by invoking the mass conservation of element 1 (say), which leads to the condition that the integral over the entire distribution of element 1 (both above and below the middle point) must be equal to a known, prespecified value of the mass of element 1 in the model.

In practice, for DA models, the total mass fractions of hydrogen, q(H), and helium, q(He), are specified. Following the procedure just described, q(H) is used to locate the middle of the H/He transition zone, q_m(H/He), and similarly, q(He) is used to locate the middle of the He/C transition zone, q_m(He/C). The abundance profiles are then directly given in terms of our independent variable ξ via $q(\xi)$ and equations (30), (31), and (32). During the evolution q_m(H/He) and q_m(He/C) do not change very much; small effects are observed as the consequence of slight changes in the equilibrium conditions brought about by slight changes in the average charges Z_1 and Z_2 as a result of cooling (see § III*b*). Note that we have not assumed complete ionization of the ionic species in the composition transition zones. Instead, Z_1 and Z_2 are evaluated consistently from the equation-of-state tables for the conditions encountered within the transition zones.

Our description of diffusive equilibrium leads to transition zones which are relatively broad. In actual calculations, the zones correspond to those regions where the abundances (c_1, c_2) of the two ionic species are larger than 10^{-3}. Number abundances less than this value were set to zero. Typically, the H/He buffer zone would cover about 1.5 decade in q, while the He/C buffer zone would be somewhat broader, covering about 2 decades in q (the differences in equilibrium profiles for various ionic species can be appreciated from Fig. 7 of Arcoragi and Fontaine 1980). Because our technique can handle only two-ion plasmas and not multi-ionic mixtures, we have always made sure that the H/He and He/C transition zones would not overlap in our DA models. This was achieved by choosing q(He) *at least* 2 orders of magnitude larger than q(H). There are, in addition, a number of observational and theoretical arguments which favor this choice.

The fundamental importance of the composition transition zones in the context of pulsating white dwarfs is their influence on the Brunt-Väisälä frequency N, which is defined as

$$N^2 = -g\left(\frac{d \ln \rho}{dr} - \frac{1}{\Gamma_1}\frac{d \ln P}{dr}\right), \tag{33}$$

where all symbols have been identified previously. Any sharp feature or quasi-discontinuity in N^2 as a function of depth in a stellar model corresponds to a region where eigenmodes can potentially be pinched and filtered. In particular, the transition zones produce relatively narrow features in the profile of the Brunt-Väisälä frequency which are responsible for the main filtering capability of stratified white dwarf models. As first shown by Winget, Van Horn, and Hansen (1981), only a few modes (known as trapped modes) out of the extremely rich g-mode spectrum can actually resonate with the H and He layer thicknesses in a given model. Because these modes are the more likely to be excited, the phenomenon of mode trapping leads to a potentially extremely powerful seismological tool. Thus, the period structure of a stratified white dwarf model is dominated by mode trapping which is caused by resonances with the compositional layers. An appropriate description of mode trapping in white dwarfs therefore requires a study of the composition profiles in the transition zones.

It is useful, and even essential in the core of a degenerate star (cf. Brassard *et al.* 1990), to transform equation (33) in order to obtain reliable values for N^2. It can be shown that equation (33) can be rewritten in the form

$$N^2 = \frac{g^2\rho}{P}\frac{\chi_T}{\chi_\rho}(\nabla_{\rm ad} - \nabla + B), \tag{34}$$

with

$$B = -\left(\frac{\partial \ln P}{\partial \ln Y}\right)_{\rho,T}\frac{d \ln Y}{d \ln P}\frac{1}{\chi_T}, \tag{35}$$

where ∇_{ad} is the adiabatic temperature gradient, ∇ is the actual temperature gradient, and Y is the mass fraction of one element in a two-ion buffer zone. Written in this form, the contribution of a transition zone to the Brunt-Väisälä frequency is made explicit; it is contained in the variable B. This quantity is always positive and assumes (in the presence of diffusive equilibrium) nonnegligible values only in regions where the abundances of two ionic species are comparable, i.e., in the composition transition zones.

The form of equation (34) also underlines the well-known intimate relationship between the Brunt-Väisälä frequency and the Ledoux criterion for convective stability. However, in the present case, the mean molecular weight μ, which is the usual variable appearing in the Ledoux criterion, is not appropriate. This is because partial ionization regions can sometimes overlap with transition zones in our models, which causes μ to vary not only with composition there but also with varying ionization as a function of depth. The difficulty is easily removed by replacing μ by *any* variable which measures *only* a change in chemical composition; the functional form of equation (35) is the same as that of the term involving μ in the Ledoux criterion. We have chosen Y, the mass fraction of helium, as the new variable; this choice has the advantage of being relevant to both transition zones in DA models. The computation of B is then straightforward: $(\partial \ln P/\partial \ln Y)_{\rho,T}$ is obtained by differencing in composition in the equation-of-state tables, $d \ln Y/d \ln P$ is obtained numerically from the actual composition profile, and χ_T is again an equation-of-state variable.

iv) *Treatment of Convection*

As in any other type of star, superficial convection zones in white dwarfs are closely related to partial ionization zones. In a cooling white dwarf, superficial convection always develops as the result of the recombination of the main atmospheric constituent; the profile of such a convection zone becomes, in fact, an almost perfect tracer of the extent of the partial ionization zone of this constituent (Fontaine and Van Horn 1976). It is near the base of the superficial convection zone that the radiative luminosity starts being modulated when a white dwarf enters an instability strip. Hence, the exact location of the base of the convection zone is critical in terms of potential driving of pulsation modes. Because we have to rely on the mixing-length theory with its intrinsic limitations, we can expect the location of the base and, in general, the whole extent of the convection zone to be uncertain. This, in turn, implies that the derived pulsation properties of a white dwarf model can be sensitive to the assumed convective efficiency. (In fact, Winget *et al.* 1982*a* and Winget *et al.* 1983 have shown that the theoretical blue edges of both the DAV and the DBV instability strips are quite sensitive to the convective efficiency.) Thus, one of the most crucial dimensions in our exploration of parameter space is to investigate the effects of changing the convective efficiency within the framework of the mixing-length theory.

To this end, we have computed different evolutionary sequences using three different versions of the mixing-length theory. The first one, referred to here as ML1, is the standard version due to Böhm-Vitense (1958). In this version, the mixing length is chosen equal to 1 local pressure scale height. Our ML2 version is due to Böhm and Cassinelli (1971); the mixing length is again chosen equal to 1 local pressure scale height. The ML1 and ML2 theories differ only in the choice of the numerical constants a, b, and c which appear in the following well-known equations (cf. Cox and Giuli 1968) for the average speed of a convective cell,

$$v_c^2 = \frac{al^2 gQ(\nabla - \nabla')}{H_P}, \tag{36}$$

the average convective flux,

$$F_c = \frac{b\rho v_c C_P T l(\nabla - \nabla')}{H_P}, \tag{37}$$

and the convective efficiency (in a medium without energy sources),

$$\frac{\nabla - \nabla'}{\nabla' - \nabla_{ad}} = \frac{C_P \rho^2 l v_c \kappa}{c\sigma T^3}, \tag{38}$$

where the symbols are standard. Böhm-Vitense (1958) gives $a = \frac{1}{8}$, $b = \frac{1}{2}$, and $c = 24$, whereas Böhm and Cassinelli (1971) use $a = 1$, $b = 2$, and $c = 16$. The ML2 version essentially amounts to reducing the horizontal energy loss rate and thereby increasing the convective efficiency relative to the ML1 approach. Our third version, ML3, assumes an even greater convective efficiency; we use the same constants a, b, and c as in the ML2 version, but this time we take the mixing length as equal to 2 local pressure scale heights.

In the solution of the energy transport problem, we have used the usual Schwarzschild criterion ($\nabla_{rad} < \nabla_{ad}$) to determine the convective stability of a given shell. Arguments could be put forward that in composition transition zones the Ledoux criterion should be used instead. For reasons related to partial ionization as discussed above, this would have to be a modified criterion, however, because μ is not an appropriate variable to use under the present circumstances. A criterion inspired from equations (34) and (35) could be used. On the other hand, one can argue that convective instability still develops if $\nabla_{rad} > \nabla_{ad}$ *even* in the presence of composition gradients. In the case of interest, the composition gradients in the H/He and He/C transition regions lead to the term B in the Ledoux criterion. As indicated previously, this term is positive and has a stabilizing effect often referred to as the μ-barrier effect. (Note that the case $B < 0$ is always unstable and corresponds to the Rayleigh-Taylor instability.) It is important to realize, however, that the stabilizing effect of B (> 0) is to be understood in the following sense: Instead of moving indefinitely away from its equilibrium position when $\nabla_{rad} > \nabla_{ad}$, a perturbed parcel of matter (in the picture of the mixing-length theory) actually oscillates about this position in a medium with $B > 0$, *but the amplitude of oscillation increases with time*. This is sometimes referred to as overstability. In practice, this oscillatory motion with increasing amplitude must eventually lead to an instability. For this reason, we have adopted the Schwarzschild criterion throughout our

models. Further arguments in favor of this choice are presented in Spiegel (1969, 1972; see also Kato 1966).

The question of convective mixing is more subtle because the instability (as defined by the Schwarzschild criterion) is linear and local in nature, whereas mixing is nonlinear and nonlocal. Indeed, convective mixing modifies the distribution of temperature, density, and opacity, which may change the stability of the layers of interest. Hence, in practice, it is necessary to use an iteration technique to obtain a self-consistent model in which the mixed region corresponds exactly to the layers where the Schwarzschild criterion indicates convective instability. Under certain circumstances, a self-consistent solution is not even possible, and one must deal with the phenomenon of semiconvection and partial mixing.

In the interest of simplicity, we have not attempted to describe convective mixing in our evolutionary models. Thus, we have generally stopped the calculations in those cases where a superficial H convection zone would merge with a subphotospheric He convection zone (DA models), or in those cases where a superficial He convection zone would merge with a subphotospheric C convection zone (DB models). This procedure is certainly justified on the grounds that the resulting mixed models have surface compositions dominated by helium (former DA stars) or carbon (former DB stars), and are no longer appropriate for studies of the DAV and DBV phenomena. At the same time, however, this procedure has introduced a small inconsistency in *some* of our models suitable for a study of these phenomena. Indeed, for DA models with relatively thin outer layers of hydrogen, a subphotospheric convection zone caused by partial ionization of helium generally appears below the H/He transition zone. (A similar situation occurs in DB models with thin He layers in which a subphotospheric carbon convection zone develops.) The inconsistency arises because the top of this subphotospheric convection zone is located in the lower part of the H/He transition zone where the H abundance is still nonnegligible. Thus, in principle, convection would mix the lower region of the H/He transition zone, thereby changing the abundance profiles which have been obtained under the assumption of diffusive equilibrium. A self-consistent solution as discussed above would be necessary in such a case. By ignoring these complications, we have introduced an inconsistency in models with thin outer layers. However, we find that the fraction of the flux carried by convection in the subphotospheric convection zones of these models is generally very small. As a consequence, the structure of the models in the transition zones cannot be strongly affected by the presence of these convection zones. We thus feel perfectly comfortable with the slight inconsistency just described.

d) *The Interpolation Code*

To prepare data files suitable for pulsation studies, it was found more efficient to compute the evolutionary sequences first and keep, from these computations, a minimum amount of data in the form of disk files. This is primarily because pulsation calculations require the knowledge of a large number of variables that are obtainable from the constitutive physics but are not directly involved in the evolutionary calculations as such. The explicit computations of these variables would slow down the evolution code considerably. In addition, it was found that the evolution of our white dwarf models is accurately described with models having, typically, 160–190 shells, but that this number of shells is insufficient for providing the resolution necessary to study high-order pulsation modes. For example, our experience with pulsation codes shows (cf. Brassard *et al.* 1990) that the adiabatic period of a pulsation mode of a DAV model can be obtained within an accuracy better than 1% for all gravity modes with $l=1$, 2, and 3 and in the period range 100–1000 s, provided that the model has about 600 shells or more. Hence, it is necessary to devise an interpolation scheme aimed at increasing the number of shells, particularly for the high-order modes. As the accuracy requirement may vary from one application to another, our approach allows us to build models with a variable number of shells as necessary, without having to recompute a full evolutionary sequence each time. We thus describe briefly an interpolation code whose main function is to generate data files usable by pulsation programs. Improvements over the original version of the interpolation code used in the pulsation studies of Winget (1981), Winget *et al.* (1982*a*), and Winget *et al.* (1983) have been made and are included in the present discussion.

Let us discuss first the interpolation strategy. We have experimented with a number of interpolation techniques and have found out that *independent* interpolation of most (but not all) variables in terms of an appropriate interpolant are satisfactory. Ideally, from the point of view of pulsation theory, the mesh distribution should be uniform in terms of the quantity x [$\equiv \ln(r/P)$], which is usually the independent variable used in pulsation codes based on a generalized Newton-Raphson technique. However, x is not a mass variable, and its divergent behavior near the center of a model makes that quantity unsuitable for evolutionary calculations. Although it is possible to use x as the interpolant for generating data files for pulsation studies (and thus obtain a uniform mesh in terms of that quantity), it is actually best to retain the original shells in the data to be processed. This is because, to the accuracy of the evolutionary calculations, the structure equations are guaranteed to be satisfied at those shells, while they are not satisfied at interpolated shells. We find our Henyey variable ξ to be a most useful interpolant in this context. At the same time, this choice implies that the mesh distribution is not (and cannot be) uniform in terms of x throughout our models. Note that this desired uniformity is not strictly demanded by pulsation codes but represents an efficient way of distributing shells in such codes. For this reason, we made the grid spacing as uniform as possible in terms of x within the constraints imposed by our evolutionary models. In this spirit, our choice of ξ as the interpolant is a judicious one because, in the envelope of a model (i.e., for $\log q < -1.498$ according to eq. [31]), we have $\xi \propto -\log q$. In these outermost layers, $r \simeq R =$ constant approximately, $P \propto q$, and $x \propto -\log q$ also, which means that the mesh distribution in terms of x is, in fact, essentially uniform there. This direct scaling between ξ and x is, of course, invalid in the core.

With two exceptions, independent interpolations in terms of ξ have been carried out for all the variables. We have made

some efforts to achieve a higher level of consistency for the mechanical structure equations because the pulsation periods are most sensitive to the mechanical structure. This has some importance because some of the variables used in pulsation codes must satisfy known central boundary conditions and behaviors which are directly related to the mechanical structure. Moreover, because of the divergent nature of x near the center, a relatively large number of shells (typically 20) must be inserted between the center and the first shell of an evolutionary model in order to ensure a grid spacing as uniform as possible in x. Obviously, a correct behavior of the pulsation variables is highly desirable in these extra shells. To this end, we have interpolated in an independent way the pressure P and the density ρ (these are well-behaved quantities in white dwarfs, particularly near the center, where their derivatives with respect to ξ vanish), while the radial coordinate r is derived from an interpolation involving the mechanical structure equations. From the equations of hydrostatic equilibrium and of mass conservation, we get

$$\frac{dM}{dP} = -\frac{4\pi r^4}{GM(r)}. \tag{39}$$

This quantity is interpolated in terms of ξ, which, as the interpolant, reveals another useful property here. And indeed, we find that $dM/dP \propto \xi$ near the center of a model, thus ensuring that the interpolated values of dM/dP are correct there. The interpolation of the function dM/dP also becomes quite reliable in the outer envelope as dM/dP tends toward a constant. After the interpolation of dM/dP, the values of r are obtained by isolating r in equation (39), $M(r)$ being directly related to ξ.

We have followed a similar philosophy for the radiative luminosity $L_{\rm rad}$. This variable must obey the boundary condition $L_{\rm rad} \to 0$ as $\xi \to 0$. However, if we expand about the center, we find that $L_{\rm rad}$ is *not* directly proportional to r (or ξ), which implies that an interpolation of $L_{\rm rad}$ in terms of ξ in the central regions does not give the right behavior. This problem is easily solved by remembering that, to a high level of approximation, $L_{\rm rad} \propto M(r)$ in the core of a white dwarf. Thus, we interpolated the ratio $L_{\rm rad}/M(r)$, which is nearly a constant throughout a model (except for convective regions). The radiative luminosity is eventually derived from this ratio, $M(r)$ being once again directly related to ξ.

Before interpolating the required variables as such, the interpolation code performs a number of needed operations. First, it uses the minimal data generated by the evolution code to compute (or recompute in some cases) all the required variables in a way absolutely consistent with that used in the evolution code, since the same block of constitutive physics subroutines is used. The interpolation code also recomputes explicitly new opacity derivatives $[(\partial \log \kappa/\partial \log \rho)_T$ and $(\partial \log \kappa/\partial \log T)_\rho]$ with a higher order numerical scheme (a 3-point Lagrange technique). In the evolution code, the opacity derivatives (only needed in the convergence process) are evaluated in a cruder way, using a 2-point forward (not centered) difference scheme. This latter scheme leads to some artificial structure in the opacity derivative surfaces, which may introduce some unwanted noise in nonadiabatic pulsation calculations. In § III we compare opacity derivatives of two sequences of models, each using one or the other of the numerical schemes.

The next task performed by the interpolation code is to delete some original shells which are very closely spaced with respect to one another. These closely spaced shells are simply the results of the evolution code, which requires, for example, that the changing location of a convection zone be kept track of, or that extra shells be added during convergence difficulties, and so on. The evolution code not only adds shells but also deletes some, but the end product is usually a shell distribution which shows bunching. We eliminate closely spaced shells in order to facilitate the use of spline interpolation. In practice, no adjacent shells closer than $|\Delta \log q| = 0.006$ are tolerated. This implies the elimination of some 10–15 shells out of the original 160–190 shells. The interpolation code then smooths locally the variables which show some discontinuities deep in the stellar interior where the equation of state switches from the tabular data (second part; see discussion above) to the high-density, high-temperature analytic fits. This step is not fundamental, since we are dealing with the very deep interior where eigenmodes may have only very small amplitudes, but is taken as a precaution against the occurrence of artificial features which may nevertheless affect a quantity such as the Brunt-Väisälä frequency. The smoothing recipe is quite straightforward, as a simple filter is passed over 10 shells (five shells above and five below) which overlap the equation-of-state transition region.

The next step is to define a finer mesh to increase the number of shells. The interpolated models that are presented in this paper, have, typically, 630–650 shells (including 150–175 original ones), but, quite clearly, this is not restrictive. For the present models, then, we have first divided the interval between the center and the first original shell into 20 smaller intervals uniform in $\Delta\xi$. We have then considered the spacing Δx between the first and second original shells expressed in terms of the pulsation variable x. If the spacing was less than 0.09, we would go to the next interval, i.e., the one between the second and third original shells. If the spacing was larger than 0.09 but smaller than 0.18, we would divide the interval into two smaller intervals uniform in $\Delta\xi$. If the spacing was larger than 0.18 but smaller than 0.27, we would divide the interval into three smaller intervals uniform in $\Delta\xi$, and so on. This procedure was repeated for all original shell intervals up to the surface. In this way, although the interpolation was carried in terms of ξ, we still get a fairly uniform distribution in terms of x, the variations of Δx never exceeding 30% from the mean value. (This excludes, of course, the central point itself not used in pulsation calculations and where x becomes infinite.)

The interpolation code finally carries out the interpolation of the variables on this finer mesh. Cubic spline interpolation with the independent variable ξ is used for most variables. This technique, however, is not appropriate for the variables which show discontinuities in their profiles (e.g., the radiative luminosity across convection zones) because Gibbs noise is generally generated at those discontinuities. In these cases, we have simply used a linear interpolation technique. Table 1 gives a list of the 21 variables generated by the current version

TABLE 1

BASIC VARIABLES FOR PULSATION STUDIES

Variables (1)	Interpolated Quantity (2)	Interpolation Scheme (3)	Smoothing (4)
Mass fraction	$(\log q)$	Computed directly from ξ	No
Radius	Derived from dM/dP	Spline	No
Mass within radius r	$(M(r))$	Computed directly from ξ	No
Radiative luminosity	Derived from $L_{\rm rad}/M(r)$	Linear	No
Temperature	$\log T$	Spline	No
Density	$\log \rho$	Spline	No
Pressure	$\log P$	Spline	No
Specific heat at constant volume	$\log C_V$	Spline	Yes
Pressure derivative	χ_ρ	Spline	Yes
Pressure derivative	χ_T	Spline	Yes
Opacity derivative	$(\partial \log \kappa/\partial \log \rho)_T$	Spline	Yes
Opacity derivative	$(\partial \log \kappa/\partial \log T)_\rho$	Spline	Yes
Temperature gradient	∇	Spline	Yes
Adiabatic temperature gradient	$\nabla_{\rm ad}$	Spline	Yes
Opacity	$\log \kappa$	Spline	Yes
Helium mass fraction	Y	Spline	No
Mixing length	l	Spline	No
Convective flux	F_c	Linear	No
Convective velocity	v_c	Linear	No
Ledoux term	B	Linear	No
Brunt-Väisälä frequency squared	N^2	Linear	Yes

NOTE.—See text for explanation of table.

of the interface code. Column (2) indicates which quantity is actually interpolated (logarithmic variables can be quite useful here), column (3) says which of the interpolation techniques (linear or spline) is used, and column (4) shows whether the smoothing filter has been applied or not across the equation-of-state transition region. From the listed variables, *all* quantities needed for both adiabatic and nonadiabatic pulsation studies can be directly obtained. In the next section we present graphic representations of the evolution of these variables in typical cooling white dwarfs.

In ending this subsection, it is appropriate to discuss briefly the "performance" of the interpolation scheme. For reasons given above, we again concentrate on the mechanical structure equations. Specifically, we have computed for various typical models the quantities

$$\sigma(P) \equiv \sum_{i=1}^{N} \left| \frac{(dP/dr)_{\rm num} + \rho g}{-\rho g} \right|_i \Big/ N \qquad (40)$$

and

$$\sigma(M) \equiv \sum_{i=1}^{N} \left| \frac{(dM/dr)_{\rm num} - 4\pi r^2 \rho}{4\pi r^2 \rho} \right|_i \Big/ N, \qquad (41)$$

where N is the number of shells in a model and $(dP/dr)_{\rm num}$ and $(dM/dr)_{\rm num}$ are evaluated at each shell using some algorithm to obtain the numerical derivatives on the mesh distribution. The quantities $\sigma(P)$ and $\sigma(M)$ correspond simply to the average absolute deviations from the hydrostatic equilibrium equation and the mass conservation equation, respectively, and are global measures of the degree of consistency of a model. Three different algorithms have been used for evaluating $(dP/dr)_{\rm num}$ and $(dM/dr)_{\rm num}$: a 2-point centered difference [e.g., $(P_{i+1} - P_{i-1})/(r_{i+1} - r_{i-1})$], a 3-point Lagrange scheme which takes into account the fact that the r_i are not equally spaced, and a 5-point Lagrange scheme which is similar but is of higher order.

First, we have considered a typical DA model which has been processed by the interface code in the manner discussed in this subsection; the model has 617 shells. For the 2-point numerical scheme we get $\sigma(P) = 0.36\%$ and $\sigma(M) = 0.28\%$; for the 3-point scheme we get $\sigma(P) = 0.24\%$ and $\sigma(M) = 0.24\%$; and for the 5-point scheme we get $\sigma(P) = 0.23\%$ and $\sigma(M) = 0.19\%$. It is seen that the average errors depend on the interpolation scheme, and decrease with increasing sophistication of the scheme. Presumably, the errors would have been somewhat smaller had we used a spline interpolation technique. Thus, a typical global accuracy of some 0.2% in the mechanical structure equations is easily achieved. It should be pointed out that the deviations are roughly uniform as functions of depth except for one specific region which we have left out in the averaging process. Indeed, in the innermost 7 or 8 shells, $dP/dr \to 0$, and it becomes intrinsically difficult to properly evaluate the numerical derivative $(dP/dr)_{\rm num}$ at the same relative accuracy as for the other shells. Errors contributing to $\sigma(P)$ can be as large as 20% in the central regions, but they reflect a numerical problem and not a consistency problem. We have excluded these regions in the evaluation of $\sigma(P)$. Also, to prevent the evaluation of $(dM/dr)_{\rm num}$ from becoming totally dominated by truncation

errors in the outermost layers where the inner mass practically does not change, we have instead calculated the equivalent derivative $dM/dr = -M dq/dr$. With that procedure, the error in the mass derivative is essentially uniform as a function of depth.

It is interesting to investigate the influence of the number of shells on the quantities $\sigma(P)$ and $\sigma(M)$. To this end, we have reprocessed the same evolutionary model with the interface code, but this time generating 1233 and 1849 shells, respectively. For the 5-point numerical differentiation scheme, our model with 617 shells has $\sigma(P) = 0.23\%$ and $\sigma(M) = 0.19\%$ as quoted above; a similar model with 1233 shells has $\sigma(P) = 0.22\%$ and $\sigma(M) = 0.20\%$; and yet another similar model with 1849 shells has $\sigma(P) = 0.22\%$ and $\sigma(M) = 0.19\%$. The average errors are essentially the same, and the regions where the deviations are the largest are also the same. This suggests that our interpolation technique *does* conserve the integrity of the mechanical structure equations. Adding shells improves the spatial resolution but does not degrade the basic structural consistency of a model. In fact, the errors are dominated by the differentiation schemes used to evaluate $(dP/dr)_{\rm num}$ and $(dM/dr)_{\rm num}$.

It is also quite interesting to go back to the original model without increasing the number of shells by interpolation. This model has 186 shells, and for every one of these shells the structure equations are strictly verified by definition of an evolutionary model (to the accuracy of the calculations, of course). If we apply the 5-point differentiation scheme, then $\sigma(P)$ and $\sigma(M)$ will measure *uniquely* the precision with which $(dP/dr)_{\rm num}$ and $(dM/dr)_{\rm num}$ can be evaluated with that scheme. Interestingly, the errors that we find are significantly larger than the one we quoted before; $\sigma(P)$ now equals 0.66% and $\sigma(M) \simeq 0.30\%$. These errors reflect the intrinsic accuracy with which one can verify the validity of the mechanical structure equations in this model and for this particular differentiation scheme. The fact that the errors are less for a similar model with a larger number of shells (obtained via interpolation) and for the same differentiation technique demonstrates without a doubt that our interpolation scheme is quite reliable. The added fact that the errors are *significantly* less in such a model is a bonus: it appears that the number of shells must be increased substantially beyond 186 to achieve the optimum distribution for sampling the numerical derivatives $(dP/dr)_{\rm num}$ and $(dM/dr)_{\rm num}$. Finally, it should be pointed out that we have evaluated $\sigma(P)$ and $\sigma(M)$ for a very large number of models, from very hot to very cold, including complete sequences. For all these models with, typically, 630–650 shells, $\sigma(P)$ and $\sigma(M)$ are both always very close to 0.2% (5-point Lagrange scheme).

e) The Grid of Models

Evolutionary models appropriate for pulsation investigations of DAV stars were first obtained with the primary aim of covering a large volume of parameter space. To this end, models with masses $M/M_\odot = 0.4$, 0.6, and 0.8 were computed. This mass range covers the observed narrow mass range for isolated white dwarfs as indicated previously. The mass of the outer hydrogen layer was varied from $\log q(\mathrm{H}) = -4.0$ (as imposed by standard evolution theory arguments) to $\log q(\mathrm{H}) = -14.0$. This latter value comes from an argument by Arcoragi and Fontaine (1980) which suggests that real DA white dwarfs cannot generally have an outer hydrogen layer much less massive than this value because it would not be stable against convective mixing with the underlying, active helium convection zone in such a case. The mass of the outer helium layer was varied from $\log q(\mathrm{He}) = -2.0$ (again imposed by standard pre–white dwarf evolution theory) to $\log q(\mathrm{He}) = -10.0$, always making sure that q(He) was larger than q(H) by at least 2 orders of magnitude in order to avoid overlapping H/He and He/C transition zones. The bulk of the evolutionary sequences were computed using the newer set of radiative opacities provided by Huebner (1980). However, a significant subset of sequences were computed using the older radiative opacity data of Cox and Stewart (1970). The effects of varying the assumed convective efficiency were explored by computing models with the ML1, ML2, and ML3 versions of the mixing-length theory. Because our approach is based on full evolutionary calculations, the range of effective temperatures of interest for DAV stars was systematically covered. Finally, we have computed a special sequence in which the scale heights of the transition zones have been reduced by a factor of 10 (i.e., α_1 and α_2 have been multiplied by 10 in eqs. [30] and [31]). This provides models with relatively narrow transition zones. This is of interest because the inclusion of thermal diffusion (which we have neglected) would somewhat decrease the scale height of a transition zone in diffusive equilibrium.

Table 2 summarizes the main characteristics of the DA evolutionary sequences. For simplicity in referring to a specific sequence, we have developed a short-hand notation which is given in column (1). In this notation, the first digit gives the mass of the model in tenths of solar mass units. The next two digits refer to the mass of the outer helium layer; the digits correspond to $-\log q$(He). Similarly, the fourth and fifth digits correspond to $-\log q$(H). A letter then follows, either C or L, depending on the actual set of radiative opacity data used in the calculations; C stands for the older Cox and Stewart (1970) tables and L for the newer Los Alamos data. Finally, the last digit refers to the version of the mixing-length theory used; 1 for ML1, 2 for ML2, and 3 for ML3. Thus, the symbol 60204C1 means a sequence of models with $M/M_\odot = 0.6$, $\log q(\mathrm{He}) = -2.0$, $\log q(\mathrm{H}) = -4.0$, and computed with the older opacity data and ML1 version of the mixing-length theory.

Column (2) of Table 2 gives the actual number of models calculated in a sequence. This entry shows that more than 11,300 models distributed among some 48 different evolutionary sequences were computed. Of course, these models are not all of direct interest for investigating DAV stars, and only a subset of them have been retained on disk files as eventual input data for the interpolation code. Column (3) of Table 2 gives the number of such models which have been kept for subsequent pulsation analysis. The numbers in parentheses give the initial and final epoch numbers for these models; generally, one model out of four would be retained in a given range of effective temperature. The effective temperatures of the hottest and coolest models of the subset are indicated under the symbols T_e(i) and T_e(f), respectively. Typically, we have retained models in the wide range 21,000 K $\gtrsim T_e \gtrsim$ 6000

TABLE 2

CHARACTERISTICS OF THE DA EVOLUTIONARY SEQUENCES

Sequence (1)	Number of Models (2)	Number of Stored Models (3)	T_e(i) (4)	T_e(f) (5)	T_e(m) (6)
60204C1.....	232	27(140–232)	18493	7328	...
60206C1*	300	31(156–259)	17021	6295	...
60206L3.....	245	26(156–245)	17021	6295	...
60207L1.....	252	63(16–252)	82985	6237	...
60207L3.....	249	31(140–249)	20653	6295	...
60208L1.....	249	30(152–248)	16595	6295	6457
60208L3.....	238	59(16–238)	71614	6237	6486
60209L1.....	251	63(16–251)	83752	6266	7762
60209L3.....	250	32(140–250)	20749	6251	8570
60210L1.....	227	23(144–227)	18197	7889	9016
60210L2.....	210	19(144–210)	18071	9494	9594
60210L3.....	220	21(144–220)	18071	8222	9750
60212L1.....	212	19(144–212)	18071	9247	9333
60213L1.....	199	16(144–199)	16595	9506	9571
60214L1.....	206	16(152–206)	16595	9594	10690
60406L1.....	248	29(148–248)	16481	6382	...
60408L1.....	242	32(136–242)	19231	6295	6411
60410L1.....	215	23(132–215)	19454	8337	8995
60412L1.....	196	16(140–196)	17538	9354	9354
60510C1*	301	28(176–268)	16595	6223	8933
60510L1.....	275	59(56–275)	54200	8630	9015
60510L3.....	212	52(16–212)	82604	9705	9750
T60510C1	249	21(176–249)	16788	8110	8690
60608L1.....	242	30(132–242)	21232	6237	6383
60610L1.....	229	24(144–229)	18113	7762	9057
60612L1.....	202	19(136–202)	19860	9332	9332
60810L1.....	239	24(152–239)	16904	6592	9036
60812L1.....	230	18(170–230)	17022	9290	9333
61012L1.....	212	20(136–212)	20701	9311	9333
40204C1.....	216	36(100–216)	16943	6237	...
40204L1.....	218	55(16–218)	41686	6295	...
40208L1.....	227	58(16–227)	44360	6237	7194
40210L1.....	193	39(52–193)	33573	8356	8610
40210L3.....	177	32(56–177)	32062	9141	9419
40212L1.....	207	54(16–207)	44668	8730	8954
40608L1.....	220	54(16–220)	44978	6223	7178
40612L1.....	185	47(16–185)	45186	8750	8995
41012L1.....	182	42(16–182)	45186	8690	8933
80204C1.....	285	52(194–285)	19099	7469	...
80204L1.....	300	44(136–300)	33266	6310	...
80206C1.....	309	28(220–309)	16860	6306	...
80208L1.....	281	45(116–281)	42560	6266	...
80210L1.....	262	29(164–262)	19498	6324	8550
80210L3.....	272	29(164–272)	19633	6310	9885
80212L1.....	242	37(79–242)	64416	9750	9840
80608L1.....	294	56(72–294)	72444	6281	...
80612L1.....	259	45(70–259)	98855	9572	9840
81012L1.....	257	44(71–257)	64863	9462	9750

NOTE.—See text for explanation of table.

TABLE 3

CHARACTERISTICS OF THE DB EVOLUTIONARY SEQUENCES

Sequence	Number of Models	Number of Stored Models	T_e(i)	T_e(f)	T_e(m)
60200L1	225	57(20–225)	101625	12106	...
60400L1	305	78(20–305)	103039	6266	...
60600L1	256	67(20–256)	103039	14289	14621
60600L3	245	59(32–245)	95060	10399	17989
60800L1	233	61(20–233)	110408	13614	16788
61000L1	274	75(20–274)	102801	13002	17458
61200L1	202	53(20–202)	103040	17413	17701
40800L1	190	53(20–190)	50700	16180	16180

NOTE.—See text for explanation of table.

K, but the coverage has been even much broader for a substantial number of sequences. Although the hot models are not relevant to the DAV phenomenon, they remain quite useful for studies of trace-element diffusion used in investigations of the spectral evolution of white dwarfs. On the average, the spacing in effective temperature between two consecutive models in the subset is ~ 560 K. However, we have purposely computed a larger number of models in the range of effective temperature of immediate interest for DAV stars (14,000 K $\gtrsim T_e \gtrsim$ 9000 K), and the average spacing in this range is ~ 280 K. This provides excellent temperature coverage of the DAV instability strip. Finally, column (6) of Table 2 lists the effective temperature T_e(m) of the first model of a sequence (if any) in which the superficial H convection zone has merged with a subphotospheric He convection zone. The subsequent mixing episode would completely dilute the outer H layer, so that models cooler than T_e(m) in a given sequence are no longer representative of DA stars (their atmospheres would now be dominated by helium). They cannot be used in pulsation studies of DAV stars.

Three special sequences in Table 2 are worthy of mention. First, the one sequence with thin composition transition zones is labeled T60510C1. Also, two sequences (noted by an asterisk in Table 2) have been pursued to lower temperatures than indicated in the table. Indeed, for comparison purposes (see § III*a*) as well as spectral evolution needs, we have followed the evolution of 60206C1 models down to $T_e = 3828$ K and that of 60510C1 models down to $T_e = 4140$ K.

Table 3 gives the main characteristics of the evolutionary sequences relevant to the DBV instability strip. The format is identical to that of Table 2. The absence of an outer hydrogen layer is symbolized by the fourth and fifth digits assuming values of zero. Note that, for reasons of spectral evolution, the temperature coverage is quite wide. With only eight evolutionary sequences (as compared with 48), our coverage of parameter space for the DBV phenomenon is less extensive than our effort for DAV objects, allowing that we do not have to explore the effects of varying q(H). Nevertheless, this more limited exploration of parameter space for DBV stars remains by far the most extensive effort that has been made up to now. In fact, the DB models, together with those of the DA evolutionary sequences, form a data bank of more than 2200 models of potential interest in pulsation studies of white dwarfs. This large number of models exceeds by *more than 2 orders of magnitude* the number of models used in *all* the comparatively limited explorations of DAV and DBV parameter space carried out by other groups. The size of the data bank also explains, in part, why the models described in the present paper have still not been fully exploited and are the subjects of ongoing pulsation investigations.

III. PROPERTIES OF THE EVOLUTIONARY MODELS

a) *Basic Cooling and Structural Characteristics*

i) *Comparison with Other Evolutionary Calculations*

As indicated in § II*a*, we have concentrated most of our efforts on the evolutionary phases near the DAV instability strip. In the process, we have made a number of simplifying assumptions which are reasonable for white dwarfs of intermediate luminosities (such as DAV stars), but which are generally not justified in the very hot or in the very cool phases of white dwarf evolution. Hence, our calculations are not of immediate relevance to the general problem of establishing a theoretical luminosity function over the full range of white dwarf luminosities. However, it is important to demonstrate that our cooling time scales and structural properties are reliable in the phases near the DAV instability strip. For example, the predicted rates of change in the periods of pulsation modes across the instability strip are directly related to our cooling time scales.

In this context, we first compare the cooling curve (i.e., luminosity versus time) of a typical sequence with those obtained in several recent investigations of the white dwarf cooling problem. We have chosen the 60204C1 sequence, since q(H) and q(He) are the closest to the values used in these other investigations. The small filled circles in Figure 1 give the cooling curve for our 60204C1 sequence. As a comparison, the larger open circles give the cooling curve for an evolutionary sequence by Iben and Tutukov (1984) which is characterized by $M/M_\odot = 0.6$, $\log q(\mathrm{He}) = -1.36$, and $\log q(\mathrm{H}) = -3.60$. These models have a mixed C/O interior, and residual hydrogen burning goes on down into the DAV range. Another independent result is the continuous line which represents the cooling curve of a DA evolutionary

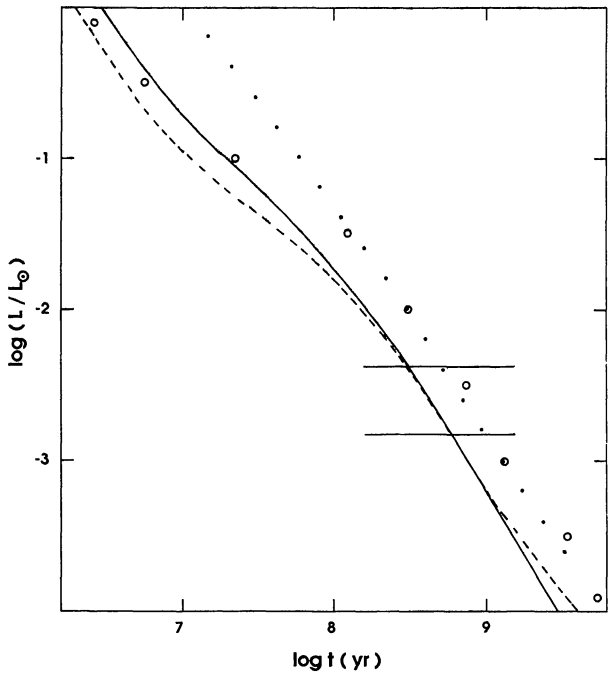

FIG. 1.—Cooling curves (luminosity vs. time) for four different evolutionary sequences of DA white dwarfs. The small filled circles give the results of the present investigation for the 60204C1 sequence. The large open circles refer to the calculations of Iben and Tutukov [1984; 0.6 $M_\odot$, log q(H) = −3.60, log q(He) = −1.36], the continuous curve to those of Koester and Schönberner [1986; 0.6 $M_\odot$, log q(H) = −3.81, log q(He) = −1.63], and the dashed curve to those of Mazzitelli and D'Antona [1986; 0.7 $M_\odot$, log q(H) = −6.78, log q(He) = −1.60]. The two horizontal lines define the width of the observed DAV instability strip in terms of the luminosity.

sequence computed by Koester and Schönberner (1986). That particular sequence is characterized by $M/M_\odot = 0.598$, log q(He) = −1.63, and log q(H) = −3.81. The models also have a C/O interior, but residual hydrogen burning is found to be totally negligible. Finally, a result by Mazzitelli and D'Antona (1986) is shown by the dashed line. It gives the cooling curve for another DA evolutionary sequence characterized by models with C/O interiors, $M/M_\odot = 0.7$, log q(He) = −1.60, and log q(H) = −6.78. Nuclear burning is negligible.

The first observation that we can make from Figure 1 is that our results deviate substantially from the results of the other investigations in the high-luminosity phases of the evolution. This is due, of course, to our neglect of neutrino cooling processes, which leads to a larger age for a given luminosity in these phases. However, in the DAV instability strip (identified by the two horizontal lines in the figure) our results are sandwiched between those of the other investigators. The dispersion shown in the DAV strip is representative of modern calculations of the evolution of cooling white dwarfs. Actually, this dispersion can be reduced if adjustments are made to account for the different choices of parameters (cf. Winget and Van Horn 1987). For example, the 60204C1 curve should be shifted slightly to the left to take into account the fact that C/O white dwarfs have a lower heat capacity than pure C white dwarfs and, consequently, cool faster. Likewise, the three other curves should be shifted slightly to the right in the DAV range when their larger values of log q(He) are adjusted to a value of −2.0. This is because the conductive opacity of carbon is larger than that of helium and the adjustment would render the matter more opaque, hence slowing the cooling process in the low-luminosity phases. From these arguments, we conclude that there is good consistency between cooling curves of independent investigations in the DAV range and, in particular, that our results are in good agreement with those of contemporary investigations in this range.

A much more rigorous comparison can be made with an unpublished evolutionary sequence computed by Winget, Lamb, and Van Horn a few years ago at the University of Rochester and using the same techniques as those used by Wood, Winget, and Van Horn (1987). We refer to this sequence as R60510C1 in the notation introduced above. It has been used, for example, in the investigation of Winget *et al.* (1987), which presents a new method for estimating the age of the universe based on white dwarf physics. A more rigorous comparison than that shown in Figure 1 can be made, for two reasons. First, an evolutionary sequence with parameters [total mass, pure carbon interior, q(He), q(H), radiative opacity, conductive opacity, envelope equation of state, and convective efficiency] identical to those of the R60510C1 sequence can be computed. We have explicitly calculated our 60510C1 sequence with this comparison in mind; it was extended to effective temperatures lower than our normal limit of log T_e = 3.8 for that specific purpose. Convective mixing has been ignored in the two sequences. Second, we know *exactly* what the differences are between the two sets of calculations, which implies that, in principle, we should be able to identify the cause of possible differences in the cooling and structural properties of the models.

A first difference between the two sets of calculations is that they are based on two independent, completely different evolution codes. We have described the code used in the present paper in § II. The code used by Winget, Lamb, and Van Horn is based on that developed by Lamb (1974). The "atmosphere" in that code is, in fact, an envelope structure computed by the envelope code written by Fontaine (1973). Thus, the Henyey "interior" does not extend to the photosphere in the Winget, Lamb, and Van Horn code. There are also differences in the gray atmosphere strategy, the shell distribution in the envelope, and the technique for solving by iteration the equations involving convection. Further differences in the two sets of calculations are that the R60510C1 calculations assume discontinuous transition zones and the so-called Böhm-Stuckl prescription for the mixing length is used in conjunction with the ML1 version of the mixing-length theory (Böhm and Stuckl 1967; see below). Moreover, the full equation-of-state tables of Fontaine, Graboske, and Van Horn (1977) (54 isotherms instead of 27) have been used in the R60510C1 calculations. We note that none of these differences are expected to influence significantly the cooling properties of the models.

More important from that point of view is the inclusion of neutrino processes in the R60510C1 calculations. Likewise, an

important difference is the sophisticated treatment of the ionic system for the interior equation of state which was included in the R60510C1 computations. This treatment is based on the dense, totally ionized, pure carbon equation of state of Lamb (1974). Significant differences in the heat capacity of the internal thermal reservoir are expected here. At low enough luminosities, the R60510C1 calculations also include the effects of the ionic system in the core undergoing a first-order phase transition from the liquid to the solid phase with the associated release of latent heat. Further effects, such as the decrease of the specific heat of the ions in the quantum regime, lead to an accelerated phase of cooling referred to as Debye cooling, and this is included in the R60510C1 calculations.

In order to understand the following figures, it is best first to recall some basic features of white dwarf cooling theory. In its simplest version (Mestel 1952; Van Horn 1971; Winget and Van Horn 1987), the theory shows that the cooling problem can be understood in terms of two fundamental problems. The first is that of determining the amount of thermal energy available in the reservoir constituted by the core, since thermal motions are believed to be the essential source of the luminosity of a white dwarf. This requires a detailed knowledge of the thermodynamics of the stellar interior. In particular, the specific heat of the core material must be derived; the main contribution coming from the specific heat of the ionic system because degenerate electrons cannot contribute much to the overall heat capacity of the interior of a white dwarf. The second problem is to determine the rate at which this thermal energy is transferred from the hot, almost isothermal interior to the cold interstellar medium. This involves the solution of the energy transfer problem across the thin, outer nondegenerate layers. The opacity of these layers thus plays an essential role by regulating the heat flow. It has been shown explicitly by Fontaine and Van Horn (1976) that the envelope structures converge to the well-known "radiative zero solution" as long as convection does not reach the boundary of the degenerate core, i.e., at high enough luminosities. In such a case, the heat flow is regulated by the radiative opacity of the material at the core boundary. Note that the conductive opacity of the core material also plays an important role in the energy transfer problem, since there exists a nonnegligible temperature gradient between the core boundary and the center of the star (Fontaine and Van Horn 1976). Because of the convergence properties of the "radiative zero solution," cooling is not affected by possible differences that may characterize the upper part of the envelope (e.g., different composition stratifications) and therefore does not depend on the detailed opacity profile in these regions. In the case where superficial convection does reach into the degenerate core (i.e., in the cooler phases of evolution), the above insensitivity of the temperature stratification to the details of the heat transfer problem in the nondegenerate layers is lost. Instead, the temperature stratification depends on a specific convective solution which ties the surface to the base of the convection zone. The heat flow is then regulated by the overall opacity distribution in these outer layers, from the conductive opacity of the material below and at the base of the convection zone to the radiative opacity of the atmospheric material.

A priori, we can expect the temperature structures of similar models (same luminosity) belonging to the R60510C1 and 60510C1 sequences to be quite similar. This is because the solution of the heat transfer problem depends primarily on the opacity profile (in principle, both sets of calculations use the same opacities) and very much less on the equation of state (which is somewhat different in the interior). This expectation is borne out by Figure 2, which shows the luminosity–central temperature relationship for both the R60510C1 sequence (*continuous curve*) and the 60510C1 sequence (*dashed curve*). From the point of view of cooling, the essential result of the heat transfer problem across the nondegenerate layer is contained in this relationship between the luminosity and the temperature of the degenerate, nearly isothermal core. We first remark that our central temperatures are larger than those of the R60510C1 sequence at high luminosities because of our neglect of neutrino emission processes. These processes are the dominant cooling mechanisms in the hot phases of white dwarf evolution and can reduce the core temperature considerably in such phases. Figure 2 shows, however, that neutrino cooling becomes negligible below a luminosity $\log (L/L_{\odot}) \simeq -1.2$; at this point in the evolution, the temperature structures of the R60510C1 and 60510C1 sequences become nearly identical. We note that in the range $-1.2 \gtrsim \log (L/L_{\odot}) \gtrsim -3.7$ (which includes the DAV range), the L-T_c relationships are remarkably similar. This is particularly true in view of the numerous residual differences between the two evolution codes as explained above. This gives us added confidence in the internal consistency and reliability of our code.

Below a luminosity of $\log (L/L_{\odot}) \simeq -3.7$, Figure 2 reveals a structure in the L-T_c relationship associated with the influence of convection. Indeed, for the first time in the evolution, convection has broken into the degenerate core and, from that point on, influences the cooling process directly by flattening the temperature gradient between the core and the surface. In essence, convective transport across the whole nondegenerate layer renders the layer more transparent. The change of slope in the L-T_c relationship shown in Figure 2 is thus associated with this lowering of the core temperature caused by convection. An unexpected result of this feature, however, is that we observe small but significant differences between the L-T_c relationships of the two sets of calculations; our central temperatures are systematically lower than those predicted by the R60510C1 calculations for $\log (L/L_{\odot}) \lesssim -3.7$. Considering our discussion above, this result is quite puzzling because practically *no* differences are expected in this luminosity range. We have consequently spent some time trying to solve this puzzle. First, although the avenue did not seem very promising, we have thoroughly investigated the effects of differences in the treatment of convection between the two sets of calculations. To complement the evolutionary calculations, we have used an envelope code based on the same constitutive physics as in the evolution code. Thus, we have explicitly verified with this envelope code the expectation that the different assumed convective efficiencies (ML1, ML2, or ML3 with or without the Böhm-Stuckl prescription) do *not* affect at all the cooling time scale or the L-T_c relationship of an evolving white dwarf. This is because convection can affect the cooling process only at relatively low luminosities. At such

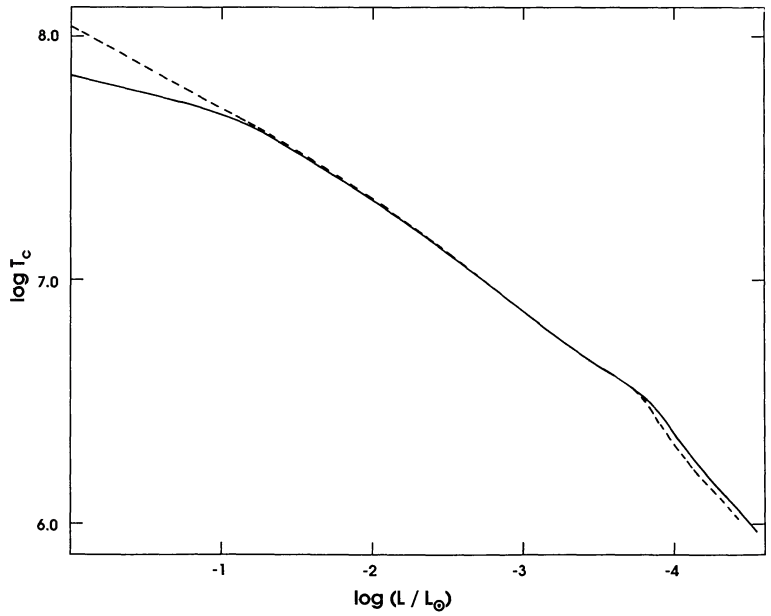

FIG. 2.—Central temperature vs. luminosity for evolving DA white dwarfs. The dashed curve corresponds to the results of the 60510C1 sequence, and the continuous curve to those of the R60510C1 sequence.

low luminosities the convective stratification has become essentially adiabatic (cf. Fontaine and Van Horn 1976). Hence, the efficiency of convective transport and the extent of the superficial convection zone do not depend on the usual free parameters of the mixing-length theory as they do at high luminosities. We have also verified explicitly that the different treatments of the composition transition zones in the two sets of calculations lead to insignificant differences in the L-T_c relationship. Likewise, we find that the onset of crystallization at $\log (L/L_\odot) = -3.75$ and the associated release of latent heat in the R60510C1 sequence cannot affect the L-T_c relationship as illustrated in Figure 2.

We have traced the problem back to a small inconsistency in the R60510C1 calculations. In these models, the conductive opacity of *carbon* was used throughout, even in the He-rich layers above $\log q \simeq -5$ and in the H-rich layers above $\log q \simeq -10$. Because the conductive opacity of carbon is larger than that of helium or hydrogen, this leads to a higher overall opacity in these layers. That this inconsistency does not affect the cooling process in the range $-1.2 \gtrsim \log (L/L_\odot) \gtrsim -3.7$ (as evidenced by the excellent agreement between the two L-T_c relationships in Fig. 2) is simply a result of the fact that the boundary of the degenerate core is located in the C-rich layers in that range, i.e., below the level $\log q \simeq -5$. From the arguments presented above, the heat flow is then basically governed by the opacity profile from the center to the core boundary, and the upper envelope has a "radiative zero solution" character which implies that the presence of helium and hydrogen regions (with their overestimated opacity) for $\log q \lesssim -5$ is not relevant. It is only at low luminosities that the opacity problem leads to some small effects. In practice, we can define the "core boundary" as that layer where the radiative and conductive opacities are equal. This very nearly corresponds to a value of the usual electron degeneracy parameter $\eta \simeq 5$. Our detailed results show that the level $\eta = 5$ migrates upward with cooling and, in the 60510C1 models, crosses the level $\log q \simeq -5$ at almost exactly a value of $\log (L/L_\odot) \simeq -3.7$. (At slightly lower luminosities, convective transport ties the surface to the core.) Thus, the inconsistency characterizing the R60510C1 calculations starts manifesting itself only at these low luminosities, when the core boundary has moved into the He-rich layers above $\log q \simeq -5$. Because the overall opacity is now slightly larger in the R60510C1 models (because of the uniform use of the conductive opacity of carbon), the derived central temperature is slightly larger, as shown in Figure 2 for $\log (L/L_\odot) \lesssim -3.7$. Recent results obtained by M. A. Wood show that new R60510C1 models (corrected for the small opacity inconsistency) give, as expected, the same L-T_c relationship as that shown by the dashed curve at low luminosities in Figure 2.

Figure 3 shows the cooling curves for both the R60510C1 sequence (*continuous curve*) and the 60510C1 sequence (*dashed curve*). At high luminosities, the main differences in the cooling curves are caused by our neglect of neutrino processes; the 60510C1 models evolve more slowly as expected. As indicated above, the effects of neutrino cooling on the temperature structure have essentially vanished by the time the model has cooled to a luminosity $\log (L/L_\odot) \simeq -1.2$. We have just shown that below this luminosity, the solution of the heat transfer problem gives the same L-T_c relationship for the two sets of calculations. The difference in the cooling curves observed in Figure 3 must then be attributed to the other aspect of cooling theory, namely, the question of the energy content in the thermal reservoir. Our rough treatment of the ionic system in the deep stellar interior overestimates the effects of Coulomb interactions as compared with the sophisticated treatment of Lamb (1974). Thus, our models have more energy to get rid of because the specific heat of the core material is larger. Our cooling time to a given luminosity is consequently larger than that of the R60510C1 sequence. The

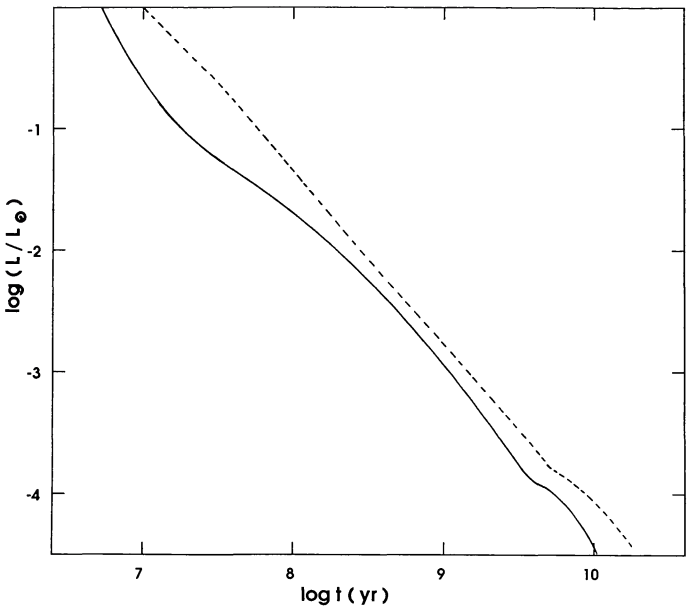

FIG. 3.—Cooling curves (luminosity vs. time) for two sequences of evolving DA white dwarfs. The dashed curve corresponds to the results of the 60510C1 sequence, and the continuous curve to those of the R60510C1 sequence.

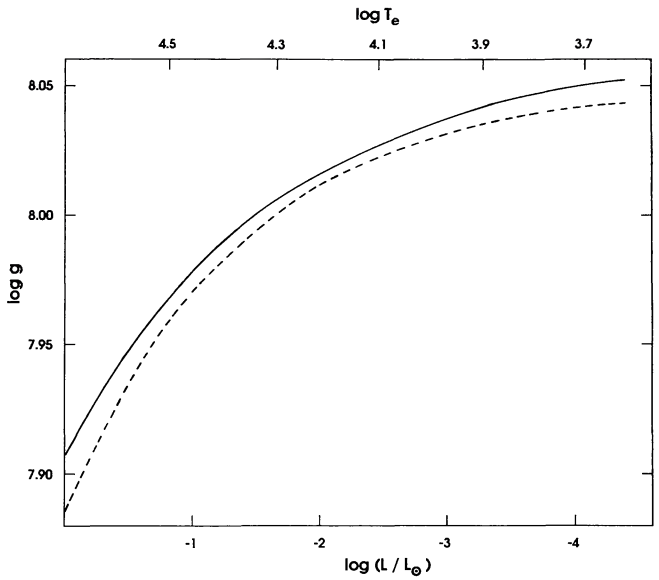

FIG. 4.—Gravity vs. luminosity for two sequences of evolving DA white dwarfs. The dashed curve corresponds to the results of the 60510C1 sequence, and the continuous curve to those of the R60510C1 sequence. The upper scale gives the effective temperature as obtained from R60510C1 models.

effect is visible throughout the luminosity range shown in Figure 3. In the DAV instability strip itself, our cooling time scales are typically 25% larger than those of the R60510C1 calculations.

The bump observed in the 60510C1 curve of Figure 3 at $\log (L/L_{\odot}) \lesssim -3.7$ is associated with the drop of the central temperature in Figure 2 and corresponds to convection (the base of the helium convection zone) breaking into the degenerate core and tying the latter directly to the surface. Because convection is more efficient than radiation at transporting energy (it flattens the temperature gradient more), there is, initially, an excess of energy to get rid of and the cooling process is slowed down somewhat, thus producing the bump. With time, the effects of convection would be to *speed up* the cooling process as compared with purely radiative models, but this is not shown in the figure because the computations were terminated at too large a luminosity.

The R60510C1 curve shows a similar feature due to the same phenomenon. However, in that case there is an additional contribution to the slowing down of the cooling process which is caused by the gradual release of latent heat from the crystallizing core. By accident, in this particular sequence, crystallization sets in at the center of the star around $\log (L/L_{\odot}) \simeq -3.75$, which causes a superposition of the phenomena. The final turnover in the continuous curve is related to the onset of Debye cooling.

Further comparisons can be made between the R60510C1 and 60510C1 sequences. For example, Figure 4 shows a plot of the surface gravity as a function of luminosity (*lower scale*) or effective temperature (*upper scale*) for the R60510C1 sequence (*continuous curve*) and the 60510C1 sequence (*dashed curve*). Note that the effective temperature scale in relation to the luminosity scale is derived from the R60510C1 results. We again observe an excellent agreement over the full luminosity range, typical differences in surface gravity being of the order of 1% in the DAV range. Interestingly, our values of the surface gravity are systematically lower than those of the R60510C1 calculations. We attribute this to the different treatment of the envelope: ours is allowed to "evolve" within the Henyey algorithm, whereas the envelope is static in the Winget, Lamb, and Van Horn code. Because our models are very slightly more extended, we can expect that the central pressure (and consequently the central density) is somewhat lower in the 60510C1 models. This should be true at very low luminosities where the mechanical structure is completely dominated by the pressure of degenerate electrons and where ions contribute negligibly to the support against gravity. Figure 5 indicates that this is indeed the case for luminosities lower than $\log (L/L_{\odot}) \simeq -2.0$, which includes the DAV strip. It shows the relationship between the central density and the central temperature for the R60510C1 sequence (*continuous curve*) and the 60510C1 sequence (*dashed curve*). The dotted lines join the points of equal luminosities; they are labeled by the values of $\log (L/L_{\odot})$. Thus, for the lower luminosities, a somewhat reduced central density (hence pressure) is sufficient to support a somewhat more extended model. The situation gets more complicated with increasing luminosity because the contribution of the ions to the total pressure can no longer be totally ignored. In particular, it has already been pointed out that our treatment of the equation of state of the deep interior overestimates the Coulomb corrections due to interactions among ions. This means that, in comparison with the equation of state of Lamb (1974), our total pressure is less for a given pair (ρ, T) in the regime where the Coulomb corrections to the pressure are not totally negligible. Thus, to compensate for this softening of the equation of state, higher

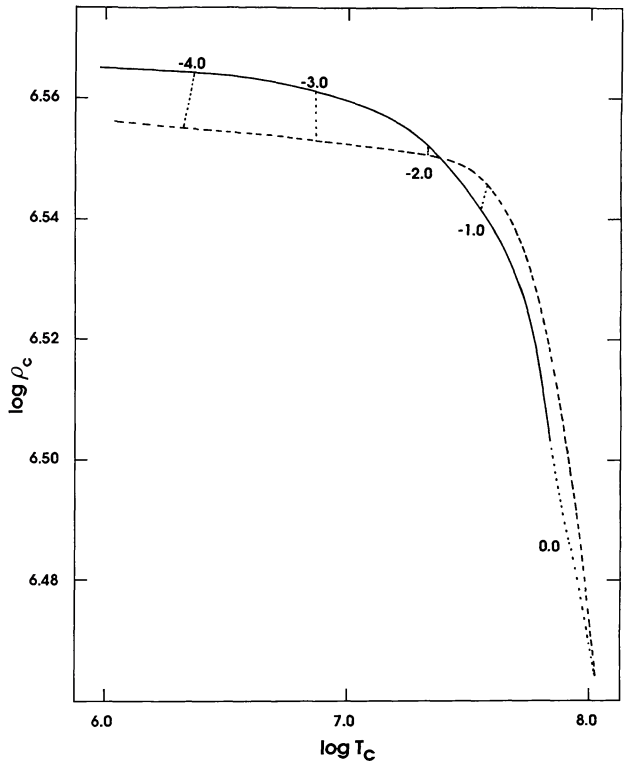

FIG. 5.—Central density vs. central temperature for two sequences of evolving DA white dwarfs. The dashed curve corresponds to the results of the 60510C1 sequence, and the continuous curve to those of the R60510C1 sequence. The dotted curves are lines of constant luminosity labeled by the value of log ($L/L_\odot$).

values of the core density are required to provide the same mechanical support. This explains why ρ_c is larger in the 60510C1 sequence than in the R60510C1 sequence at high luminosities. Figure 5 shows a final reversal in the extreme limit of high luminosities: the central density of the R60510C1 sequence is again larger than in the 60510C1 sequence. This reversal is easily explained here because the central temperature is substantially larger in the 60510C1 sequence because of our neglect of neutrino cooling. The difference of temperature is sufficiently large that thermal pressure in the very luminous 60510C1 models now contributes significantly to the mechanical support, thereby reducing the requirement on the central density.

The comparisons that we have carried out in this subsection show that our evolutionary models are consistent with the models obtained in other, independent studies of evolving white dwarfs. In particular, our results for the phases near the DAV instability strip are comparable to those of other modern calculations. Thus, our models can be used with confidence for pulsation studies of white dwarfs.

ii) *Differential Effects on the Luminosity-Core Temperature Relationship and on the Cooling Curve*

An interesting benefit of our exploration of a large volume of parameter space is the possibility of learning about the effects of various parameters on the cooling and structural properties of evolving white dwarfs to an extent not achieved before. In this subsection, we first focus on the effects of varying the total mass, the mass of the outer helium layer [q(He)], and the mass of the outer hydrogen layer [q(H)] on the luminosity-core temperature relationship of stratified white dwarfs. In the context of cooling white dwarfs, this relationship is the essential result of the solution of the heat transfer problem as explained above. Several investigations have discussed the L-T_c relationship in their studies of evolving degenerate stars (e.g., Lamb and Van Horn 1975; Sweeney 1976; Shaviv and Kovetz 1976; Iben and Tutukov 1984; Mazzitelli and D'Antona 1986; Wood, Winget, and Van Horn 1987; D'Antona and Mazzitelli 1987), but not to the extent possible in the present study. The L-T_c relationship is also of particular interest for pulsating white dwarfs, as Osaki and Hansen (1973) have shown that the rates of period changes of the nonradial gravity-mode oscillations are sensitive to the core temperatures of the white dwarf models, implying that the period evolution is strongly coupled to the core temperature evolution.

At the outset, it is appropriate to recall that the L-T_c relationship is totally insensitive to the assumed convective efficiency. Moreover, our results show that the relationship is also insensitive to the choice of the radiative opacity set. Hence, from that point of view, the results of the 60206C1 sequence are identical to those of the 60206L3 sequence, for example.

The continuous lines in Figure 6 give the luminosity–central temperature relationships for sequences with $M/M_\odot = 0.4$, 0.6, and 0.8 from top to bottom, respectively; each sequence is parameterized by log q(He) $= -2.0$ and log q(H) $= -4.0$. (The data were taken from the 40204C1, 60204C1, and 80204L1 sequences). Note that the luminosity range shown in Figure 6 corresponds to the evolutionary phases in which our models should be most reliable; our neglect of neutrino cooling affects only the high-luminosity phases of the evolution. Our computations were also generally stopped before the onset of crystallization in the core, but this is not expected in any case to seriously affect the L-T_c relationship. The luminosity window of the figure is directly relevant to pulsating white dwarfs (because it encompasses both the DAV and the DBV instability strips), and to white dwarfs in general (since the bulk of the observed white dwarfs are found in the luminosity range $-1.5 \gtrsim \log (L/L_\odot) \gtrsim -3.3$).

Figure 6 shows that the less massive stars have larger central temperatures for a given luminosity in this range. This is because less massive stars have relatively lower densities in their interiors. This results in decreased degeneracy overall and associated increased conductive opacities. In addition, the less massive stars are cooler for a given luminosity (because their radii are larger), which implies that their envelopes are more opaque, the main atmospheric constituent being less ionized. This combination of increased opacities produces steeper temperature gradients and, consequently, larger core temperatures. The results of Figure 6 are qualitatively consistent with the predictions of simple cooling theory (cf. Mestel 1952), which suggests that $T_c \propto M^{-2/7}$ for a given luminosity, and $T_c \propto L^{2/7}$ for a given mass. Quantitatively, however, the actual results are substantially different from these simple

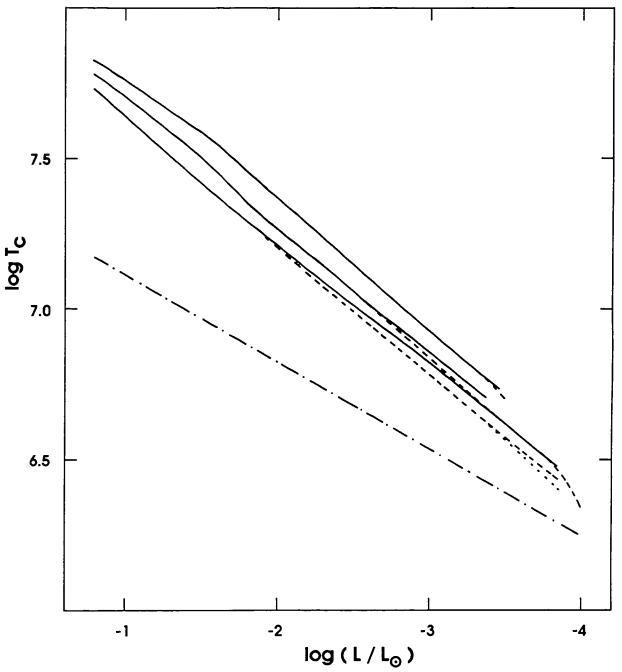

FIG. 6.—Central temperature vs. luminosity for several sequences of evolving DA white dwarfs. The three continuous curves show the L-T_c relationships for models with $\log q(\mathrm{He}) = -2$ and $\log q(\mathrm{H}) = -4$, and for $M/M_\odot = 0.4$, 0.6, and 0.8, from top to bottom, respectively. The dashed portions of the curves correspond to sequences with somewhat thinner hydrogen layer, i.e., with $\log q(\mathrm{H}) = -6$. The dotted extension of the curve for the 0.8 $M_\odot$ sequences corresponds to models with $\log q(\mathrm{H}) = -8$. These extensions illustrate the insulating effect of the hydrogen outer layer. The dash-dot line shows the slope (2/7) of the linear relationship between $\log T_c$ and $\log (L/L_\odot)$ predicted by simple cooling theory.

power laws. As a comparison, the dash-dot line gives the slope (2/7) of the linear relationship predicted by simple cooling theory between $\log T_c$ and $\log (L/L_\odot)$.

The effects of composition layering are also illustrated in Figure 6. We find, for example, that the L-T_c relationship is the same for *all* 0.6 $M_\odot$ sequences with $\log q(\mathrm{He}) = -2.0$ in the range $-0.8 \gtrsim \log (L/L_\odot) \gtrsim -2.6$, irrespective of the value of q(H). This includes the sequence 60200L1, which has *no* hydrogen. Thus, for $\log q(\mathrm{H}) \lesssim -4.0$, the hydrogen layer has no influence whatsoever on the L-T_c relationship in this luminosity range. The explanation for this phenomenon is relatively simple. Above a luminosity $\log (L/L_\odot) \simeq -2.6$, the boundary of the degenerate core is located deeper than $\log q \simeq -4.0$, i.e., deeper than the base of the largest possible hydrogen outer layer. As discussed previously, and for the luminosities of interest, convection does not reach into the degenerate core, which implies that the heat flow is simply governed by the opacity profile from the center of the star to the core boundary. Above the core, the convergence properties of the "radiative zero-like solution" make the details of the stratified envelope unimportant; what matters is the radiative opacity of the material in the vicinity of the core boundary, in our case the radiative opacity of helium. Thus, the energy transfer problem gives the *same* L-T_c solution for all the models, irrespective of the presence and thickness of a hydrogen outer layer.

With cooling, the degeneracy boundary moves up into the star and, in our 0.6 $M_\odot$ models with $\log q(\mathrm{He}) = -2.0$, reaches the level $\log q \simeq -4.0$ around $\log (L/L_\odot) \simeq -2.6$. At that luminosity, different L-T_c solutions become possible. The heat transfer problem starts to feel the effects of the radiative opacity of *hydrogen* in the vicinity of the core boundary for those models with thick hydrogen layers [$\log q(\mathrm{H}) = -4.0$], while it still remains decoupled from the presence of hydrogen for those models with thinner hydrogen layers [e.g., $\log q(\mathrm{H}) < -6.0$]. Under the conditions of interest (both H and He are ionized, and the radiative opacity is of the Kramers type), the radiative opacity of hydrogen is significantly larger than that of helium, and, consequently, the models with thick hydrogen layers first experience the insulating effects of hydrogen. Those models therefore keep higher central temperatures with further cooling. Progressively, further solutions become possible as the boundary of the degenerate core continues to rise, moving across other levels [$\log q(\mathrm{H}) = -6.0$, and so on]. Our computations do not extend to low enough luminosities for these effects to become visible in the figure, however. Figure 6 nevertheless does show the first divergence point around $\log (L/L_\odot) \simeq -2.6$. Below this luminosity, the continuous part of the curve refers to the 60204C1 sequence, and the dashed part to all other sequences with $\log q(\mathrm{H}) \lesssim -6.0$ and $\log q(\mathrm{He}) = -2.0$. No differences are found in the L-T_c relationships between these sequences in regions of overlapping luminosities; note that we have used the extended sequence 60206C1 to pursue the dashed part of the curve to very low luminosities. The final turnover of this curve for $\log (L/L_\odot) \lesssim -3.8$ is associated with superficial convection breaking into the degenerate core in a manner similar to the effects shown on Figure 2.

The cases of the other masses shown in Figure 6 can be interpreted in the same way. We note that the sequences with $M = 0.4$ $M_\odot$ retain an insensitivity to q(H) to much lower luminosities than the 0.6 $M_\odot$ models, the first divergence occurring around $\log (L/L_\odot) \simeq -3.3$. The dashed portion of the 0.4 $M_\odot$ curve comes from data taken from the 40208L1 sequence. This late divergence can be understood if we recall once again that less massive white dwarfs have characteristically lower densities. This implies that the boundary of the degenerate core is located deeper in such stars (cf. Fontaine and Van Horn 1976). Hence, this boundary crosses the level $\log q \simeq -4.0$ at smaller luminosities for the 0.4 $M_\odot$ models as compared with the 0.6 $M_\odot$ models, and the insulating effects of the hydrogen layer can only appear at these lower luminosities. By the same token, the effects become noticeable earlier (i.e., at higher luminosities) in the life of more massive stars. In particular, note how the 0.8 $M_\odot$ curve in Figure 6 shows *two* divergence points—the continuous part of the curve referring to the 80204L1 models, the dashed part to the 80206C1 models, and the dotted part to the 80208L1 models.

The effects of varying the mass of the helium layer, keeping the total mass constant, are illustrated in Figure 7. The lower curve gives the L-T_c relationship for the 60200L1 sequence. Because that particular sequence (appropriate for DBV studies) has been stopped relatively early, we have extended it by

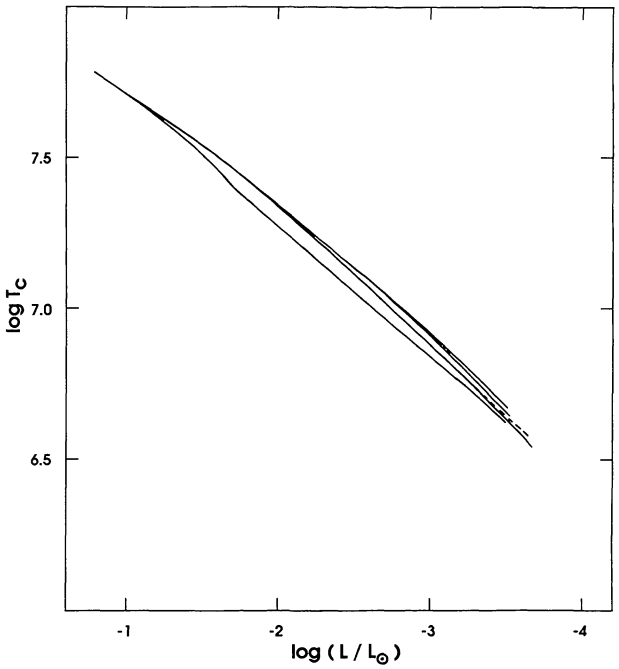

FIG. 7.—Central temperature vs. luminosity for 0.6 $M_\odot$ white dwarf sequences with different values of the mass of the helium layer and negligible values of the mass of the hydrogen layer. The lower curve gives the results for a white dwarf sequence with log q(He) = −2. The second curve from the bottom shows the L-T_c relationship for sequences with log$q$(He) = −4; the short dashed extension of the curve corresponds to the small insulating effects of adding a thin layer of hydrogen [log q(H) = −6]. The second curve from the top shows the L-T_c relationship for models with log q(He) = −6, and the upper curve shows the corresponding relationship for models with log q(He) = −8.

using data from the 60208L1 sequence below log $(L/L_\odot) \simeq -2.5$. This is quite consistent because the effects of adding a layer of hydrogen as small as log q(H) = −8.0 on the L-T_c relationship have just been shown to be negligible in the luminosity range of interest. The second curve from the bottom in Figure 7 shows the results for the 60400L1 sequence. Below log $(L/L_\odot) \simeq -3.3$, the presence of a hydrogen layer in the 60406L1 models (*dashed part of curve*) has a tiny insulating effect, as expected from the above discussion. The third curve from the bottom corresponds to models with log q(He) = −6.0; specifically, the data were taken from the 60600L1 sequence extended at lower luminosities by the 60608L1 sequence. Finally, the upper curve refers to the 60810L1 sequence and is representative of *all* models with log q(He) ≤ -8.0 (including pure carbon models) in the luminosity range illustrated. The lesson to be retained from Figure 7 is that the central temperatures are essentially the same at high luminosities for all models with log q(He) ≤ -2.0, but that they decrease faster with decreasing luminosities the thicker the helium layer. So, contrary to the case of hydrogen, increasing the mass of the helium outer layer actually decreases the overall temperature gradient between the surface and the core of a white dwarf.

We can understand the behavior shown in Figure 7 in a manner similar to our explanation of the main features of Figure 6. At the highest luminosities, the boundary of the degenerate core is below the level log $q \simeq -2.0$ and the heat transfer problem is purely specified by the opacity of carbon for all the models considered. As cooling proceeds, the core boundary moves above that level and the heat transfer problem now depends, in part, on the radiative opacity of helium for those models with log q(He) = −2.0. Because the radiative opacity of helium is *less* than that of carbon under white dwarf envelope conditions, such models become more transparent than others (those with log q(He) < −2.0) whose heat flow is still entirely controlled by the opacity of carbon. With further cooling, the core boundary successively crosses other levels corresponding to the various values of q(He) used in our sequence calculations. When that happens, the lower opacity of helium renders these models more transparent, divergence points arise along the curves of Figure 7, and the resulting core temperatures are lower.

It is interesting to examine briefly the effects of composition layering on the cooling curve itself. As was just described, changing the composition of the outer layers of a white dwarf model leads to variations in transparency which may affect the rate at which energy is lost during the evolution (via the L-T_c relationship). A specific example is that of the 80204L1 and 80208L1 models, whose L-T_c relationships have been plotted in Figure 6. Here we are interested in the effects of varying q(H). At relatively high luminosities, the core temperatures of models belonging to the two sequences are the same for a given luminosity. Because the thermal energy contents of such models are also the same to start with, their cooling time scales must be equal. Below a luminosity log $(L/L_\odot) \simeq -1.8$, however, the models with the thick hydrogen envelope (80204L1) experience the insulating effects of the opacity of hydrogen as discussed above. This leads to larger core temperatures with further lowering of the luminosity in these models, as observed in Figure 6. Hence, around log $(L/L_\odot) \simeq -1.8$, the 80204L1 models and the 80208L1 models have the same age and the same amount of energy in their thermal reservoirs, but the latter become more transparent to radiation with further cooling. The consequence is that the more transparent models (the ones with negligible amounts of hydrogen in the range of luminosity illustrated) evolve *more slowly* initially because they have an excess of energy to get rid of. Hence, their cooling time scales to a given luminosity are larger in this phase. With time, after the excess energy has been exhausted, such models must cool *faster* because their outer layers remain more transparent. The top two curves in Figure 8 illustrate the situation: the dashed line corresponds to the cooling curve (time versus luminosity) of the 80208L1 sequence and the continuous line to that of the 80204L1 sequence. Figure 8 indeed shows that the cooling times are the same down to log $(L/L_\odot) \simeq -1.8$, and that the more transparent models (80208L1) evolve slower until log $(L/L_\odot) \simeq -3.8$. From that point on, the same models evolve faster, but the computations have not been pursued to much lower luminosities. Nevertheless, it is clear that at very low luminosities, models with more opaque, thick hydrogen layers would take longer to evolve. These results are in excellent agreement with those of D'Antona and Mazzitelli (1987), who have discussed the same phenomenon in a slightly different context.

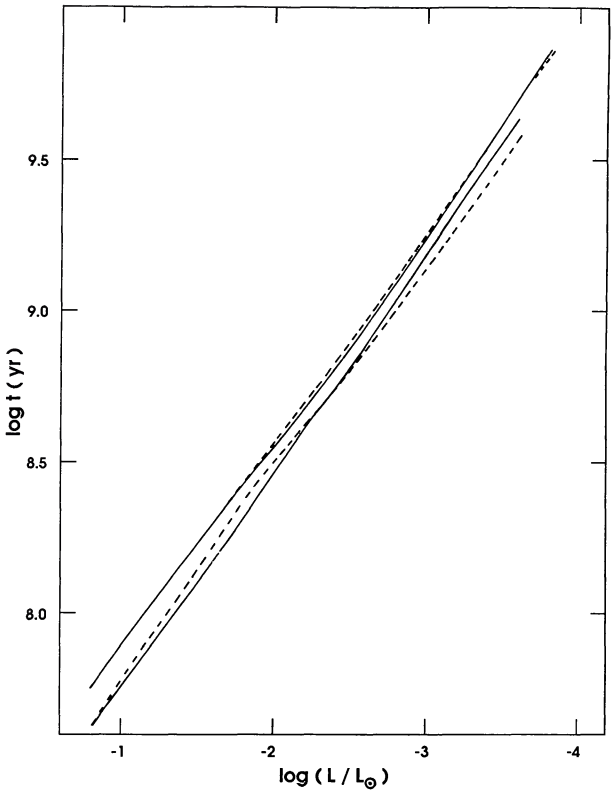

FIG. 8.—Cooling time vs. luminosity for white dwarf sequences with different values of q(H) and q(He). The top two curves correspond to 0.8 $M_\odot$ models which differ in their values of q(H): log q(H) = −4 (*continuous curve*) and log q(H) = −8 (*dashed curve*). The two lower curves refer to 0.6 $M_\odot$ models which differ in their values of q(He): log q(He) = −2 (*dashed curve*) and log q(He) = −6 (*continuous curve*).

The two lower curves shown in Figure 8 illustrate even better the effects of composition layering on the cooling curve. In this case, we are interested in the effects of varying q(He). The dashed curve corresponds to the more transparent 60208L1 models, and the continuous curve to the 60608L1 models. As in the above example, the more transparent models (with lower T_c as shown in Fig. 7) initially experience a delay in cooling in order to get rid of their excess thermal energy. Down to a luminosity log $(L/L_\odot) \simeq -0.8$, the cooling times are the same (and so are the L-T_c relationships), but there is indeed a delay in cooling for the more transparent models in the range $-0.8 \gtrsim \log (L/L_\odot) \gtrsim -2.5$. Below log $(L/L_\odot) \simeq -2.5$, the more transparent models evolve faster as shown in Figure 8 because they have lost more energy by then. Hence, our results are consistent with the rule of thumb proposed by Wood and Winget (1989) and which applies at very low luminosities: the thinner the helium layer (more opaque models), the longer the evolutionary time scale. We note that the relative delay in cooling arising from increasing the transparency of models from one sequence to another [such as decreasing q(H) and/or increasing q(He)] is of the same nature as the bump observed in the cooling curve due to convection penetrating into the degenerate core (see Fig. 3). This delay corresponds to a phase in which an excess energy is radiated away. Similarly to the case of an increased transparency of the outer layers, convection eventually does accelerate the cooling process as noted previously.

iii) *Superficial Convection Zone Structure*

An important result of the present evolutionary calculations is that we have investigated the effects of varying different parameters on the structure of the superficial convection zone which develops with cooling as the consequence of the recombination of the main atmospheric constituent (H in DA stars, He in DB objects) in an evolving white dwarf. Because detailed discussions of the behavior of the partial ionization and convection zones of white dwarfs exist in the literature (see, notably, the studies of Fontaine and Van Horn 1976 and D'Antona and Mazzitelli 1979), we focus the present discussion on the role played by convection zones in relation to the pulsation properties of white dwarfs.

Given the existence of a potent driving mechanism near the base of the superficial convection zone, one can understand, as first shown by Winget (1981), the intimate relationship between the onset of g-mode oscillations (the blue edge of the instability strip) and the location of the base of the superficial convection zone. Indeed, it has been known (cf. Cox 1980) that in order to drive instabilities, the driving regions—associated here with the base of the superficial convection zone—must be able to respond thermally on the time scale of the pulsation. In the case of interest, the thermal time scale $\tau_{\rm th}$ may be estimated by

$$\tau_{\rm th} \simeq C_V(b)\,T(b)\,q(b)\,M/L, \qquad (42)$$

where $C_V(b)$, $T(b)$, and $q(b)$ are, respectively, the specific heat at constant volume per gram, the temperature, and the mass fraction at the base of the convection zone, and where M and L are, respectively, the mass and the luminosity of the model. The blue edge of a white dwarf instability strip corresponds to the effective temperature at which the base of the superficial convection zone is sufficiently deep for the local thermal time scale to be comparable to the shortest *observable* g-mode periods. These periods are specified by the mechanical structure and, for degenerate stars in the mass range 0.4–0.8 $M_\odot$, are of the order of 100 s. Such periods would correspond to g_{13} ($k=1$, $l=3$) modes; low-order modes with $l \geq 4$ can have shorter periods than this limit for white dwarfs, but they would not be observable because of surface cancellation effects (Dziembowski 1977; Brassard 1986). Thus, detectable g-mode instabilities are possible in white dwarfs only if $\tau_{\rm th} \gtrsim$ 100 s. Because the location of the base of the convection zone depends on several parameters, it is easy to understand why the effective temperature of the blue edge can be affected.

The most important parameter in the present context is, not surprisingly, the assumed convective efficiency. To illustrate the point, Figure 9 shows the relationship between the development of a hydrogen convection zone and the growth of the thermal time scale at its base for a number of sequences of cooling DA white dwarf models having the same mass ($M = 0.6\ M_\odot$), but differing in their postulated convective efficiency. These sequences are also parameterized by log q(He) = −2 and various values of q(H). The solid lines

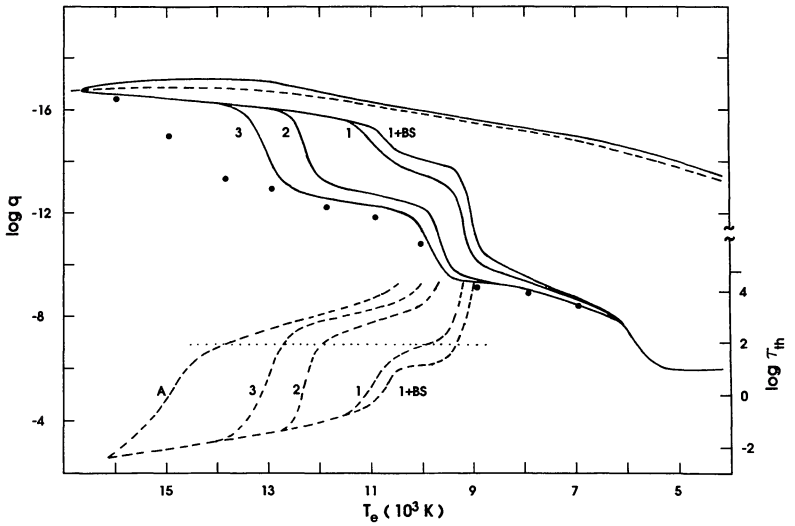

FIG. 9.—Convection zone profile (expressed in terms of the mass fraction q) and thermal time scale at the base of the convection zone vs. effective temperature for 0.6 $M_\odot$ DA sequences. The continuous curves show the extent of the superficial hydrogen convection zone for four different assumed convective efficiencies. The upper continuous curve gives the location of the top of the convection zone; it is always near the photosphere, as indicated by the upper dashed curve which gives the exact location of the photosphere ($\tau = \frac{2}{3}$). The lower continuous curves labeled "1 + BS," "1," "2," and "3" give the location of the base of the convection zone for models with an assumed convective efficiency given by the ML1 version of the mixing-length theory incorporating the Böhm-Stuckl prescription, and the ML1, ML2, and ML3 versions, respectively. The small filled circles correspond to the maximum possible extent of the convection zone as obtained from the adiabatic approximation. The set of dashed curves in the lower half of the diagram shows how the characteristic thermal time scale at the base of the convection zone increases with decreasing effective temperature. The scale is given on the lower half of the right-hand axis. The dashed curves are labeled by numbers and letters corresponding to different versions of the mixing-length theory as explained above; "A" stands for adiabatic stratification. The horizontal dotted line gives the minimal period detectable (100 s) for a nonradial pulsation in a white dwarf of average mass.

illustrate the boundaries of the convection zone given in terms of the mass fraction q as a function of effective temperature. It should be pointed out here that the hydrogen convection zone profiles do not depend on the value of q(H) as long, of course, as the layers of interest are above the H/He buffer zone. Thus, the convection zone profiles shown in Figure 9 remain appropriate for *all* 0.6 $M_\odot$ DA models until the base of the convection zone reaches $q \simeq q$(H) and H/He mixing occurs. The figure shows that the hydrogen convection zone reaches a maximum depth around $\log q \simeq -6.0$; models with a value of $\log q$(H) larger than this consequently never mix.

In our 0.6 $M_\odot$ DA models, hydrogen starts to recombine around $T_e \simeq 16{,}500$ K, which leads to the formation of a superficial convection zone from then on. With further cooling, the base of the convection zone sinks into the star as more and more hydrogen recombines and convection becomes the dominant energy transfer mechanism in the outer layers of our models. Note that the top of the superficial convection zone always stays near the photosphere ($\tau = 2/3$), whose location is given by the upper dashed curve. (The position of the photosphere changes with time because cooling changes the surface opacity, thereby allowing radiation to escape from various depths.) From a common point corresponding to the top of the convection zone, the solution of the structure equations follows various paths in the (ρ, T)-plane depending on the assumed convective efficiency. Hence, the regions of partial ionization are mapped differently, and the outcome is models with the same effective temperature having convection zones of different thicknesses. Figure 9 also shows that the base of the convection zone reaches a maximum depth, and there is a hint in the figure that it retreats toward the surface at very low effective temperatures (this tendency is more obvious in Fig. 10). The physical reason for this behavior is that the base of the convection zone eventually reaches the boundary of the degenerate core. Because of highly efficient electron conductivity, convection is suppressed in degenerate matter. With further cooling, the boundary of the degenerate core goes up toward the surface, which forces the base of the convection zone to move up also.

The continuous curves labeled "1," "2," and "3" give, respectively, the location of the base of the hydrogen convection zone for models using the ML1, ML2, and ML3 versions of the mixing-length theory. We have used data from the 60206C1 extended sequence (ML1), the 60210L2 sequence (ML2), and the 60207L3 sequence (ML3). We have found practically no differences between the hydrogen convection zone profiles of models computed with the two different sets of radiative opacities. In the case of the 60210L2 sequence, we have supplemented the evolutionary results with data coming from an envelope code (mentioned above) because these models mix around $T_e = 9600$ K and no longer represent DA white dwarfs below this value. Thus, ML2 envelope models with $\log q$(H) $= -6.0$ were computed with this code. The same envelope code was used to generate the continuous curve labeled "1 + BS." This is based on the ML1 version of the mixing-length theory but includes a refinement due to Böhm and Stuckl (1967). The refinement is introduced to make sure that the convective velocity actually vanishes at the

top of the convection zone, thus preventing overshooting; it is implemented by choosing, as the local mixing length, the smaller of the pressure scale height or the distance to the top of the convection zone. This procedure reduces the overall convective efficiency as compared with the standard ML1 version and gives rise to yet another possible structure path in the (ρ, T)-plane. We discuss this additional convection model not only to compare with our evolutionary results but, mostly, to clear up some confusion which has been introduced in the literature. Indeed, Cox *et al.* (1987) suggest that some of the differences they find between their pulsation results and those of Winget *et al.* (1982*a*) are caused by the fact that the latter authors have used models (the ones discussed here) which supposedly incorporate the Böhm and Stuckl prescription. Cox *et al.* (1987) have not included this prescription, and their convective efficiency (based on the standard treatment) is presumed to be larger than that used by Winget *et al.* (1982*a*). The fact is that Winget *et al.* (1982*a*) have used the models described in the present paper, which also do *not* include the Böhm and Stuckl prescription. The confusion may arise from the fact that the envelope code of Fontaine and Van Horn (1976) (which is not used in our evolutionary calculations but is included in the Winget, Lamb, and Van Horn evolution code) does incorporate the prescription. In any case, the source of the differences between the pulsation results of Cox *et al.* (1987) and those of Winget *et al.* (1982*a*) must be attributed to a cause other than different convective efficiencies.

Figure 9 indicates that, in the intermediate range of effective temperature, the location of the base of the superficial hydrogen convection zone can be uncertain by up to 4 orders of magnitude in q; the greater the assumed convective efficiency, the deeper the convection zone. Note, however, that the location of the base of the convection zone becomes insensitive to the free parameters of the mixing-length theory at both ends of the temperature sequence shown in the figure. At high effective temperatures, a negligible fraction of the energy flux is transported by convection. In that case, changing the efficiency of convection does not appreciably affect the stratification, which remains essentially radiative in the convection zone. At low enough effective temperatures, the temperature stratification becomes entirely adiabatic throughout the whole convection zone ($\nabla = \nabla_{ad}$), energy transport by convection reaches its most efficient state, and the temperature gradient is lowered to its minimum possible value in the zone. Again in this case, the free parameters of the mixing-length theory become irrelevant. We note in particular that, by the time a DA white dwarf has cooled to $T_e \simeq 6000$ K, the location and extent of the hydrogen convection zone are entirely insensitive to these free parameters. This has, at least, the happy consequence that cooling is never affected by the uncertainties of the mixing-length theory because the whole convection zone has become fully adiabatic by the time its base breaks into the degenerate core.

The situation for the blue edge of the DAV instability strip is quite different. In the lower half of Figure 9, we have shown how the characteristic thermal time scale at the base of the convection zone increases with decreasing temperatures. The dashed curves labeled "1+BS," "1," "2," and "3" correspond, respectively, to the convection zone structures computed with the ML1 version of the convection theory including the Böhm and Stuckl prescription and the ML1, ML2, and ML3 versions; the time scale is given on the lower half of the right-hand axis. The dotted horizontal line crossing the dashed curves gives the value of the minimum observable g-mode periods for white dwarfs, namely, ~ 100 s. As cooling proceeds, the base of the convection zone sinks into the star and the thermal time scale increases. When, for the first time, the thermal time scale becomes comparable to ~ 100 s, the star starts responding to the driving mechanism, which corresponds to the observable blue edge of the DAV strip. The intersection of the horizontal dotted line and a dashed curve gives an estimate of the effective temperature of the blue edge; clearly, there is a strong dependence here on the free parameters of the mixing-length theory. Figure 9 shows that the convective efficiencies which we have assumed in the present paper (and they are by no means exclusive) can accommodate a blue edge in the range 13,000 K $\gtrsim T_e \gtrsim$ 9500 K. The temperature of the blue edge can be increased by increasing appropriately the assumed convective efficiency of the equilibrium models. From that point of view, we must disagree with Weidemann and Koester (1984) and Cox *et al.* (1987), who suggest that current theory cannot account for an observed blue edge around $T_e \simeq 13{,}000$ K. In the pulsation analyses carried out by our own group, we never had difficulties in reconciling theory and observations, and this probably reflects some differences in the models. It should be pointed out, of course, that the game of shifting the theoretical blue edge to higher temperatures by increasing the convective efficiency has its limits. Indeed, the maximum possible extent of a convection zone is that given by the adiabatic approximation corresponding to the most efficient way of transporting energy. We have used our envelope code to generate convection zone models in the adiabatic approximation. The small filled circles in Figure 9 give the location of the base of the adiabatic convection zone; notice how these data merge nicely with our previous results at low effective temperatures. Corresponding to this new convection zone profile, we have also shown the thermal time scale curve in Figure 9 (*dashed line labeled "A"*). The figure shows that the largest possible effective temperature for the DAV blue edge is around $T_e = 14{,}000$ K according to the present evolutionary models.

Qualitatively similar results are obtained for models appropriate for DBV stars. Figure 10, which has the same format as Figure 9, summarizes our results based on the 60400L1 and 60600L3 sequences as well as complementary data obtained with our envelope code. The figure shows that superficial convection due to helium recombination starts at $T_e \simeq 65{,}000$ K in cooling 0.6 $M_\odot$ DB white dwarfs. In a way very much similar to the case of DA stars, the top of the convection zone always remains at or near the photosphere (*upper dashed line*). At the same time, the base of the convection zone sinks into the star at a rate which depends on the assumed convective efficiency. The base of the convection zone reaches a maximum depth $\log q \simeq -6.0$ around $T_e =$ 11,000 K and retreats toward the surface with further cooling. The entire convection zone has become fully adiabatic near

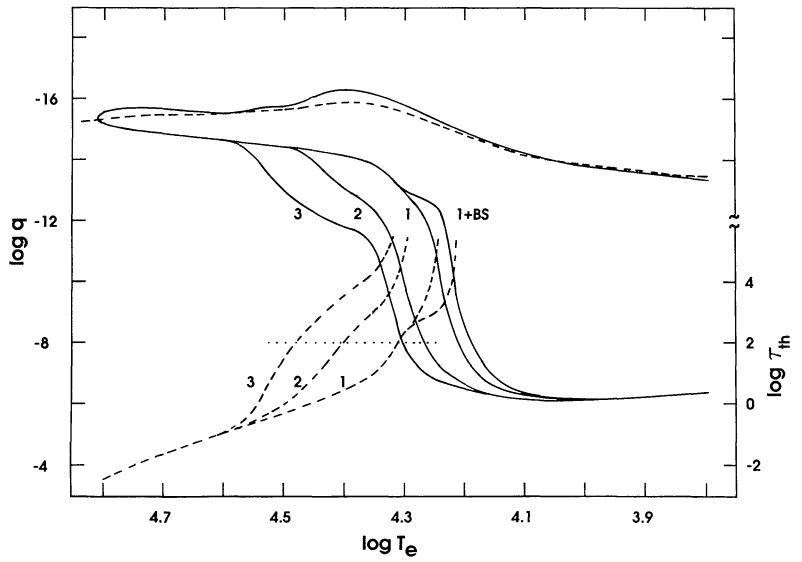

FIG. 10.—Similar to Fig. 9, but for 0.6 $M_\odot$ DB models

this effective temperature, as evidenced by the convergence of the various curves in the figure. Using the same arguments as for the DAV case, we find that the theoretical blue edge of the DBV instability strip is quite sensitive to the assumed convective efficiency; our models can accommodate a blue edge temperature varying from ~ 20,000 K (ML1) to ~ 30,000 K (ML3). Interestingly here, the Böhm and Stuckl prescription does not affect the blue edge temperature because its effects on the thermal time scale are being felt only after the time scale has grown beyond 100 s for ML1 convection.

The effects of varying the total mass of the model on the convection zone structure of DA white dwarfs are illustrated in Figure 11, which has a format similar to that of the two previous figures. We distinguish the convection zone profile of DA models with ML1 convection and $M/M_\odot = 0.8$ (*dotted curve*; 80204L1), 0.6 (*continuous curve*; 60207L1), and 0.4 (*dashed curve*; 40204L1). Generally, the more massive models have slightly shallower convection zones because their characteristically higher densities tend to favor ionization in the higher levels (cf. Fontaine and Van Horn 1976). However, at intermediate effective temperatures, there is some structure associated with the equation of state which muddles the picture somewhat, and there is no clear relationship between the location of the base of the convection zone and the mass in terms of effective temperature. (Note that the base of the convection zone of a more massive star would *always* be shallower than that of a less massive star if the convection zone profile was expressed in terms of the luminosity instead

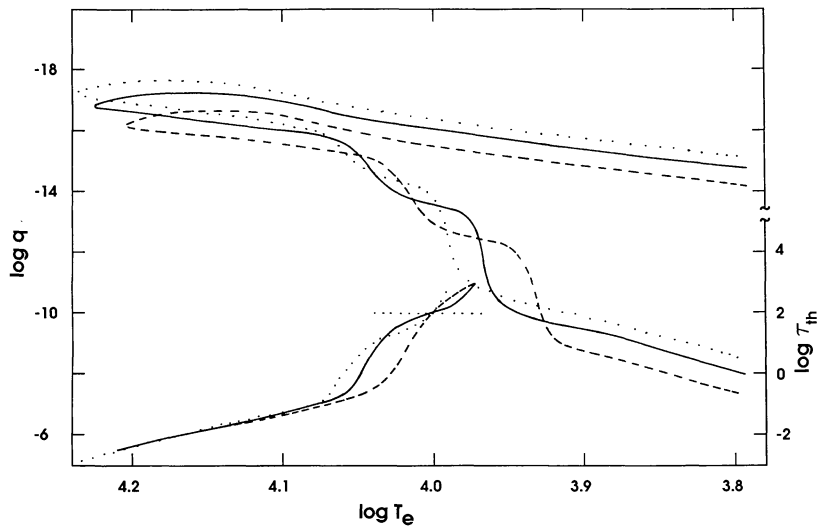

FIG. 11.—Similar to Fig. 9, but for DA models with ML1 convection and different masses. The dotted, continuous, and dashed curves correspond, respectively, to models with $M/M_\odot = 0.8$, 0.6, and 0.4.

of the effective temperatures.) Figure 11 shows that the location of the base of the convection zone is relatively insensitive (as compared with the effects of the convective efficiency) to the mass over large temperature intervals. This insensitivity is more striking at the level of the thermal time scale, which we show as a function of effective temperature in the lower half of the figure. The dotted, continuous, and dashed curves there correspond to models with $M/M_{\odot} = 0.8$, 0.6, and 0.4, respectively. At high effective temperatures, the thermal time scale appears essentially insensitive to the mass because there is an almost perfect compensating effect between a higher mass and a shallower convection zone (cf. eq. [42]). The dependence of the thermal time scale on the mass remains quite weak at lower effective temperatures and, in particular, almost vanishes again when the time scale reaches a value near 100 s. From this, we conclude that there can be only a weak dependence of the blue edge temperature on the mass of the DA model.

Figure 12 illustrates another weak effect on the convection zone structure of DB white dwarfs. The continuous line shows the boundary of the helium superficial convection zone for 60400L1 models. In comparison, the dashed curve shows the deviation from this profile brought about by our use of the older set of radiative opacities (Cox and Stewart 1970) in conjunction with our envelope code. We have already pointed out that the two sets of radiative opacity give practically the same profiles for hydrogen convection. Here, in the case of helium convection, the differences are significant, but the figure nevertheless shows that they remain small in a relative sense. Thus, we do not expect important effects on the blue edge temperature due to the use of our two different opacity sets. By and large, the largest effects are caused by the convective efficiency. This suggests that a comparison between the observed blue edge temperature and that predicted by theory could lead to an *actual calibration of the mixing-length theory in pulsating white dwarfs*. This has already been claimed by Fontaine, Tassoul, and Wesemael (1984), who find that ML3 theory for both DAV and DBV stars matches the observations very well (see also Winget *et al.* 1983).

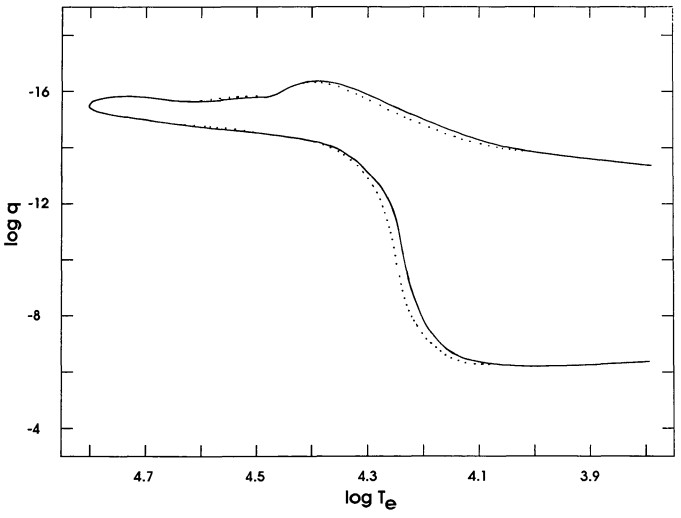

FIG. 12.—Helium convection zone profile (mass fraction vs. effective temperature) for 0.6 $M_{\odot}$ DB models computed with ML1 convection. The continuous curve corresponds to models computed with the newer set of Los Alamos radiative opacities, and the dotted curve to models computed with an older version of the opacities.

It should be pointed out in conclusion that the present thermal time scale arguments concerning the relationship between the blue edge temperature and the convective efficiency in pulsating white dwarfs can be validated only by actual pulsation calculations. Such calculations (as available) already indicate that other effects can also influence the onset of g-mode instabilities in white dwarfs. For example, according to Winget *et al.* (1982*a*), changing the value of q(H) changes the conditions for both mode trapping and the onset of the instabilities. To a large extent, however, the computations of Winget *et al.* (1982*a*) as well as those of Winget and Fontaine (1982) and Winget *et al.* (1983) have already established the basic validity of the thermal time scale arguments used in this subsection. Thus, one can have confidence in the qualitative picture presented here.

Another aspect of convection in relation to pulsating white dwarfs is the potential occurrence of mixing episodes which can change drastically the surface composition of white dwarfs. In particular, one possibility for explaining the red edge of the DAV instability strip is to assume that the hydrogen outer layer is sufficiently thin that it becomes eventually totally convective and mixes with underlying helium. When that happens, it is believed that hydrogen is completely diluted in a much more massive helium convection zone which changes the surface composition from a hydrogen-dominated to a helium-dominated one. The mechanism associated with the hydrogen partial ionization zone and responsible for driving the pulsations of DAV stars is then washed away, and presumably, this stops the oscillations. The possibility that the red edge of the DAV instability strip is associated with a mixing event is attractive, at least from the point of view of white dwarf statistics. Indeed, it has been known from some time (see Sion 1984 and references therein) that there is a strong reversal in the number ratio of DA to non-DA (He-dominated) stars in favor of He-rich white dwarfs below $T_e \simeq 10{,}000$ K. The usual explanation for this has been to invoke convective mixing, and this has been studied theoretically by Koester (1976) and Vauclair and Reisse (1977) in particular. The models which we have computed in this paper are relevant to the mixing process. However, the general problem of convective mixing in DA white dwarfs with its important potential implications for both the spectral evolution of white dwarfs and the DAV stars deserves a much more elaborate treatment than we can afford here. We postpone such a discussion to a later publication and restrict ourselves to a few brief comments in what follows.

We have already pointed out that superficial convection zones always reach a maximum depth in models of evolving white dwarfs as the result of the encounter between the base of the convection zone and the degeneracy boundary. For example, Figure 9 shows that the hydrogen convection zone reaches a maximum depth at $\log q \simeq -6.0$. The potential for mixing therefore exists for any stratified DA model which has a value of $\log q$(H) less than this limit. For models with the thinnest hydrogen outer layers, mixing is facilitated by the

presence of a subphotospheric helium convection zone below the H/He transition zone. We find that such a subphotospheric convection zone is significant only for models with $\log q(\mathrm{H}) \leq -12.0$. In that case, the mixing process is initiated by the merging of the H and He convection zones. The subphotospheric helium convection zone is basically negligible in extent for models with larger values of $\log q(\mathrm{H})$ and disappears completely for models with $\log q(\mathrm{H}) \geq -8.0$. Nevertheless, efficient mixing still occurs when the hydrogen outer layer becomes fully convective, since the latter event induces convection to penetrate rapidly into the He-rich regions. We have not followed the subsequent evolution of the surface composition in the present calculations because our primary goal has been the construction of models appropriate for pulsation studies. As an interesting by-product, however, we have obtained the values of the effective temperature at which mixing occurs in DA white dwarfs in terms of several parameters. These are listed under the heading $T_e(\mathrm{m})$ in Table 2. The mixing temperatures are those of the *first* models which show a merging of the H and He convection zones or which show convection penetrating completely through the H/He transition zone in given evolutionary sequences. Note that the mixing temperature is the same for models of the same mass, computed with the same convective efficiency, and with the same value of $\log q(\mathrm{H})$. It does not depend on the value of $\log q(\mathrm{He})$ in DA models. The small variations of $T_e(\mathrm{m})$ shown in Table 2 for models which differ only by their values of $\log q(\mathrm{He})$ are not significant and are simply caused by the fact that the effective temperatures of models belonging to different sequences are not the same.

The dashed curve in Figure 13 gives the effective temperature at which mixing occurs in terms of the hydrogen layer thickness [$\log q(\mathrm{H})$] for 0.6 $M_\odot$ models computed with ML1 convection. The arrows correspond to the increase in mixing temperature in the case where the ML3 version of the mixing-length theory is used for models with $\log q(\mathrm{H}) = -10$ and -9. The curve should extend to lower values of $\log q(\mathrm{H})$ and $T_e(\mathrm{m})$, since mixing can occur for $\log q(\mathrm{H}) \lesssim -6.0$ as indicated previously. We have no actual data for these low temperatures because we have generally stopped our evolutionary calculations at $\log T_e = 3.8$ ($T_e \simeq 6300$ K). However, an examination of Figure 9 suggests that mixing is just possible for $\log q(\mathrm{H}) \simeq -6.0$ at $T_e \simeq 5000$ K. The dashed curve in Figure 13 shows that DA white dwarfs with a spectrum of hydrogen layer mass $-14 \lesssim \log q(\mathrm{H}) \lesssim -8$ may gradually turn into He-rich stars over an effective temperature interval 11,000 K $\gtrsim T_e \gtrsim$ 6000 K. At the same time, it also reveals that if the mixing hypothesis is to be retained to account for the red edge of the DAV instability strip, only models with very thin hydrogen layers *and* efficient convection could pass the test. Clearly, more detailed studies of this important issue are required.

For completeness, we have also plotted in Figure 13 (*continuous curve*) the mixing temperature of DB models as a function of $\log q(\mathrm{He})$ for the 0.6 $M_\odot$ ML1 models of Table 3. By direct analogy with the case of DA stars, we can expect mixing episodes in the outer layers of DB stars if the value of $\log q(\mathrm{He})$ is smaller than the maximum depth reached by the superficial helium convection zone. Figure 10, for example,

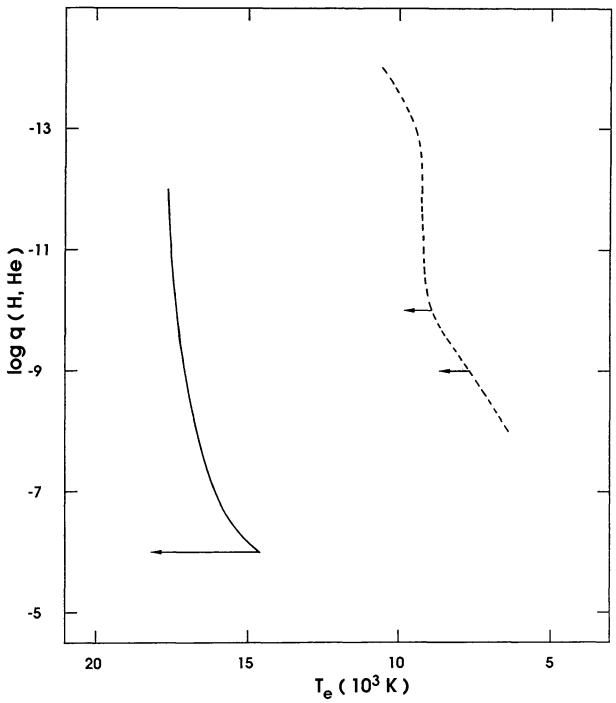

FIG. 13.—Relationship between the mass of the hydrogen layer (*dashed curve*) and the effective temperature below which H/He mixing occurs in 0.6 $M_\odot$ DA white dwarfs computed with ML1 convection. A similar relationship is shown (*continuous curve*) for 0.6 $M_\odot$ DB models corresponding to He/C convective mixing. The effect of using ML3 convection is to push the mixing temperature to higher values, as indicated by the arrows.

shows that helium convection reaches a maximum depth of $\log q \simeq -6.0$ around $T_e = 11{,}000$ K. Because of the presence of a transition zone, our results show that mixing just barely occurs in models with $\log q(\mathrm{He}) = -6.0$ at $T_e \simeq 14{,}600$ K. This temperature is increased to $\sim 18{,}000$ K if ML3 convection is used, as indicated by the arrow in Figure 13. Contrary to the DA case, however, the mixing hypothesis is not at all attractive for DB objects. From a pulsation point of view, the mixing temperature is much too low to be associated with the red edge of the DBV strip. More important, however, is the fact that mixing would produce stars with carbon-dominated atmospheres in an effective temperature range where spectroscopic carbon features would become very prominent. The fact that a white dwarf with a carbon-dominated atmosphere has yet to be discovered suggests strongly that He/C mixing does not occur in real white dwarfs. This implies $\log q(\mathrm{He}) > -6.0$ according to our calculations. At the same time, the red edge must be associated with a mechanism other than convective mixing. In fact, a theoretical red edge has been found by Winget *et al.* (1983) for DBV stars, and the idea that long-period modes are damped by energy leakage in the outer layers appears to be the basic physical explanation (Hansen, Winget, and Kawaler 1985).

b) Evolution of Key Variables

It is of interest to discuss in detail the evolution of the many variables (see Table 1) which enter into the computa-

tions of the pulsation properties of white dwarf models, in order to obtain a good qualitative understanding of these basic ingredients. At the same time, such a discussion provides a description of the main features of white dwarf evolution at intermediate luminosities. We have chosen to represent the temporal behaviors of the variables in terms of the effective temperature T_e, and the spatial behaviors in terms of the mass fraction $\log q$. Note that, in the latter case, this variable strongly emphasizes the outer layers. From the point of view of pulsation theory, these are the important regions because large-amplitude oscillations and driving are confined there. In terms of the independent variables T_e and $\log q$, the many quantities listed in Table 1 define as many surfaces, which may have quite complex structures. For a minority of variables (such as, for example, temperature, density, and pressure), their behaviors are sufficiently simple that they can be described by ordinary two-dimensional representations. For other variables, however, we have found it not only very instructive but also essential to use three-dimensional representations of their surfaces over the $(T_e, \log q)$-plane. We use both approaches in this subsection; cgs units are used throughout.

As representative cases, we have decided to discuss the results for two typical sequences: The 60510L1 sequence is appropriate for evolving DA models which eventually mix (it extends down to $T_e \simeq 9000$ K, where H/He mixing occurs). The evolution of DB white dwarfs is typified by the 60400L1 sequence, which features no convective mixing and extends to the crystallization phase. For the three-dimensional representations of the 60510L1 sequence models (see Table 2), we have picked 52 stored models starting with model 56 ($T_e =$ 54,200 K; $L/L_\odot = 1.81$) and ending with model 275 ($T_e = 8630$ K; $L/L_\odot = 7.62 \times 10^{-4}$). For the case of the 60400L1 sequence, we have picked 61 models (see Table 3) starting with model 88 ($T_e = 52{,}330$ K; $L/L_\odot = 1.49$) and ending with model 305 ($T_e = 6266$ K; $L/L_\odot = 2.09 \times 10^{-4}$). For the two-dimensional representations, the density of selected models is too high (the curves would overlap), and we consequently picked about one model out of three in such cases. Thus, we have retained subsets of 19 and 21 models for the 60510L1 and 60400L1 sequences, respectively. Table 4 lists the numbers and effective temperatures of these models. Note that the spacing in T_e is not uniform. In the following, the results will generally be presented as pairs of figures, *a* referring to the 60510L1 sequence, and *b* referring to the 60400L1 sequence.

The temperature profiles from the center ($\log q = 0$) to the surface are illustrated in Figures 14*a* and 14*b*. As expected from purely cooling objects (and according to the basic hypotheses discussed in § II*a*), the behavior of the temperature is strictly monotonic both with depth and with time. Hence, the lowest curve in each figure corresponds to the temperature profile of the model of the appropriate subset with the lowest effective temperature. Several features of the temperature profiles are worthy of comment. First, one can note how cooling flattens the temperature gradient in the core region containing some 99% of the mass of the star ($\log q \gtrsim -2$). This is due, of course, to the efficiency of degenerate electron conductivity, which increases with cooling. Cooling also leads to the recombination of the main atmospheric constituent,

TABLE 4

EFFECTIVE TEMPERATURES OF SELECTED MODELS: TWO-DIMENSIONAL REPRESENTATIONS

Model Number	T_e	Model Number	T_e
Sequence 60510L1		Sequence 60400L1	
56	54200	88	52330
68	47318	100	45379
80	40947	111	39686
92	35370	120	36531
104	33223	132	33515
116	32982	144	33265
128	30271	152	31573
140	30061	164	27919
152	27209	176	27277
164	23309	188	23567
176	19961	196	21278
184	17989	208	18482
195	15882	220	17317
204	14100	232	16225
216	12057	240	14922
228	11267	252	12759
239	10917	264	10886
248	10290	276	9280
260	9344	284	8360
		296	7124
		305	6266

which increases the opacity of the matter in the outer layers, ultimately giving rise to superficial convection zones. The temperature profiles in such convection zones are distinctly different from those found in radiative regions, as can be observed in the figures. For example, the first 12 hotter models in Figure 14*a* (models 56 through 184, sequence 60510L1) are fully radiative. (Note that in this case we have only retained data for $\log q \geq -14$.) The temperature profiles in the outer layers of these models are very similar, showing a continuous and monotonic behavior with time. As indicated previously, hydrogen starts to recombine around $T_e \simeq 16{,}500$ K in evolving 0.6 $M_\odot$ DA white dwarfs, which leads to the formation of a superficial convection zone from then on. The seven cooler models in Figure 14*a* (models 195 through 260, sequence 60510L1) show how the growing convection zone affects the temperature stratification in the outer layers. The coolest model (No. 260, $T_e = 9344$ K) has a hydrogen superficial convection zone extending to $\log q \simeq -11.6$. A surface value $\log q_s = -17.5$ was chosen for the cooler models in order to include both the photosphere ($\tau = \frac{2}{3}$) and the top of the convection zone in the Henyey "interior" (see § II*b*). The nearly isothermal part of the temperature profiles of these cooler models near the surface corresponds to the optically thin, radiative regions of the upper atmosphere.

In the case of the DB models (Fig. 14*b*), a thin surface convection zone due to the recombination of helium already exists in the hottest model considered (model 88; $T_e = 52{,}330$ K). The figure illustrates clearly the subsequent effects of convection on the temperature profiles in the outer layers. Here, a surface value $\log q_s = -16$ (-17) has been used for the hotter (cooler) models. Again, these values correspond to the optically thin, radiative regions of the upper atmosphere. One qualitative difference between the cooler models of Fig-

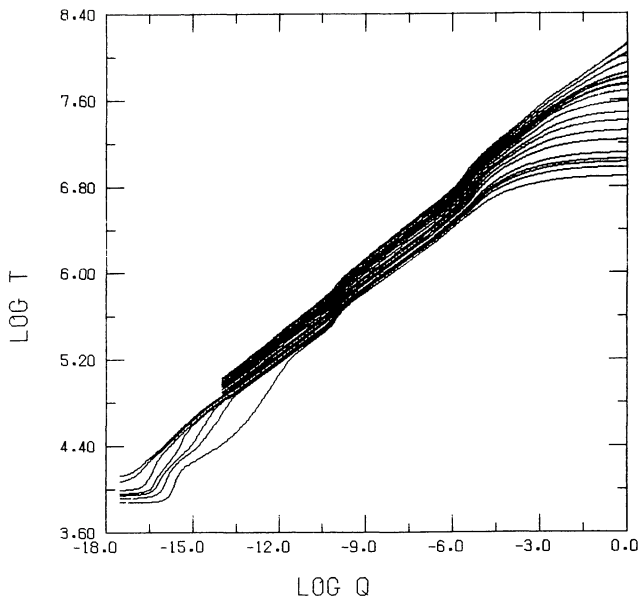

FIG. 14*a*

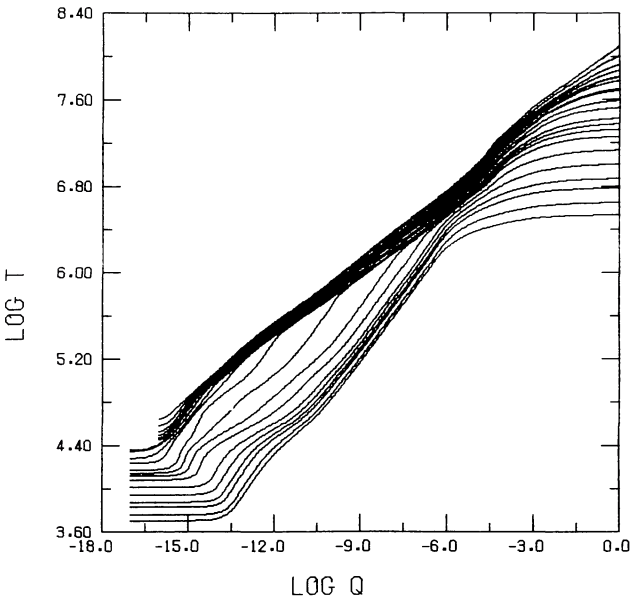

FIG. 14*b*

FIG. 14.—(*a*) Temperature profiles for 19 models belonging to the 60510L1 sequence. (*b*) Temperature profiles for 21 models belonging to the 60400L1 sequence.

ure 14*b* and those of the previous figure is that they are sufficiently evolved and possess such a thick convection zone (extending to $\log q \simeq -6.2$) that convective transport plays a major role in their evolution. Indeed, the energy flow from the nearly isothermal core to the surface is specified by a convective solution in such models. By contrast, the coolest model shown in Figure 14*a* is still too hot for convection to have developed sufficiently to reach into the degenerate core. As discussed previously, the consequence is that the model still evolves as if its outer layers were radiative. Hence, convection does not affect cooling in the effective temperature range illustrated in Figure 14*a*, but the exact temperature stratification in the outer layers remains quite critical for pulsation studies.

A final remark about the temperature profiles is that the figures show some small structure associated with the composition transition zones. With increasing depth, the temperature increases slightly in the H/He transition zone ($\log q \simeq -10$) of the 60510L1 models. Likewise, there is a similar effect present in the He/C transition zone of both the DA ($\log q \simeq -5$) and DB ($\log q \simeq -4$) models, although it tends to disappear with cooling in that case. This structure is related to an opacity effect and is discussed more fully below.

Figures 15*a* and 15*b* show the density profiles. Corresponding to a monotonic decrease of the temperature with cooling at a given shell, there is a monotonic increase of the density. We note that the presence of a superficial convection zone modifies substantially the density stratification in the outer layers of cooler models. Also, there is a significant change of density in the H/He transition zone of the 60510L1 models due to the corresponding change in mean molecular weight. The effect is much reduced in the He/C buffer zone (both DA and DB models) because the difference of mean molecular weights between helium and carbon is smaller than that between hydrogen and helium. The density profiles in the deep core region do not change very much with cooling. What we observe in this region is a small density increase at a given shell corresponding to residual contraction and to an evolution toward the completely degenerate configuration. This behavior is quite different from that of the temperature profiles and illustrates, of course, the decoupling of the question of the thermal energy content (specified by the ionic system) from the question of the mechanical structure (specified by degenerate electrons).

Figures 16*a* and 16*b* show the pressure profiles. Here the vertical scale is such that the curves are confused, but we can nevertheless distinguish that cooling corresponds to a monotonic increase of the pressure at a given shell. As expected, this qualitative behavior is the same as that of the density, to which the pressure is directly tied via the equation of state. The mechanical structure equations show that the pressure P is directly proportional to the mass function q in the outer layers of a star where the variations of gravity can be neglected. The present figures demonstrate that this direct proportionality is very well verified in white dwarfs down to a depth $\log q \simeq -2$.

A more sensible way to present the effects of cooling on the pressure is to plot not the pressure itself but the pressure scale height H_P [$= -P/(dP/dr)$] as a function of the mass fraction q. This is shown in Figures 17*a* and 17*b*, where we have naturally excluded the central value of H_P, since it is infinite. Because the models illustrated have been computed with the ML1 version of the mixing-length theory, H_P also represents the adopted mixing length itself in the convection zones. The figures show that the pressure scale height decreases monotonically with cooling at a given shell. Hence, larger local pres-

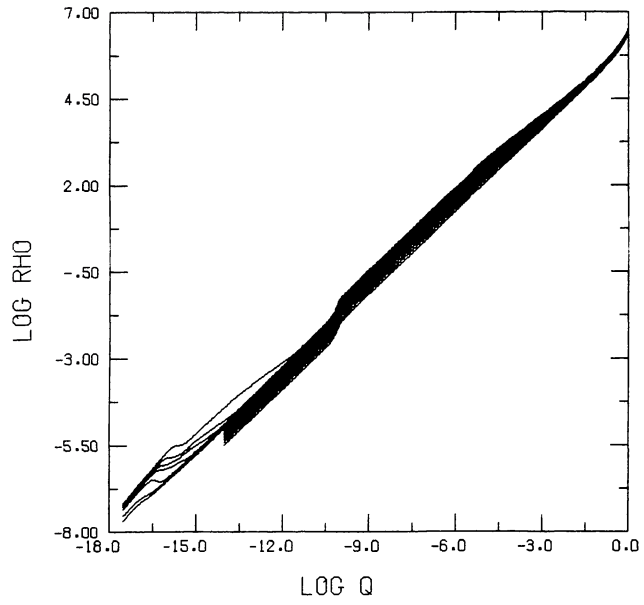

FIG. 15*a*

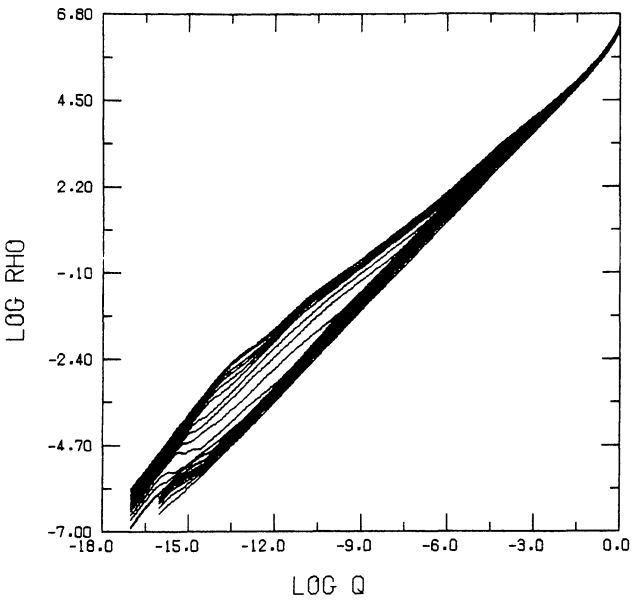

FIG. 15*b*

FIG. 15.—(*a*) Same as Fig. 14*a*, but for density profiles. (*b*) Same as Fig. 14*b*, but for density profiles.

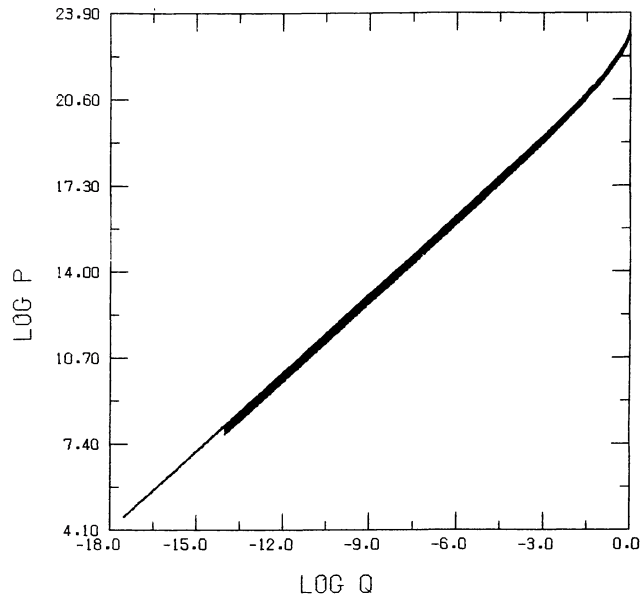

FIG. 16*a*

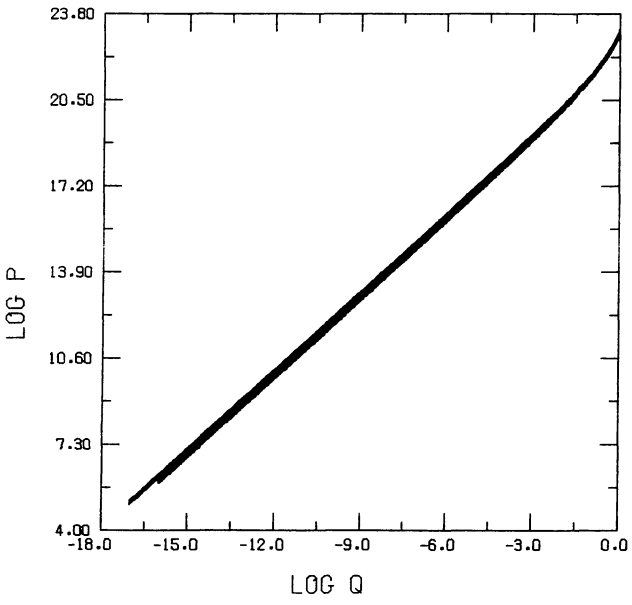

FIG. 16*b*

FIG. 16.—(*a*) Same as Fig. 14*a*, but for pressure profiles. (*b*) Same as Fig. 14*b*, but for pressure profiles.

sure gradients are built up which correspond to residual contraction. Obvious structure is associated with the convection zones, as well as with the composition transition zones (especially with H/He buffer zone). Finally, the approach to a fully degenerate configuration in the deep core is also evident.

It was previously stated that ionized material (either H or He) at the surface of a white dwarf eventually recombines with cooling. A partial ionization zone thus develops near the surface. A first consequence of this is that the opacity of the matter in the partial ionization zone increases considerably because bound-free transitions are quite efficient at absorbing photons. This large increase of the opacity in the outer layers of evolving white dwarfs is illustrated in Figures 18*a* and 18*b*. To distinguish the various models in these figures, we note that the behavior of the opacity in the core region is monotonic; there, the total opacity is dominated by the conductive

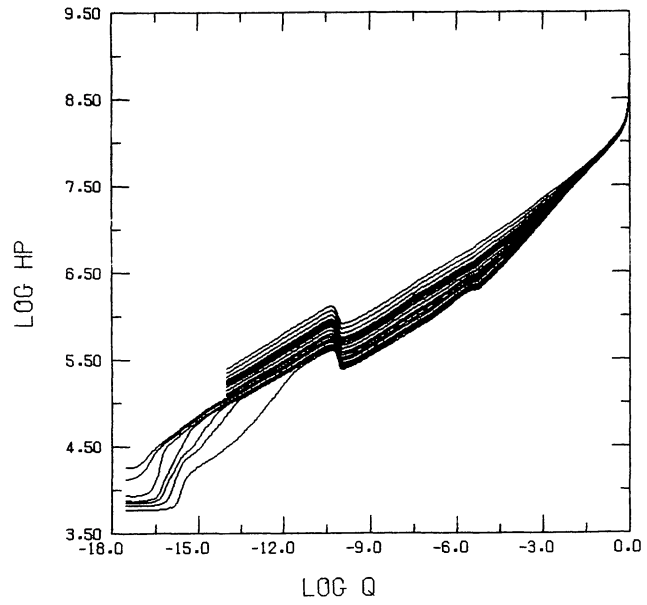

FIG. 17*a*

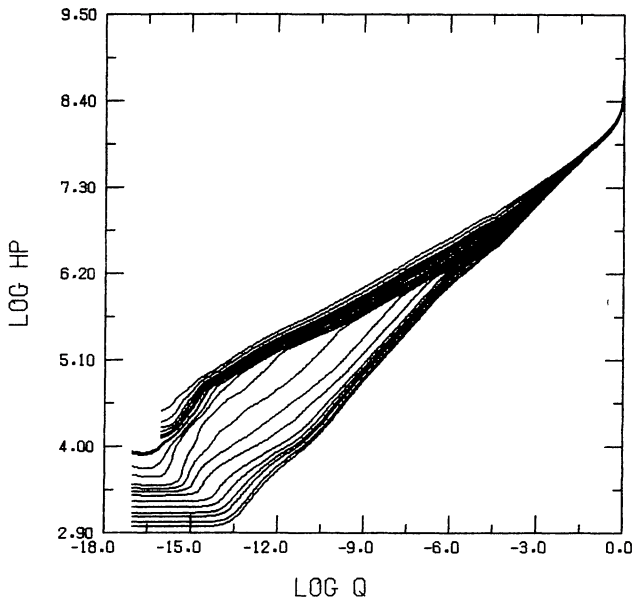

FIG. 17*b*

FIG. 17.—(*a*) Same as Fig. 14*a*, but for pressure scale height profiles. (*b*) Same as Fig. 14*b*, but for pressure scale height profiles.

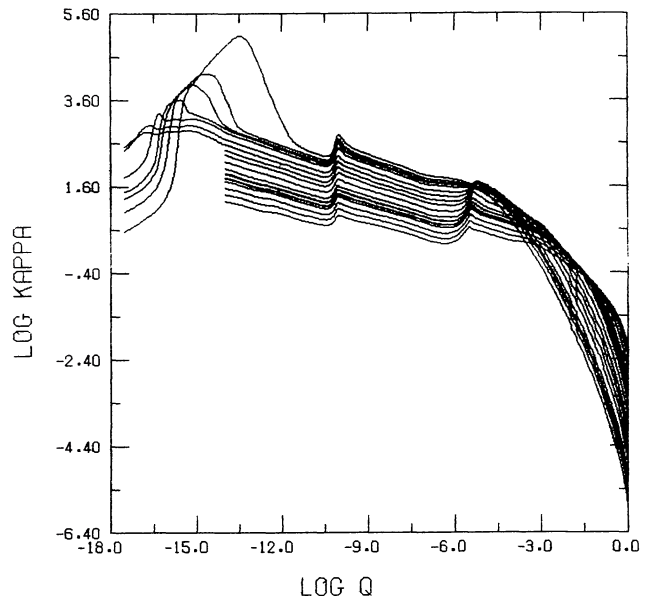

FIG. 18*a*

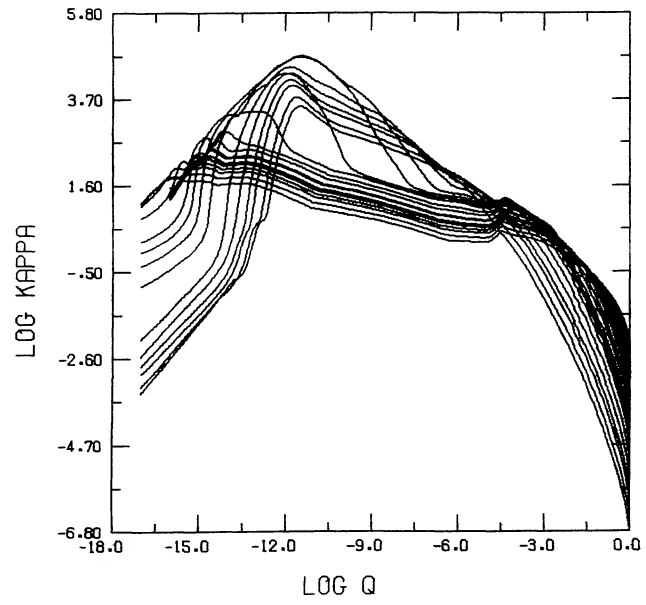

FIG. 18*b*

FIG. 18.—(*a*) Same as Fig. 14*a*, but for opacity profiles. (*b*) Same as Fig. 14*b*, but for opacity profiles.

opacity of degenerate electrons, and cooling leads to a decrease of the local opacity. Hence, the model with the lowest effective temperature corresponds to the curve with the lowest opacity in the core region ($\log q \gtrsim -2$).

Except for the outermost layers, Figure 18*a* shows clearly how the opacity of the envelope of stratified 60510L1 models increases with cooling. It reaches a maximum value in the hydrogen outer layer of the coolest model considered here (No. 260, $T_e = 9344$ K). Note also the substantial increase of the opacity going through the H/He transition zone ($\log q \simeq -10$) from the surface. This feature is responsible for the increase of the temperature in this same region, as discussed previously and observed in Figure 14*a*. The reason the opacity increases there is that hydrogen is completely ionized in our models by the time the top of the transition zone is reached. By contrast, the ionization of helium is not quite

complete in the transition zone, which implies (through the residual effects of bound-free transitions) that its opacity remains larger than that of hydrogen. It is important to realize that this effect decreases in magnitude (and even reverses) the deeper the H/He transition zone. Indeed, for deep enough H/He transition zones ($\log q \gtrsim -7$), when both hydrogen and helium are completely ionized, the radiative opacity becomes dominated by free-free transitions (the Kramers regime). In that case, helium becomes more transparent than hydrogen. We have encountered such a situation in our discussion of the effects of composition layering on the L-T_c relationship in § II*a*(ii).

Both Figure 18*a* and Figure 18*b* also show that the opacity increases through the He/C transition zone with increasing depth. Under the conditions of interest, this is not surprising, because both the radiative (in the Kramers regime) and the conductive opacity of carbon are larger than those of helium. The opacity increase is responsible for the slight temperature increase in the He/C transition zones observed in Figures 14*a* and 14*b*. We note that the effect tends to be washed away in the cooler models, where the opacity in the transition zone is specified by degenerate electron conductivity and where the differences between the conductive opacities of carbon and helium are minimal. A final remark about the opacity profiles concerns the maximum opacity reached during the evolution. For example, Figure 18*b* shows that the opacity in the outer layers generally increases with decreasing effective temperature in the hot phases of the evolution, reaches a maximum, and subsequently decreases with further cooling. The maximum opacity obtained is for models with $T_e \simeq 16{,}000$ K. A similar effect is found in models with thick hydrogen layers where the hydrogen opacity reaches a maximum value in those models with $T_e \simeq 7000$ K. It is significant that the effective temperature at the blue edge of the instability strips ($T_e \simeq 20{,}000$ K for DB stars and $T_e \simeq 10{,}000$ K for DA stars; ML1 convection) corresponds to a phase immediately preceding the phase of maximum opacity.

A second consequence of the development of a partial ionization zone in the outer layers of an evolving white dwarf is the lowering of the adiabatic temperature gradient ∇_{ad} in such a zone. This is illustrated in Figures 19*a* and 19*b*, where we use a three-dimensional projection because the profiles would get hopelessly confused in a two-dimensional representation. Here we use the full set of 52 (61) models in Figure 19*a* (19*b*); each continuous curve corresponds to the adiabatic temperature gradient profile of one particular model. Note that the distribution of models in terms of $\log T_e$ is not uniform. For an ionized (or neutral) ideal gas in which radiation is not important, ∇_{ad} assumes a value of 0.4, and we recognize large areas of the ∇_{ad} surfaces where this is verified (particularly in the hotter models). In the presence of Coulombic interactions (even for totally ionized matter), ∇_{ad} assumes values somewhat smaller than 0.4, and this is found in the core region of hot models where departures from an ideal gas behavior are not totally negligible, and in the envelope and core region of cooler models (below the partial ionization region). The small structure present on both surfaces for $\log q \simeq -2$ corresponds to the matching region between the tabular envelope equation of state and the analytic fits (third part; see § II*c*[i]) used to describe the high-density, high-temperature regime. Some very weak structure associated with composition transition zones can also be observed. Of course, the most important features of the ∇_{ad} surfaces are the "valleys" corresponding to regions of partial ionization. In this respect, Figure 19*b* is particularly illuminating. At high effective temperatures, we can easily distinguish two valleys corresponding respectively to the ionization zone of He I–He II (*upper region*) and that of He II–He III (*lower region*). These two ionization zones of helium merge together in cooler models when pressure ionization becomes important

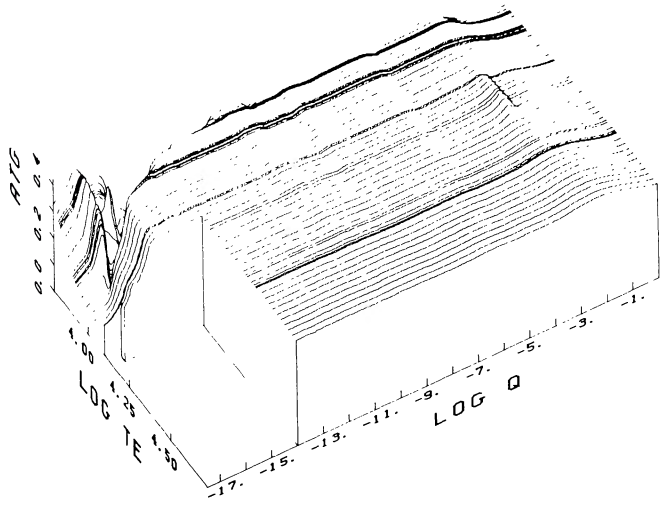

FIG. 19*a*

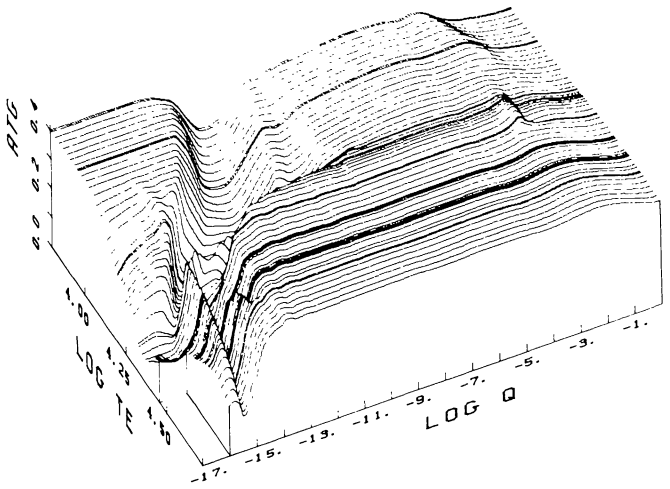

FIG. 19*b*

FIG. 19.—(*a*) Three-dimensional representation of the evolution of the adiabatic temperature gradient profiles for 52 models belonging to the 60510L1 sequence. (*b*) Three-dimensional representation of the evolution of the adiabatic temperature gradient profiles for 61 models belonging to the 60400L1 sequence.

(see Fontaine and Van Horn 1976). The resulting broad valley maps very well the region of partial ionization in these cooler models. Note in particular how the partial ionization zone moves down into the star with decreasing effective temperature. The recombination of hydrogen at low effective temperatures also leads, of course, to the formation of a valley which corresponds to the partial ionization zone of hydrogen in an evolving DA white dwarf (see Fig. 19*a*).

The combination of an increased opacity and a decreased adiabatic temperature gradient in the partial ionization zone of a cooling white dwarf naturally favors convection in this region according to the Schwarzschild criterion. In this respect, it is interesting to examine the true temperature gradient (∇) surfaces. As shown in Figures 20*a* and 20*b*, these surfaces are somewhat complex, but it is quite instructive to examine them. First, at large depths (and for high effective temperatures in the 60510L1 models), radiative and conductive transport specifies uniquely the temperature gradient profiles. In such cases the temperature gradient is directly related to the opacity distribution (see Figs. 18*a* and 18*b*). Note in particular the ridges in the ∇ surfaces associated with the composition transition zones. Note also how the He/C ridge decreases in magnitude in the cooler, more evolved models in which the differences between the conductive opacities of helium and carbon (which now dominate) become less pronounced than those between the radiative opacities.

Convective transport is responsible for the complex structure of the temperature gradient surfaces in the outer layers of the cooler models. If we focus for one moment on the DB models (Fig. 20*b*), we find that the superficial convection zone of helium corresponds to the plateau region in which the opacity is very large. The general shape of the ∇ profiles in this region can be qualitatively understood as follows. Let us consider, for example, a model with $T_e \simeq 10{,}000$ K. In the optically thin, radiative atmospheric layers, the temperature gradient is quite small (this corresponds to the low-lying regions which we can see through the peaks in the surface). With increasing depth, the opacity increases substantially in such a model, which forces ∇ to assume increasingly large values. With further increase of the opacity with increasing depth, the temperature gradient becomes so large that convection becomes a more efficient way of transporting energy than radiation. In somewhat deeper layers, the high density of white dwarf matter forces the convective solution to assume its most efficient state, i.e., to assume an adiabatic stratification. Thus, in the top layers of the convection zone, the temperature gradient goes through its maximum values (the peaks that we see in the figure) and eventually becomes almost equal to the adiabatic temperature gradient (compare with Fig. 19*b*). Convection ceases when the opacity has declined sufficiently for radiative (and conductive) transport to take over. In the cooler models in particular, this transition is rather sharp and is responsible for the sudden decrease of the temperature gradient (around $\log q \simeq -6$). This produces an obvious "cliff" in the ∇ surface which defines very well the base of the convection zone. Similar considerations apply to the 60510L1 sequence, but the effects are less apparent because the convective region is less extended.

Figures 21*a* and 21*b* illustrate the evolution of the radiative luminosity profile ($L_{\rm rad}$) and indicate how much flux is transported by convection in the outer layers of cooler white dwarf models. Of course, we have excluded the central value ($L_{\rm rad} = 0$) from these plots. Also, as expected, the radiative luminosity of a white dwarf model of a given effective temperature is essentially constant in the envelope ($\log q \lesssim -2$), with the exception of potential convection zones. The development of a superficial convection zone due to the recombination of hydrogen in an evolving 0.6 $M_\odot$ DA white dwarf model is shown in Figure 21*a*. In this particular example, a tiny subphotospheric helium convection zone associated with the opacity bump of Figure 18*a* also develops just below the H/He transition zone ($\log q \simeq -10$). Eventually, these two

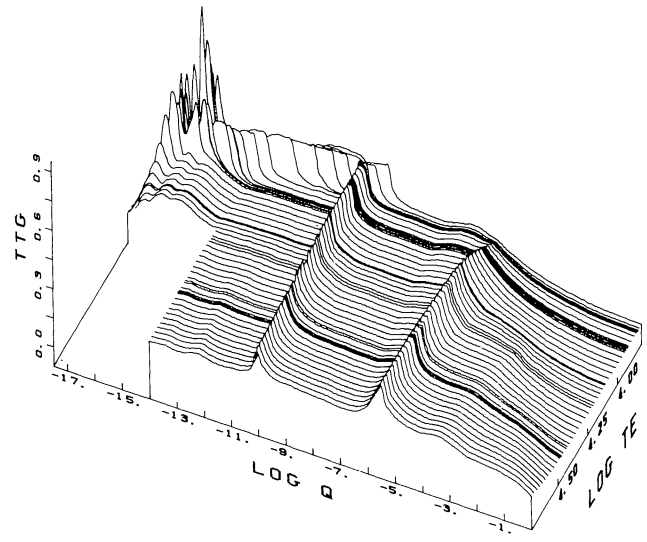

FIG. 20*a*

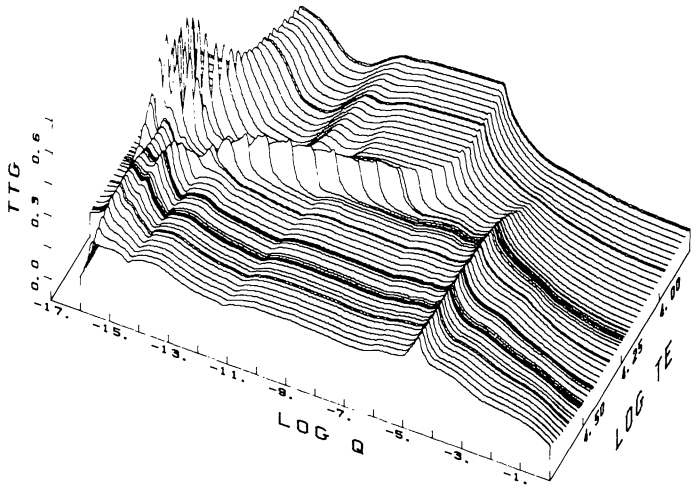

FIG. 20*b*

FIG. 20.—(*a*) Same as Fig. 19*a*, but for the true temperature gradient. (*b*) Same as Fig. 19*b*, but for the true temperature gradient.

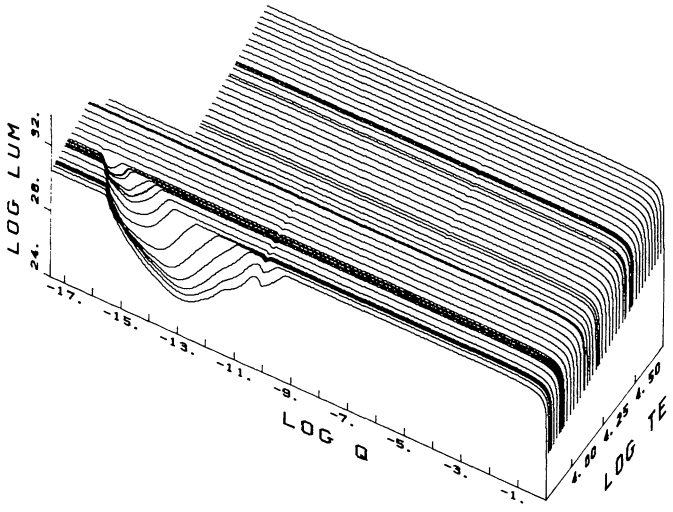

FIG. 21*a*

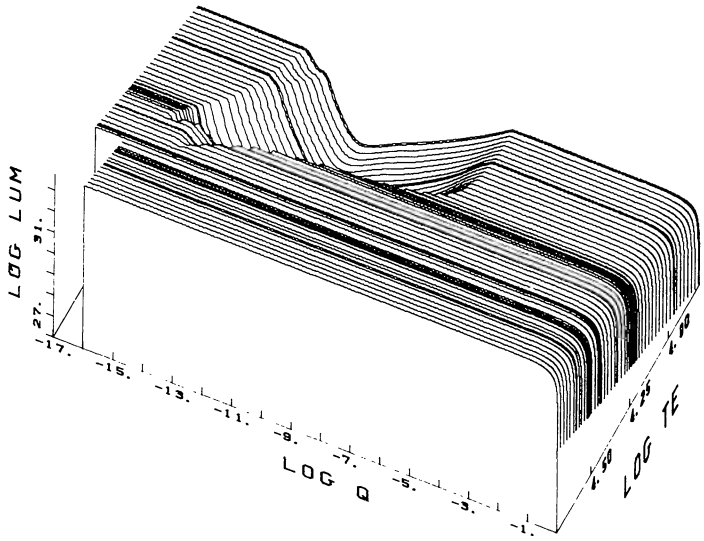

FIG. 21*b*

FIG. 21.—(*a*) Same as Fig. 19*a*, but for the radiative luminosity. (*b*) Same as Fig. 19*b*, but for the radiative luminosity.

zones merge together and H/He mixing occurs. The two coolest models plotted in Figure 21*a* show such a merging. There is also a hint in the figure of the temporary existence of a very weak carbon convection zone associated with the opacity bump in the He/C transition zone. The effects of this small convection zone on the structure and evolution of the model are totally negligible. For the 60400L1 models (Fig. 21*b*), the He/C transition zone is located deeper and no carbon convection zone is present. The figure, viewed from another angle, shows how the superficial helium convection zone develops in DB models. Note the initial existence of two distinct convection zones (corresponding to the two ionization zones of helium) which eventually merge together.

Because the question of the radiative luminosity is quite important from the point of view of pulsation theory, we feel it is useful to present the same data in a more quantitative form. This is possible using our two-dimensional representation of the subsets of models (see Table 4), since the radiative luminosity surfaces are rather simple. The results are summarized in Figures 22*a* and 22*b*. In both cases the cooler models

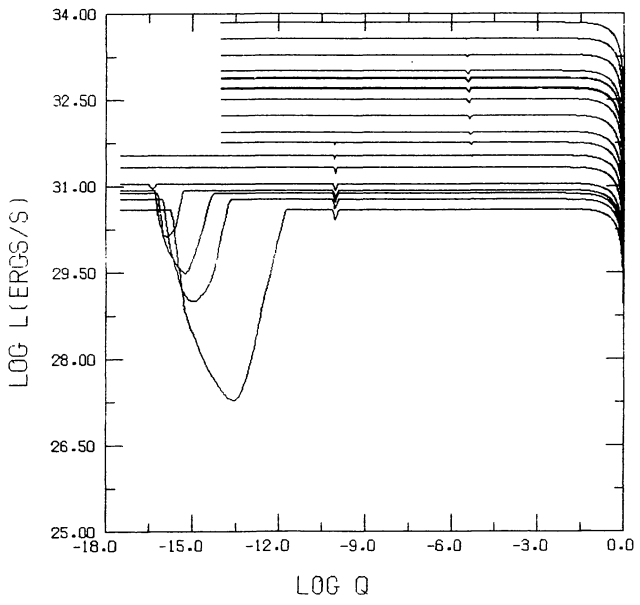

FIG. 22*a*

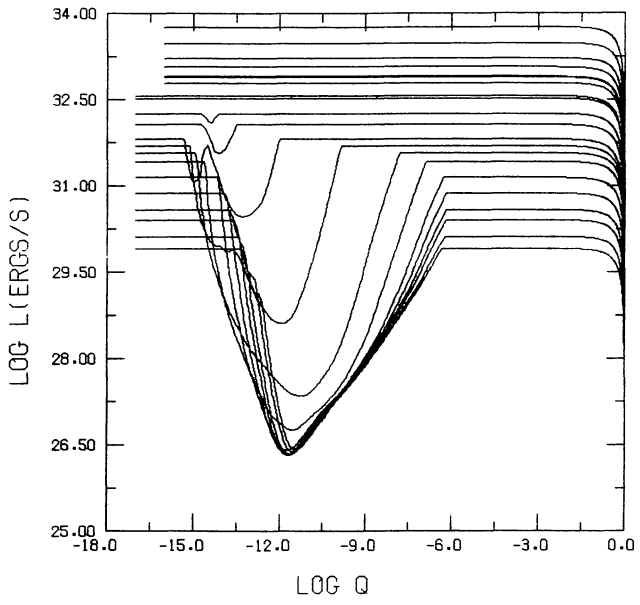

FIG. 22*b*

FIG. 22.—(*a*) Same as Fig. 14*a*, but for radiative luminosity profiles. (*b*) Same as Fig. 14*b*, but for radiative luminosity profiles.

are characterized by an extensive superficial convection zone which carries a substantial fraction of the energy flux. The actual radiative luminosity profiles are used in nonadiabatic pulsation calculations. Note that the convective flux $F_c = (L - L_{\rm rad})/4\pi r^2$, so that an explicit discussion of the behavior of F_c would be redundant here.

To complete the discussion of convection zone properties in evolving white dwarfs, we show in Figures 23*a* and 23*b* the convective velocity surfaces. A thorough discussion of the behavior of the convective velocity in white dwarfs has already been presented by Fontaine and Van Horn (1976) and will not be repeated here. Suffice it to say that the convective velocity goes through a maximum as a function of depth ($\log q$) and as a function of time (T_e). In the particular sequences illustrated here and computed with the ML1 version of the mixing-length theory, the convective velocity reaches a maximum value of $\sim 3.4\times10^5$ cm s^{-1} in the hydrogen convection zone of a 60510L1 model with $T_e \simeq 9000$ K, while it reaches a somewhat smaller value of $\sim 2.7\times10^5$ cm s^{-1} in the helium convection zone of a 60400L1 model with $T_e \simeq 22{,}000$ K. These values are small enough that turbulent pressure remains insignificant in these models. Finally, note that the convective velocity surface of Figure 23*a* also shows the presence of a subphotospheric helium convection zone below the H/He transition zone and the existence of a very weak carbon convection zone below the He/C buffer zone. This has already been noted in our previous description of the radiative luminosity profiles.

Other variables that are of importance in the study of pulsating white dwarfs are the opacity derivatives. In this context, we first show in Figures 24*a* and 24*b* the opacity surfaces themselves. These figures are meant to complement the two-dimensional representations of Figures 18*a* and 18*b*. They give, from a qualitative point of view, a better sense of the behavior of the opacity in evolving white dwarfs. We note in particular that our opacity surfaces are quite smooth, indicating that our interpolation scheme in opacity tables is quite acceptable. It is, of course, more difficult to obtain such smooth surfaces for the opacity derivatives. For example, we have pointed out in § II*d* that the evolution code uses a simple linear technique (a 2-point forward-difference scheme) to evaluate the opacity derivatives. This is perfectly acceptable from the point of view of model convergence (since the opacity derivatives do not affect the structure), but a recomputation of the opacity derivatives with a higher order numerical scheme becomes highly desirable for nonadiabatic pulsation studies. In Figures 25*a* and 25*b* we contrast the opacity derivative surface $(\partial \log \kappa/\partial \log \rho)_T$ for the case in which the data come directly from the evolution code (60510L1 sequence) and the case in which the derivatives have been recomputed within the interpolation code (60400L1 sequence). Figure 25*a* clearly shows a noise pattern (associated with the linear differentiation scheme), which is largely removed in the much smoother surface obtained in Figure 25*b*. Our usual procedure of recomputing the opacity derivatives within the interpolation code is thus clearly worthwhile. It is the increase with increasing depth of the opacity derivative at the base of the convection zone that is of particular importance for pulsation studies. The depression of the opacity derivative in the convection zone is remarkably conspicuous in the DB models (Fig. 25*b*). We note also that the opacity derivative becomes quite small in the core region, where degenerate electron conductivity dominates. The falloff of the opacity derivative at large depths clearly migrates toward shallower regions with decreasing effective temperature (this is particularly obvious in Fig. 25*a*, which is viewed at an angle appropriate for emphasizing this feature). This migration corresponds, of course, to the migration of the degenerate core boundary. A last comment about the $(\partial \log \kappa/\partial \log \rho)_T$ surfaces is the existence of a small numerical glitch in the very

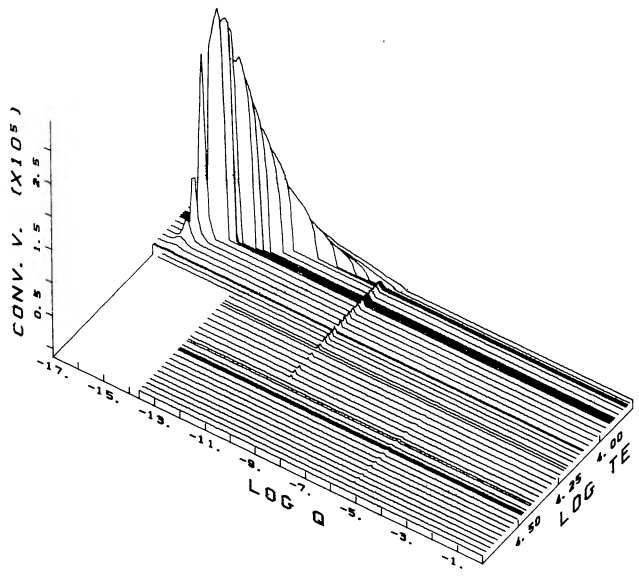

FIG. 23*a*

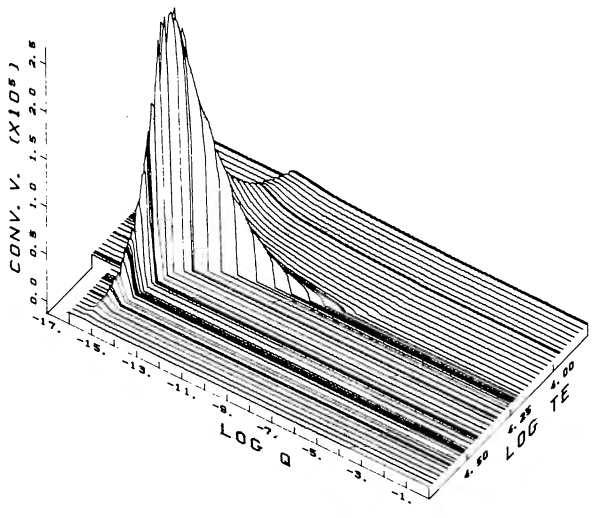

FIG. 23*b*

FIG. 23.—(*a*) Same as Fig. 19*a*, but for the convective velocity. (*b*) Same as Fig. 19*b*, but for the convective velocity.

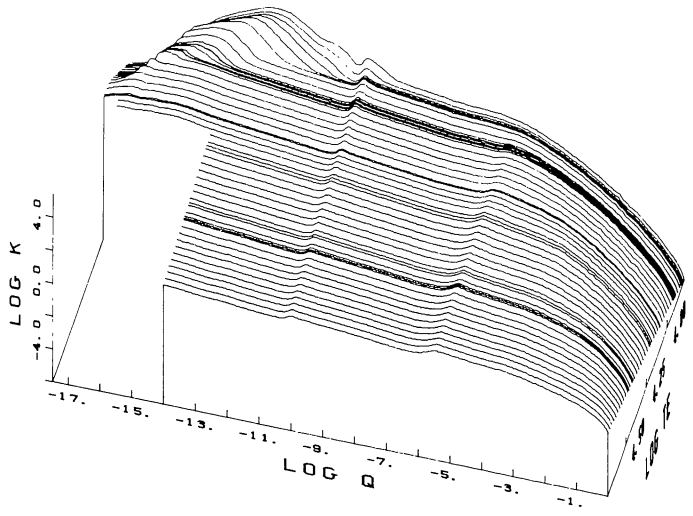

FIG. 24*a*

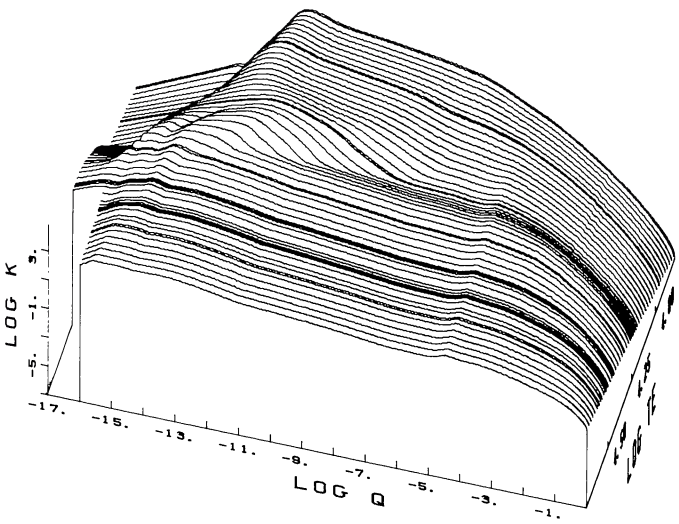

FIG. 24*b*

FIG. 24.—(*a*) Same as Fig. 19*a*, but for the opacity. (*b*) Same as Fig. 19*b*, but for the opacity.

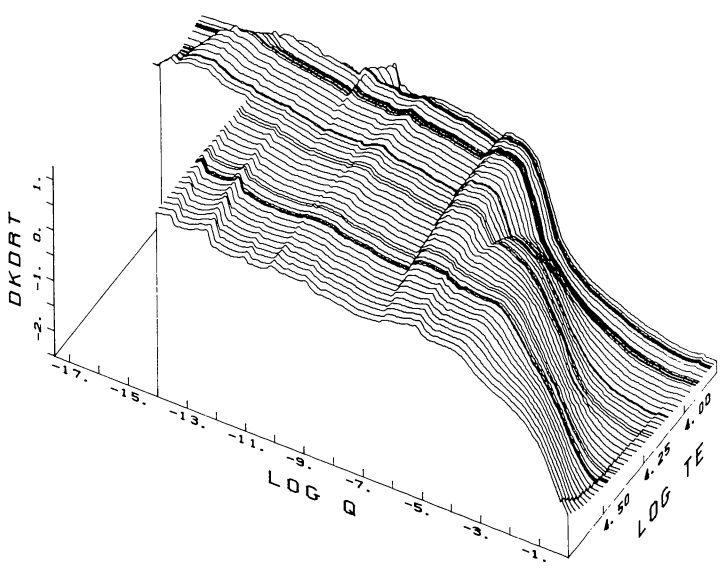

FIG. 25*a*

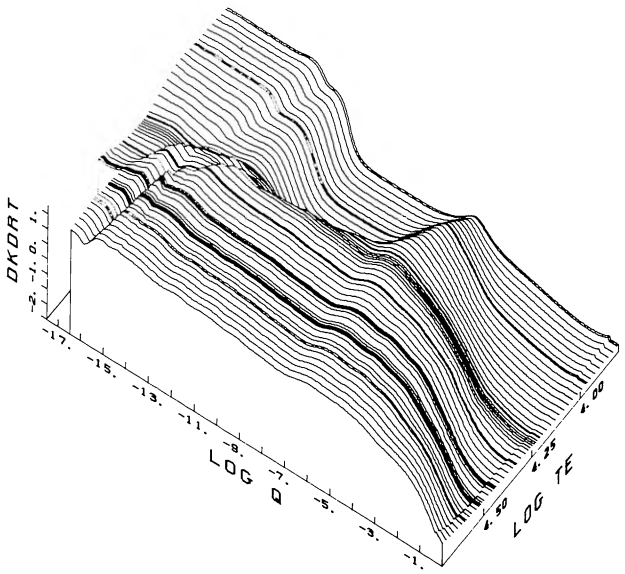

FIG. 25*b*

FIG. 25.—(*a*) Same as Fig. 19*a*, but for the opacity derivative $(\partial \log \kappa/\partial \log \rho)_T$. (*b*) Same as Fig. 19*b*, but for the opacity derivative $(\partial \log \kappa/\partial \log \rho)_T$.

deep carbon core ($\log q \simeq -0.3$), as can be observed in both figures. This small defect has no influence on the structure, evolution, or pulsation properties of our models.

Figures 26*a* and 26*b* show the other opacity derivative surface, $(\partial \log \kappa/\partial \log T)_\rho$. Again, there is a noise pattern in the 60510L1 models (Fig. 26*a*) due to the use of the linear differentiation scheme. The linear technique also exaggerates the structures associated with the composition transition zones. By contrast, the opacity derivative surface for the DB models (Fig. 26*b*) is relatively smooth; the complex structure in the outer regions is real and is caused by partial ionization.

Despite the apparent complexity of the opacity derivative surfaces, we can still identify a number of regimes. For example, in the envelopes of the hotter models (except for the outermost layers of the DB models, where partial ionization is important), free-free transitions dominate and we can expect that $(\partial \log \kappa/\partial \log T)_\rho \simeq -3.5$ and $(\partial \log \kappa/\partial \log \rho)_T \simeq 1$ according to Kramers's law. A quick inspection of Figures 25*a*, 25*b*, 26*a*, and 26*b* reveals that this is roughly correct. (Note that a value of 14.4 should be subtracted from the values labeling the vertical axis in Fig. 26*b*.) In the deep core, a switch to a very different regime is observed because of the

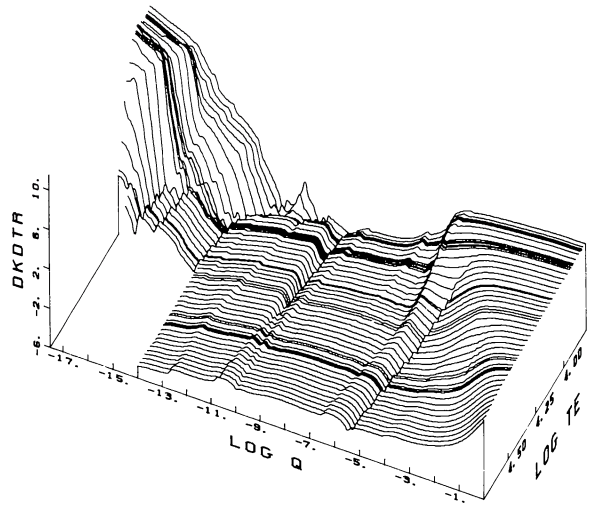

FIG. 26*a*

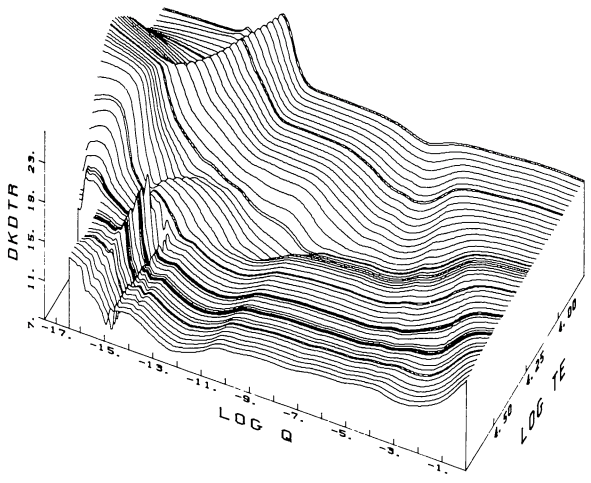

FIG. 26*b*

FIG. 26.—(*a*) Same as Fig. 19*a*, but for the opacity derivative $(\partial \log \kappa / \partial \log T)_\rho$. (*b*) Same as Fig. 19*b*, but for the opacity derivative $(\partial \log \kappa / \partial \log T)_\rho$. Note that a value of 14.4 should be subtracted from the values labeling the vertical axis.

dominance of the conductive opacity of degenerate electrons. A crude fit to the data of Hubbard and Lampe (1969) in the nonrelativistic domain gives $\kappa \propto \rho^{-2} T^{2.4}$ (Fontaine 1973). Thus, we can expect that $(\partial \log \kappa / \partial \log T)_\rho \simeq 2.4$ and $(\partial \log \kappa / \partial \log \rho)_T \simeq -2$ in this regime. Again, this is very roughly what we observe in the figures. Finally, even cruder fits to opacity tables at the *top* of partial ionization zones suggest that $\kappa \propto \rho^a T^b$, where the ranges of a and b are 0.3–0.5 and 10.0–10.3, respectively (Fontaine 1973). Thus, we can expect rather large values of the temperature derivative and relatively small values of the density derivative at the top of partial ionization zones. This is in rough agreement with the figures. Note that the exact opacity derivative profiles (particularly that of the temperature derivative) enter in a critical way into the computations of nonadiabatic pulsation properties.

Further quantities of interest are associated with the equation of state. For instance, Figures 27*a* and 27*b* show the evolution of the pressure derivative profiles $\chi_\rho = (\partial \log P / \partial \log \rho)_T$. The general behavior for a given model is an increase from a value of about unity (which is appropriate for an ionized or neutral ideal gas in which radiation is negligible) to a somewhat larger value (which would be equal to 5/3 for an ideal, nonrelativistic Fermi-Dirac gas) with

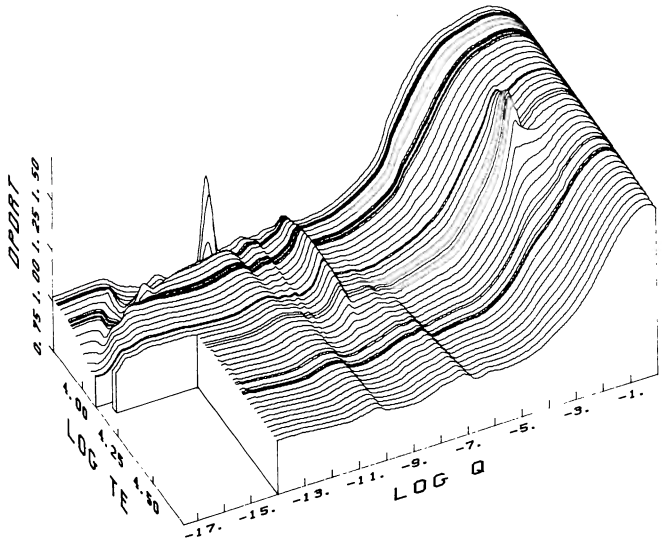

FIG. 27*a*

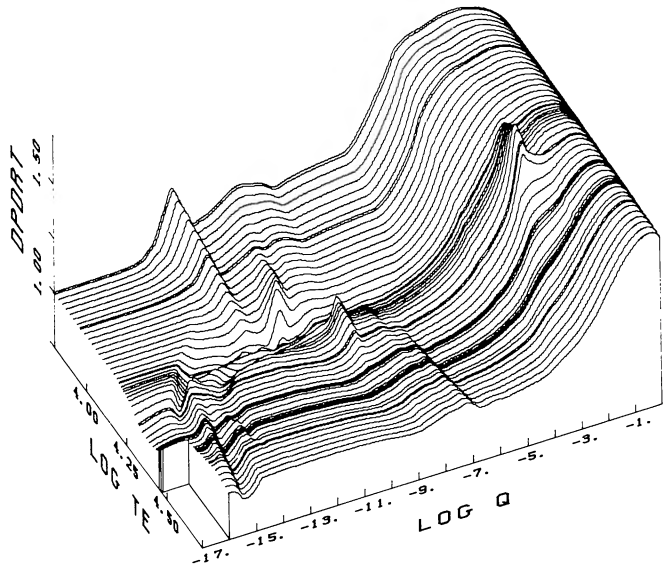

FIG. 27*b*

FIG. 27.—(*a*) Same as Fig. 19*a*, but for the pressure derivative χ_ρ. (*b*) Same as Fig. 19*b*, but for the pressure derivative χ_ρ.

increasing depth. There are several departures from this general behavior. First, in the regions of partial ionization, χ_ρ initially assumes (i.e., at higher effective temperatures) values smaller than unity. This phase corresponds to the dominance of thermal ionization in an ideal gas. With cooling, nonideal effects become important, pressure ionization takes over, and this causes the pressure derivative to become larger than unity. The transition from thermal to pressure ionization is particularly obvious in the DB models (Fig. 27*b*). The same transition occurs in the DA models, but at lower effective temperatures (note the three peaks in the ionization zones of the three coolest models).

With the exception of a weak bump corresponding to the H/He transition zone in the 60510L1 sequence, other structures of the χ_ρ surface in the envelope must be associated with nonideal effects which are included in the complex atomic model used by Fontaine, Graboske, and Van Horn (1977). In the deeper regions ($\log q \simeq -2$), the transition from the tabular envelope equation of state and the high-density, high-temperature analytic fits (the third part of the equation of state) causes a small unphysical bump in models with intermediate effective temperatures. Again, as in the case of the adiabatic temperature gradient, this bump is not expected to play a significant role. Finally, in the central regions themselves, χ_ρ shows a reversal which is stronger in cooler models. This is due simply to the onset of relativistic effects on the degenerate electrons. These effects have a tendency to push the value of χ_ρ from 5/3 (nonrelativistic limit) to 4/3 (ultrarelativistic limit). The effects are larger in cooler models because the central densities are also larger.

Figures 28*a* and 28*b* illustrate the behavior of the other pressure derivative, $\chi_T = (\partial \log P/\partial \log T)_\rho$. As compared with an ionized (or neutral) ideal gas (with no radiation) for which $\chi_T = 1$, the pressure depends even more strongly on the temperature in regions of partial ionization. This dependence produces the sharp peaks which are prominent in the figures. Note how these ridges are directly associated with the valleys of partial ionization which are found in the adiabatic temperature gradient surfaces (compare with Figs. 19*a* and 19*b*). We can also remark that the amplitudes of the ionization peaks decrease with decreasing effective temperature, and this is due to the gradual transition from thermal to pressure ionization just described. The other main feature of the χ_T surfaces is the gradual decrease of the pressure derivative to very small values in the deep core with increasing depth. This is caused by the fact that the pressure becomes dominated by the degenerate electron contribution, and, consequently, its temperature dependence almost vanishes. The rapid falloff of χ_T as a function of depth also maps the migration of the degenerate core boundary toward the surface with decreasing effective temperature.

The last equation-of-state variable used in pulsation calculations is the specific heat (per gram) at constant volume, C_V. (Other quantities, such as, for example, C_P entering into the convection equations, can be computed directly from the variables listed in Table 1.) The evolution of the specific heat profiles in cooling white dwarfs is illustrated in Figures 29*a* and 29*b*. Ionization peaks very similar to those discussed for the χ_T surfaces reflect the well-known capacity of partially ionized matter to store up energy. Below the partial ionization zone, and extending over a substantial fraction of the envelope, we find regions where $C_V \simeq$ constant. This is particularly evident in the hotter models of the 60510L1 sequence (Fig. 29*a*). In these models, there are two plateau regions above the He/C transition zone. In these regions, the gas is essentially completely ionized and is almost perfect. This implies that the specific heat becomes a direct measure of the number of free particles and is inversely proportional to the mean molecular weight. The sharp decrease of C_V across the H/He transition region corresponds to the significant decrease of the number

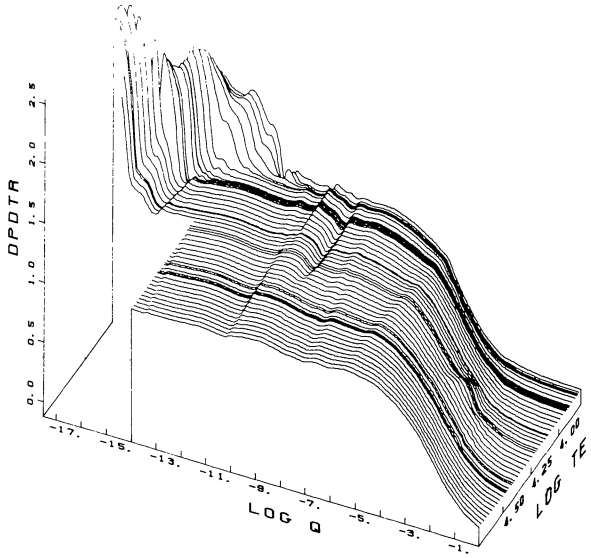

FIG. 28*a*

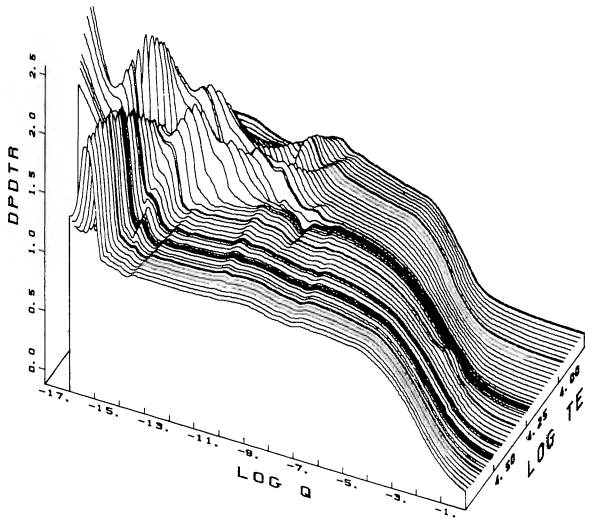

FIG. 28*b*

FIG. 28.—(*a*) Same as Fig. 19*a*, but for the pressure derivative χ_T. (*b*) Same as Fig. 19*b*, but for the pressure derivative χ_T.

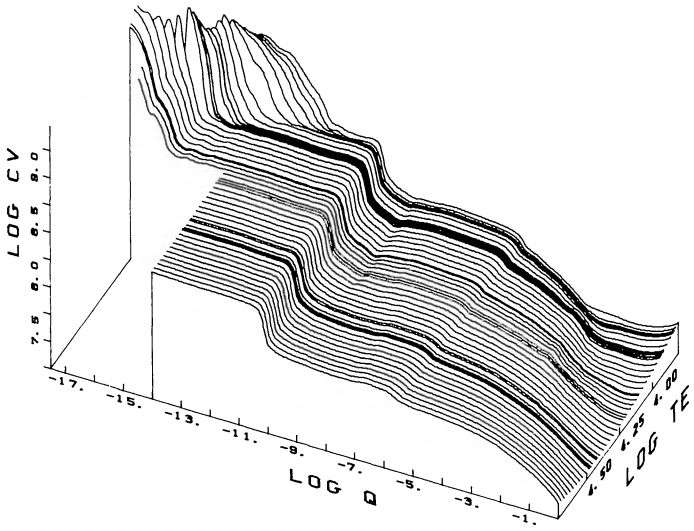

FIG. 29*a*

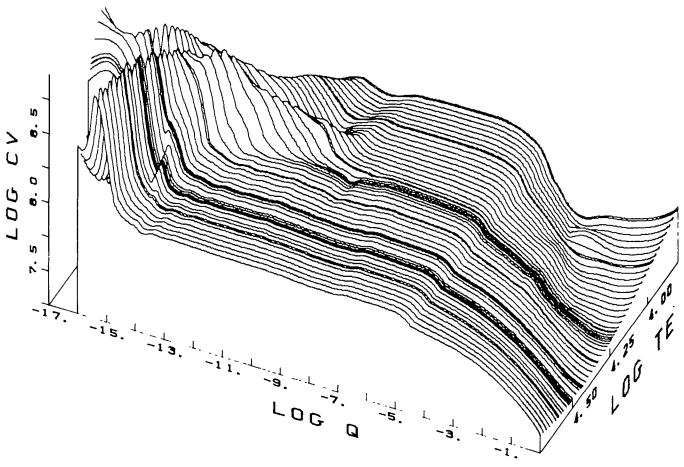

FIG. 29*b*

FIG. 29.—(*a*) Same as Fig. 19*a*, but for the specific heat at constant volume. (*b*) Same as Fig. 19*b*, but for the specific heat at constant volume.

of free particles in going from ionized hydrogen to ionized helium at constant density. In the perfect gas limit, we have $C_V(\text{H II}) = 3N_0k \simeq 10^{8.4}$ and $C_V(\text{He III}) = (9/8)N_0k \simeq 10^{8.0}$, which are roughly the values that are found in Figure 29*a*. In both Figures 29*a* and 29*b* there is a further decrease of the specific heat associated with the He/C buffer zone. This is again related to a decrease in the number of free particles, but the effect is much less pronounced than in the H/He transition zone because the difference between the mean molecular weight of helium and that of carbon is comparatively small.

A further interesting feature of the specific heat surfaces is the substantial decrease of C_V with increasing depth in the deep envelope and core regions. Here the increasing degeneracy of free electrons makes them less capable of storing energy, and their contribution to the specific heat becomes less important and, ultimately, negligible. In the core region of the cooler models, only ions can contribute to C_V. We note that such ions can interact strongly, forming a liquid and, at very low effective temperatures, forming a solid. We have already mentioned that our treatment of the equation-of-state properties of the ionic system is rather crude. Nevertheless, the Coulombic term which we have used is responsible for the departure of C_V from the behavior of an ideal ionic gas. In particular, this (liquid) term increases the specific heat of the ionic system, and the effect naturally increases with cooling. This explains the increase of the central values of C_V with decreasing T_e in the cooler models of Figures 29*a* and 29*b*.

Our discussion of the evolution of the key variables used in pulsation studies of white dwarfs would not be complete without including the helium distribution, the Ledoux term, and the Brunt-Väisälä frequency (see Table 1). Thus, Figures 30*a* and 30*b* show how the helium distribution changes during the evolution of our two typical sequences. We have chosen the two-dimensional representation because there are interesting features which would not have been so obvious in the three-dimensional representation. Because the composition profile does not change very much during the interval of time covered by our calculations, the curves overlap somewhat in our figures. Nevertheless, we have isolated the following characteristics. First, from Figure 30*a*, we find that the composition profile in the H/He transition zone has practically not changed. As indicated in the previous section, slight changes in the equilibrium abundance profile come mainly from slight changes in the average charges Z_1 and Z_2 due to cooling. In our particular example of a hydrogen/helium transition zone located around $\log q \simeq -10$, hydrogen is completely ionized there, and helium is not quite completely ionized *but* its ionization state does not change significantly. Hence, the equilibrium conditions are nearly unchanged. By contrast, carbon undergoes some nonnegligible recombination (helium remains totally ionized) as a function of cooling in the He/C transition zone of our models ($\log q \simeq -5$). This produces a somewhat narrower transition zone. The helium mass fraction in the He/C transition zone of the coolest (hottest) model is therefore given by the curve which defines the right (left) boundary of the band shown in Figure 30*a*. Note that these two limiting curves cross each other (as they should if the total mass of helium is to be the same) around $\log q \simeq -4.3$.

It is easy to understand why the He/C transition zone becomes narrower if the charge of carbon Z_2 decreases (for a constant value of the charge of helium Z_1). Indeed, equations (27) and (28) indicate that both α_1 and α_2 would increase in absolute value, implying a decrease of the scale height (see eqs. [30] and [31]). The narrowing of the He/C transition zone is less important in our DB models (Fig. 30*b*) even though the range of effective temperature covered is larger. This is because the He/C transition zone is located deeper ($\log q \simeq -4$), and carbon remains more nearly ionized at this larger depth. Note also that the H/He transition zone is narrower than the He/C transition zone in our DA models (Fig. 30*a*). This is again related to the combination of atomic

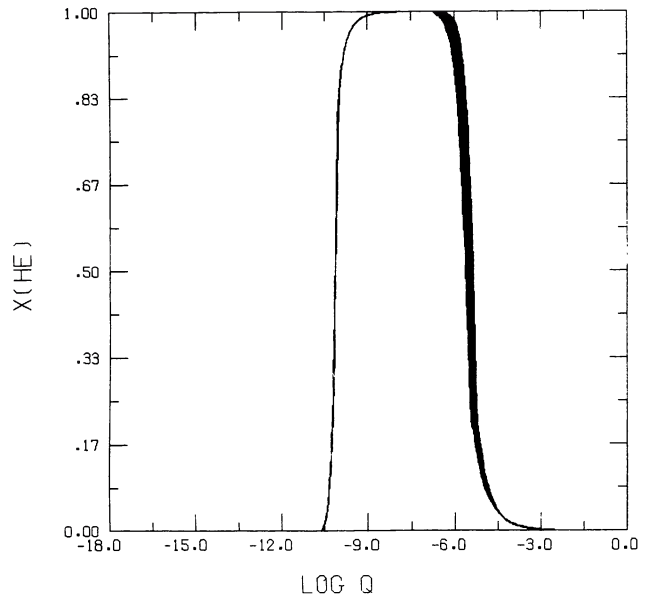

FIG. 30*a*

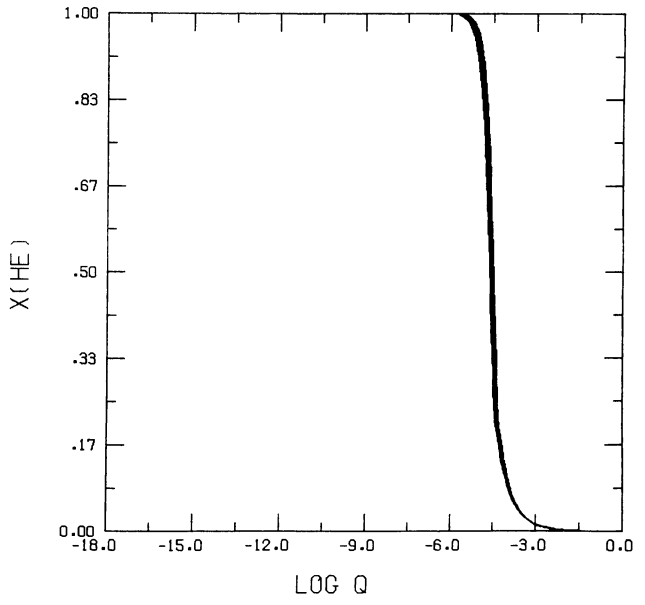

FIG. 30*b*

FIG. 30.—(*a*) Same as Fig. 14*a*, but for the helium mass fraction profiles. (*b*) Same as Fig. 14*b*, but for the helium mass fraction profiles.

weights and charges that enter the computations of the quantities α_1 and α_2.

Figure 31 gives an idea of the behavior of the Ledoux term B which enters into the computation of the Brunt-Väisälä frequency and which contains the contribution of the composition transition zones. To avoid confusion, and in the spirit of an illustrative example, we have simply selected two models belonging to the 60510L1 sequence: model 184 ($T_e = 17{,}989$ K) and model 260 ($T_e = 9344$ K). Other models give very similar qualitative results. Keeping in mind that B must be compared to $\nabla_{ad} \simeq 0.4$ (eq. [34]), it becomes clear that B can contribute only locally to the Brunt-Väisälä frequency, i.e., in the composition transition zones themselves. Note that the general shape of the B curve corresponds to a rather steep change of the composition in the upper half of a transition zone (either H/He or He/C) followed by a slower change of composition in the lower half of the zone. This is directly related to the composition gradients which are specified by the values of α_1 and α_2. Note also that Figure 31 shows practically no differences between the B-values of our two different models in the H/He transition zone. This, of course, corresponds to the fact that the composition profile in that transition zone has practically not changed, as noted just above. By contrast, because our cooler model has a narrower He/C transition zone, the composition gradient is larger there, and this is translated into larger values of B in that transition zone.

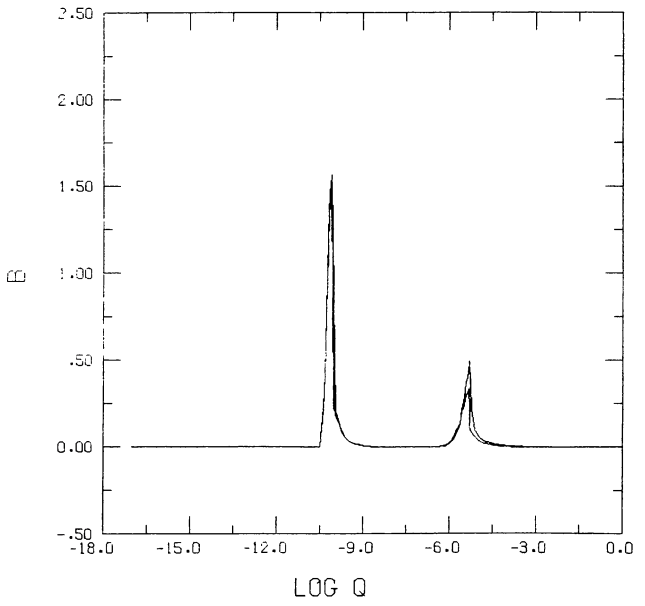

FIG. 31.—Profiles of the Ledoux term B for two typical DA models belonging to the 60510L1 sequence.

Figure 32 shows the profiles of the square of the Brunt-Väisälä frequency for the same two DA models. The dotted line corresponds to the hotter one. The overall behavior of N^2 in that model is a general decrease with increasing depth, eventually reaching very small values in the deep core (this is quite characteristic of degenerate configurations in which low-order g-modes cannot propagate because N^2 is too small). Of course, we have excluded the central value $N^2 = 0$ in our plot. Except for the existence of a hydrogen convection zone (in which N^2 becomes negative) in the outer layers of the cooler model, the behavior of N^2 is only moderately affected by cooling. We note, however, that the Brunt-Väisälä frequency assumes lower values in the deep core of the cooler model, which corresponds to the overall increase of degeneracy in its interior. The existence of an outer convection zone in the cooler model is an important difference insofar as mode

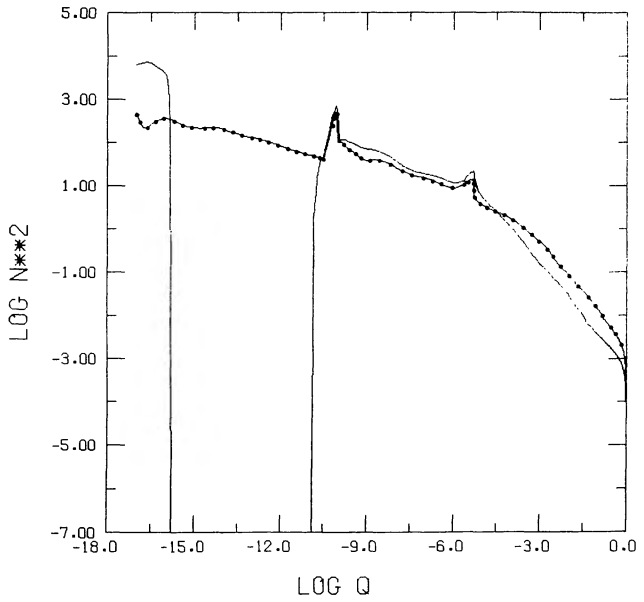

FIG. 32.—Same as Fig. 31, but for the square of the Brunt-Väisälä frequency.

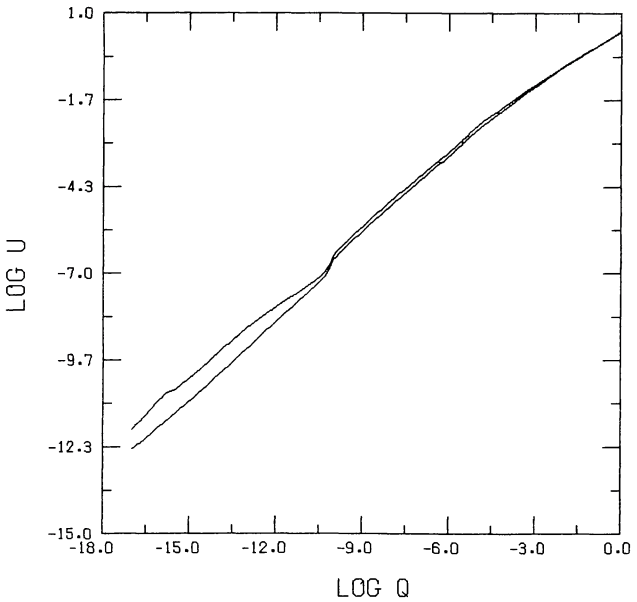

FIG. 33.—Same as Fig. 31, but for the quantity U

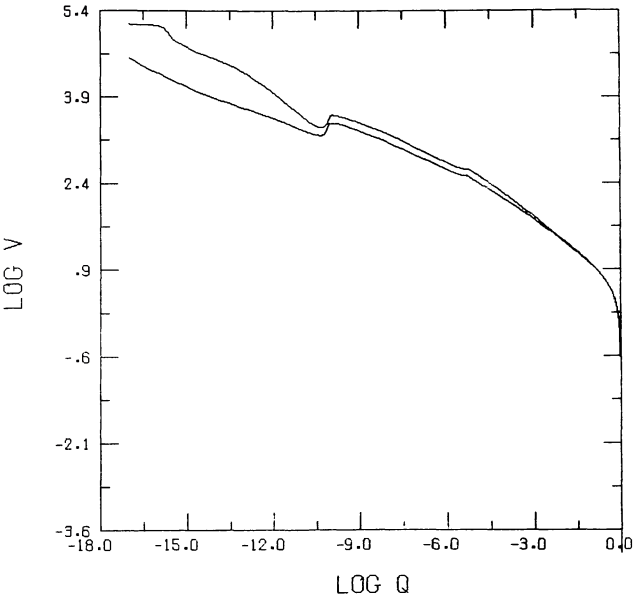

FIG. 34.—Same as Fig. 31, but for the quantity V

propagation and mode selection can be affected in this region. Finally, we remark that the contribution of the Ledoux term to the N^2 profile corresponds to small spikes in the composition transition zones. The locations as well as the exact shapes of these spikes may determine in large part the mode selection characteristics of layered white dwarf models. Attention and care in the evaluation of B are therefore critical for a discussion of mode trapping in white dwarfs.

For the sake of completeness, the next two figures illustrate the typical behaviors of two additional variables which, along with N^2, enter directly into the *adiabatic* pulsation equations as formulated by Saio and Cox (1980). These quantities can be formed by a combination of some of the variables listed in Table 1. It is nevertheless instructive to discuss briefly their dependence on cooling. The first variable is U $[\equiv 4\pi r^3\rho/M(r)]$, a quantity related to the mechanical structure and, as such, not expected to be significantly affected by cooling. A known boundary condition of the adiabatic pulsation equations is that $U \to 3$ when $r \to 0$. Figure 33 shows the U profiles for our two reference DA models used previously. There is a monotonic increase with increasing depth. As expected, there are little differences between the two models, especially in the core region; at the center itself, $U = 3$. There is also a monotonic change in the sense that the cooler model assumes larger values of U at a given mass shell. If $\langle\rho\rangle = 3M(r)/(4\pi r^3)$ is defined as the average density inside a sphere of radius r, then U can be written as $U = 3\rho/\langle\rho\rangle$, implying $U(r = 0) = 3$ and $dU/dr < 0$. We can thus readily understand Figure 33 in terms of Figure 15*a*.

A very similar situation is found for the quantity V $[\equiv G\rho M(r)/(rP)]$, which is illustrated in Figure 34 and which is another variable related to the mechanical structure. This time there is a general decrease of the variable with increasing depth. Again, there are only very small differences in the values of V between the two models in the core region because cooling no longer affects the electron degenerate mechanical structure of this region in these rather advanced phases of the evolution of a white dwarf. The central boundary value $V(r = 0) = 0$ is excluded from the plots. Also, there is a monotonic behavior in the sense that V assumes larger values in cooler objects. In contrast to the core region, the differences are not negligible in the outer layers of the models. The hydrogen convection zone of the cooler model as well as the composition transition zones produce some obvious structure in the V profiles. Here V can be rewritten as $V = r/H_P$, so that Figure 34 is intimately related to Figure 17*a*.

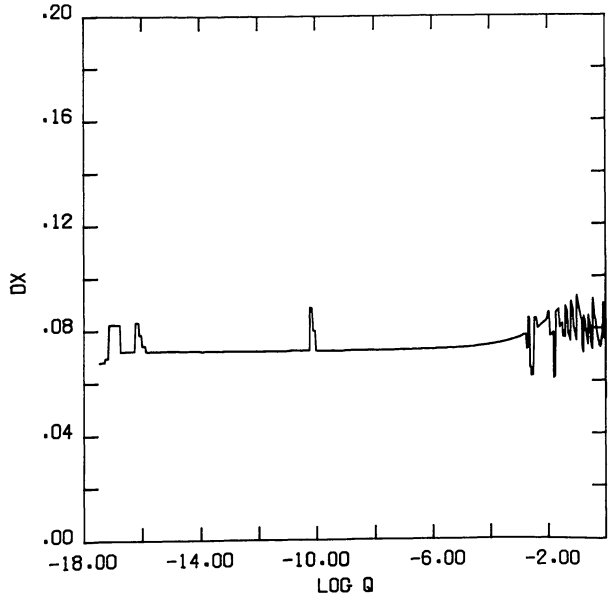

FIG. 35.—Shell spacing distribution in model 196 ($T_e = 9999$ K) belonging to the 60210L1 sequence.

Finally, to complete this subsection, we show in Figure 35 a typical distribution of shell spacings in one of our models in terms of the variable x [$= \ln(r/P)$] used in pulsation codes. The diagram plots the shell spacing Δx between two adjacent shells for model 196 ($T_e = 9999$ K) belonging to the 60210L1 sequence (a typical model) as a function of depth. As pointed out previously (§ II*d*), the pulsation codes do *not* require Δx to be strictly uniform. Our interpolation scheme, however, aims at a distribution which is as uniform as possible. In the envelope regions, the distribution is indeed largely uniform because of the direct scaling $\xi \propto x$ discussed previously. Two exceptions stand out: there is structure in the H/He transition zone and near the surface. In both cases the structure is a consequence of the necessity of keeping track of changing conditions in critical regions. In the deep core, x does not scale on ξ, and the resulting distribution is simply a consequence of our particular recipe for selecting shells out of a distribution which shows bunching (see § II*d*). The typical scatter is less than 30% of the mean value of Δx.

c) *Asymptotic Period Spacings*

A potentially very powerful seismological tool for degenerate stars is the comparison of observed period spacings with the uniform spacings predicted by asymptotic pulsation theory. Kawaler (1986, 1987*a*, *b*, *c*) was the first to introduce this technique to the field and, in a remarkable example of the scientific process, was able to derive a very accurate value for the mass of PG 1159−035 ($M = 0.60 \pm 0.02\ M_\odot$), the prototype of the pulsating pre-white dwarfs known as DOV stars. This was possible because Kawaler first recognized that period differences in the complex Fourier spectrum of the light curve of PG 1159−035 could be understood in terms of integer multiples of constant period spacings. At the same time, he demonstrated that such period spacings would be most sensitive to the mass for models appropriate for DOV stars, and that the effects of other parameters, such as the luminosity and the superficial composition, are relatively small. The technique introduced by Kawaler is based on the asymptotic pulsation theory developed by Tassoul (1980). This theory shows that, for chemically homogeneous and radiative stars, in the limit of very large values of k (long periods), the g-mode periods for a given value of l and consecutive k are separated by a constant period interval $\Delta\Pi_l$. This interval can be expressed in terms of an integral which depends only on the structure of a model:

$$\Delta\Pi_l = \frac{\Pi_0}{[l(l+1)]^{1/2}}, \tag{43}$$

with

$$\Pi_0 = 2\pi^2 \left(\int_0^R \frac{N}{r}\, dr \right)^{-1}, \tag{44}$$

where N is the Brunt-Väisälä frequency and r is the radial coordinate. Here l refers to the usual index of the spherical harmonics used in linear pulsation theory to describe the angular geometry, and k is the order of the mode, i.e., the number of nodes in the radial part of the eigenfunction of the mode. If a white dwarf pulsates in high-order modes with the same value of l but different values of k, its Fourier spectrum should show period differences that are integer multiples of the minimum period spacing $\Delta\Pi_l$, in a first approximation. Because the characteristic period spacing Π_0 depends only on the structural properties of the star, one can hope to use its observed period spacings to infer some of these structural properties. Clearly, before this tool can be applied to pulsating white dwarfs, one must investigate the effects of various model parameters on Π_0. The evolutionary models computed in the present investigation are ideally suited for such a task, and we now turn to a discussion of that problem in this subsection.

A direct application of the asymptotic approach to pulsating white dwarfs is made somewhat uncertain by the fact that these stars are chemically stratified in the outer layers and that the pulsation periods are formed in those layers. For example, the period structure of a typical DA white dwarf is dominated by resonance effects (mode trapping) caused by the presence of composition transition zones. This is particularly true for a model with a low value of q(H). Mode trapping usually gives rise to periods which are *not* equally spaced, even for high-order modes. On the other hand, short of full-fledged pulsation calculations, useful information can still be made available from the asymptotic approach because the *mean period spacing* for high-order modes is very close to the asymptotic value even in the presence of mode trapping (Kawaler 1987*a*). Moreover, the effects of mode trapping are considerably lessened in models with relatively large values of q(H). The usefulness of the asymptotic approach can further be justified by mentioning that the observed periods in several DAV and DBV stars *require* that the pulsation modes be of high order.

We have computed the expected characteristic period spacing Π_0 for a very large fraction of our evolutionary models. In the process, we have ignored the local contributions of the composition transition zones to the Brunt-Väisälä frequency in order to make detailed comparisons with the period structures of Winget (1981) which were computed by neglecting these contributions as well. Specifically, we have not included the term B in our expression for the Brunt-Väisälä frequency (see eq. [34]) used in the integral for Π_0. Extensive tests show that Π_0 is *almost uniformly* decreased by $\sim 10\%$ if B is included, which implies that our discussion of the effects of model parameters is essentially unaffected. In the presence of composition layering and convection zones, we have approximated Π_0 by integrating simply over the radiative regions (where $N^2 \geq 0$) and adding together the contributions from each radiative zone. This procedure turned out to be quite acceptable, since a comparison with the detailed pulsation results of Winget (1981) for DA stars showed a typical agreement of better than 4% between our asymptotic value of Π_0 and the mean value averaged over several pulsation modes for a given model. In practice, we have used the periods of all modes with $k \geq 9$ computed by Winget (1981) to estimate an average value of the period spacing for a mode with a given l. We have also used all the models studied by Winget (1981) in this comparison. We thus feel confident that our values of Π_0 are reliable.

Figure 36 shows the effects of varying the total mass and the convective efficiency of DA models on the characteristic period spacing. In this and the following figures, we have concentrated on the effective temperature range of immediate interest for DAV stars: 13,000 K $\gtrsim T_e \gtrsim$ 9000 K. A pair of curves (a continuous and a dashed one) is associated with each mass which we have considered ($M/M_\odot = 0.4$, 0.6, and 0.8). The continuous curves correspond to evolutionary sequences computed with the ML1 version of the mixing-length theory, and the dashed curves to sequences computed with ML3 convection. The ML3 curves have not been extended to effective temperatures lower than the mixing temperatures. For the models which we have used in this comparison [$\log q(\mathrm{H}) = -10$, $\log q(\mathrm{He}) = -2$], mixing occurs above 9000 K (see Table 2). It is to be noted that Figure 36 illustrates *typical* magnitudes of the effects of changing the total mass and the convective efficiency. The most important effect is clearly related to the total mass of the model; the value of Π_0 is some 50% larger for a 0.4 $M_\odot$ model than for a 0.8 $M_\odot$ model at $T_e \simeq 11{,}000$ K. This is mostly a question of gravity (see eq. [34]), which reduces the Brunt-Väisälä frequency in a less massive model. This overall reduction of N implies an increase of Π_0 as indicated by equation (44). The characteristic period spacing is also sensitive to effective temperature, increasing typically by $\sim 45\%$ with decreasing temperature over the range shown in Figure 36. The effect would, of course, be smaller if we were to restrict the temperature range to the actual observed width of the DAV instability strip. The general increase of Π_0 with cooling depends mostly on the overall decrease of N caused by the behavior of the pressure derivative χ_T. With cooling, the pressure becomes less and less dependent on the temperature and χ_T continuously decreases. The dashed curves in Figure 36 show that the typical

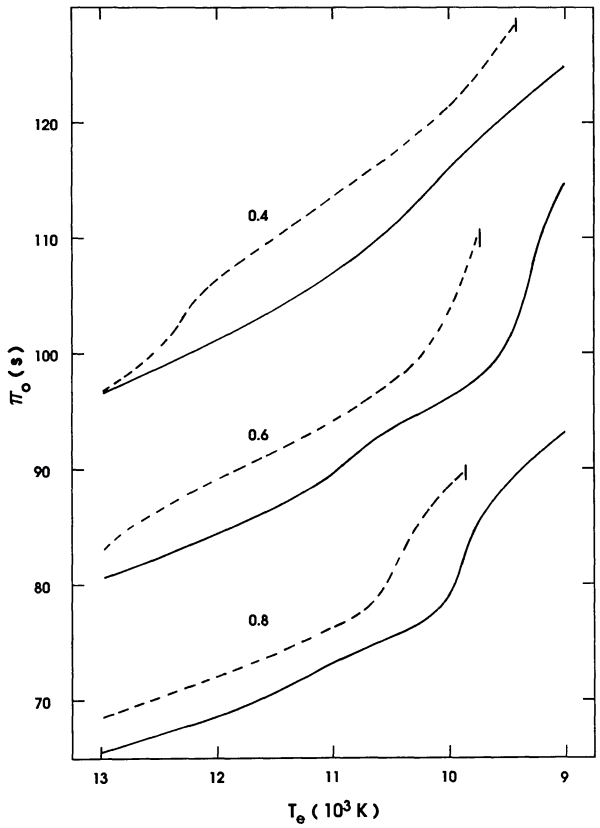

FIG. 36.—Characteristic period spacing vs. effective temperature for evolving DA models near the DAV instability strip. The models have $\log q(\mathrm{H}) = -10$ and $\log q(\mathrm{He}) = -2$. The figure shows the effects of varying the total mass and the convective efficiency. To each labeled mass (in solar units) corresponds a pair of curves: the dashed one refers to models computed with ML3 convection and the continuous one to models computed with ML1 convection.

effect of increasing the convective efficiency from ML1 to ML3 is to increase Π_0 by $\sim 5\%$. Qualitatively, this is easy to understand because ML3 convection zones go deeper than ML1 convection zones for models which have otherwise the same parameters. Thus, the integral $\int (N/r)\, dr$ is obtained over a somewhat smaller (radiative) region and is, consequently, reduced. Figure 36 also illustrates the fact that differences between ML1 and ML3 convection zones occur at lower effective temperatures for the less massive stars.

Another important effect is that produced by varying the mass of the outer hydrogen layer, $q(\mathrm{H})$. Figure 37 shows the relationship between Π_0 and T_e for DA models with $M = 0.6$ $M_\odot$, ML1 convection, $\log q(\mathrm{He}) = -2$, and for a hydrogen layer mass varying in the range $-14 \leq \log q(\mathrm{H}) \leq -4$. The curves, from top to bottom, refer to evolutionary models with $\log q(\mathrm{H}) = -14$, -12, -10, -8, -6, and -4, respectively. Again, the curves have not been extended to effective temperatures lower than mixing temperatures. Coupled with the general increase of Π_0 with cooling, we find that models with the thinner hydrogen layers are those with the larger asymptotic period spacings. At a typical effective temperature of $T_e = 11{,}000$ K, Π_0 is larger by $\sim 30\%$ for a model with

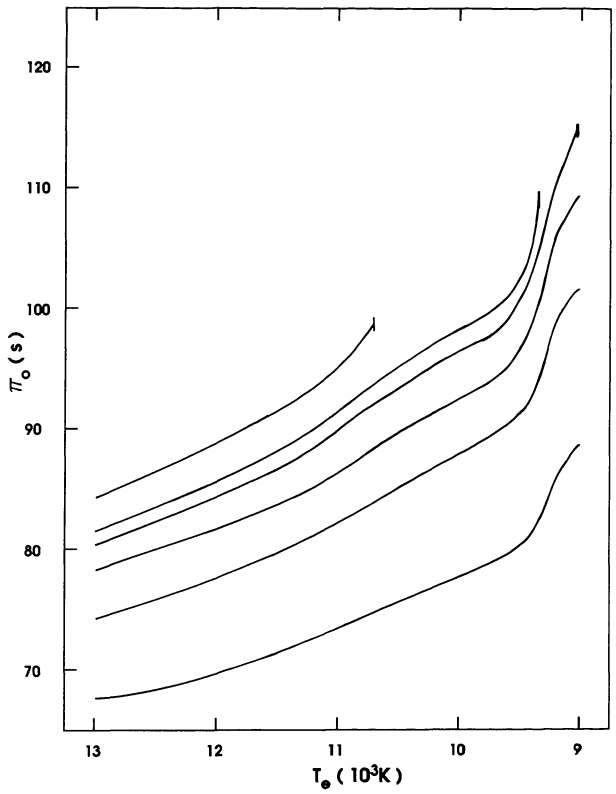

FIG. 37.—Similar to Fig. 36, but illustrating the effects of varying the mass of the outer hydrogen layer. The curves refer to 0.6 $M_\odot$ DA models computed with ML1 convection. The curves correspond to models with log q(H) = −14, −12, −10, −8, −6, and −4, from top to bottom, respectively.

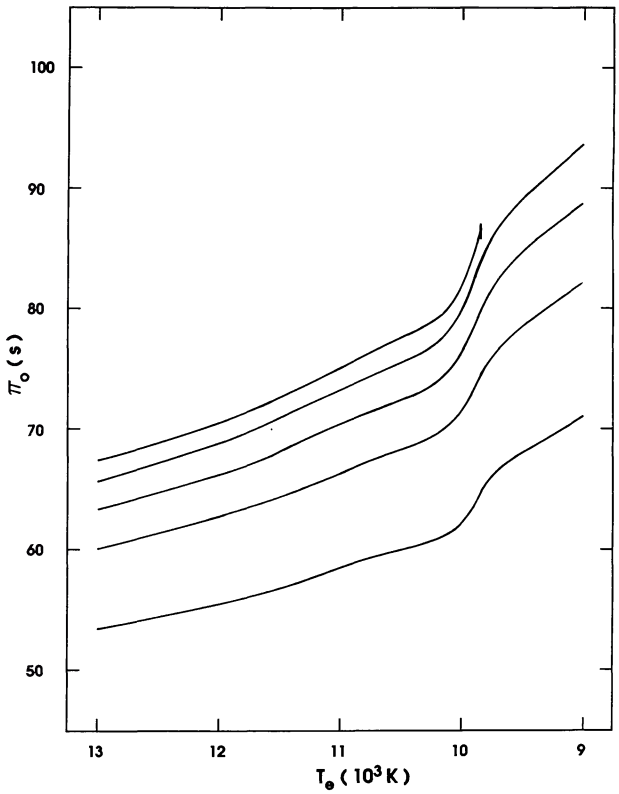

FIG. 38.—Similar to Fig. 37, but for 0.8 $M_\odot$ models. The curves correspond to models with log q(H) = −12, −10, −8, −6, −4, from top to bottom, respectively.

log q(H) = −14 than for a model with log q(H) = −4. The absolute sensitivity of Π_0 to q(H) is roughly the same (although the *relative* sensitivity is somewhat increased) if the total mass of the model is increased. This is shown in Figure 38, which is qualitatively very similar to Figure 37; data have been computed and are illustrated for 0.8 $M_\odot$ ML1 models with log q(He) = −2 and with log q(H) = −12, −10, −8, −6, and −4, from top to bottom, respectively. The dependence of Π_0 on q(H) is only weakly affected by changes in the q(He) value of the helium outer layer. This is illustrated by Figure 39, which shows again the relationship between Π_0 and T_e for models with different values of q(H). The family of continuous curves corresponds to 0.6 $M_\odot$ ML1 models with log q(He) = −4 and log q(H) = −12, −10, −8, and −6, from top to bottom, respectively. The dashed curves correspond to similar models with M = 0.6 $M_\odot$, ML1 convection, but with log q(He) = −6 and log q(H) = −12, −10, and −8, from top to bottom, respectively. A comparison of Figure 39 with Figure 37 shows indeed that the effects of varying q(He) are relatively small, and that the dominant effect is by far the sensitivity of Π_0 to q(H).

The lack of discrimination of the asymptotic period spacing with respect to the mass of the helium layer in DA models is perhaps better illustrated by plotting the same data but in a different way. Figures 40*a*, 40*b*, and 40*c* use the data for evolutionary models with M = 0.6 $M_\odot$ and ML1 convection, but this time q(H) is kept constant in a given figure and q(He) is varied. Figure 40*a* refers to models with log q(H) = −8 and log q(He) = −2 (*continuous curve*), −4 (*dashed curve*), and −6 (*dotted curve*); Figure 40*b* refers to models with log q(H) = −10 and log q(He) = −2 (*lower continuous curve*), −4 (*upper continuous curve*), −6 (*dashed curve*), and −8 (*dotted curve*); Figure 40*c* refers to models with log q(H) = −12 and log q(He) = −2 (*lower continuous curve*), −4 (*upper continuous curve*), −6 (*dashed curve*), and −10 (*dotted curve*). The figures show that the effects of varying q(He) for constant q(H) on Π_0 are not monotonic, since the curves cross each other. Mostly, however, and this is the important conclusion, the figures show that these effects are quite small, typically of order 1% for all the sequences (except for 61012L1, where the deviation is about 3 times larger) around T_e = 11,000 K. The basic reason why Π_0 is sensitive to q(H) and not to q(He) is that the combination of thermodynamic variables entering the computation of N (see eq. [34]) is sensitive to a change of material with a different electronic mean molecular weight (μ_e = 1 for ionized H and μ_e = 2 for ionized He) and not to a change of material with the same value of μ_e (2 for both ionized He and C). Thus, replacing helium by carbon by decreasing q(He), for example, does not very much affect the local Brunt-Väisälä frequency. The effect is markedly different if hydrogen is replaced by helium when q(H) is decreased; in that case, the Brunt-Väisälä frequency is significantly decreased, which leads to larger values of Π_0.

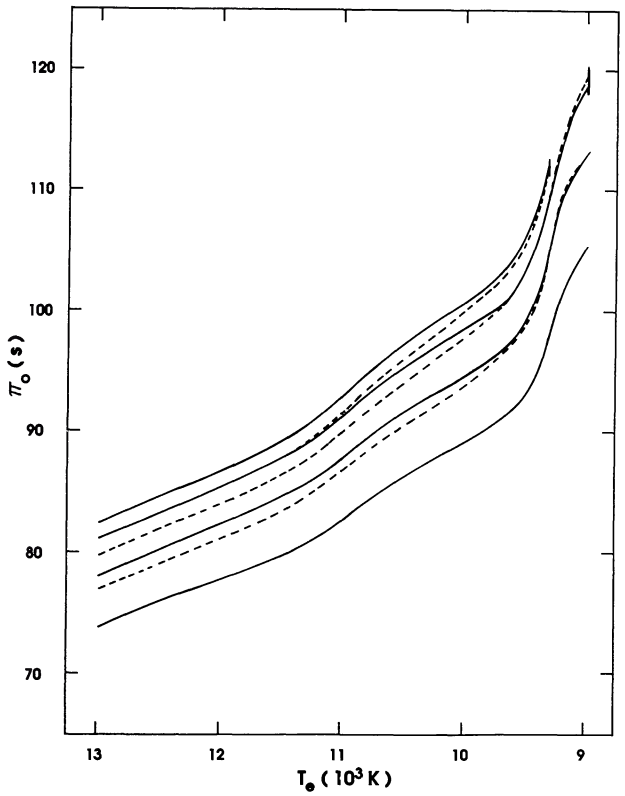

FIG. 39.—Similar to Fig. 36, but for 0.6 $M_\odot$ DA models computed with ML1 convection and variable values of the masses of the outer hydrogen and helium layers. The continuous curves refer to models with log q(He) = −4 and log q(H) = −12, −10, −8, −6, from top to bottom, respectively. The dashed curves refer to models with log q(He) = −6 and log q(H) = −12, −10, and −8, from top to bottom, respectively.

This latter behavior is explicitly demonstrated in Figure 41, which shows the running integral $\int(N/r)\,dr$ as a function of the mass fraction log q from the center to the base of the superficial hydrogen convection zone of three models with similar effective temperatures. The upper dashed curve refers to model 244 (T_e = 10,821 K) belonging to the 80204C1 sequence, the lower dashed curve to model 256 (T_e = 10,855 K) belonging to the 80206C1 sequence, and the continuous curve to model 224 (T_e = 11,047 K) belonging to the 80208L1 sequence. The effective temperature difference between the first two models is so small that the figure cannot reveal a difference in the running integral for log $q \gtrsim -4$ (the two dashed curves have merged). Above this level, however, the running integrals for the two models clearly diverge because the Brunt-Väisälä frequency is larger in a hydrogen environment than in a helium environment. The transition into a H-rich medium is clearly observed in Figure 41; the effects on the running integral are larger the deeper the H/He transition zone. Thus, the model with the thicker hydrogen layer [log q(H) = −4] shows a larger running integral and, eventually, a smaller value of Π_0. The model with log q(H) = −8 (*continuous curve*) also shows an obvious increase of its running integral for log $q \lesssim -8$; the effect, however, is smaller because the change in the Brunt-Väisälä frequency caused by changing the electronic mean molecular weight is much more dramatic in the degenerate core. Note that the continuous curve shows a somewhat larger value of the running integral as compared with the two other models for log $q \gtrsim -4$. The difference is significant and is attributed here to the larger value of the effective temperature (T_e = 11,047 K); models with larger effective temperatures but otherwise with the same parameters have larger values of the running integral and, therefore, smaller values of Π_0. This leads to the correlation discussed previously: Π_0 increases with decreasing T_e. If the three models of Figure 41 had had the exact same effective temperature, *no* difference in the curves would have been seen for log $q > -4$.

Because the Brunt-Väisälä frequency is more sensitive to a change of chemical composition in degenerate matter, we can say that Π_0 progressively loses its sensitivity to q(H) as the H/He interface is moved upward in the envelope, i.e., toward less degenerate regions. This observation explains well the qualitative behavior of Π_0 versus T_e in Figures 37 and 38, for example; generally, the spacing between two curves decreases with decreasing q(H). There is one outstanding exception in Figure 37, however. Indeed, the upper curve which characterizes the models with log q(H) = −14 appears not to follow the expected behavior. There is a simple explanation here: the presence of an extensive helium subphotospheric convection zone in these models reduces considerably the extent of the radiative regions, which causes an associated decrease of the integral $\int(N/r)\,dr$ and, hence, an increase of Π_0. We have already pointed out that helium subphotospheric convection zones are significant only for log q(H) $\lesssim -12$ in DA models.

The small effects of subphotospheric convection zones can also be observed in Figure 42, which summarizes our results for the DB models. We show the characteristic period spacing as a function of effective temperature in the range of interest for DBV stars. The data plotted refer to 0.6 $M_\odot$ ML1 models with log q(He) = −2 (*upper continuous curve*), −4 (*middle continuous curve*), −6 (*lower continuous curve*), and −12 (*dashed curve*). For comparison, we have also plotted the results for a 0.6 $M_\odot$ sequence with ML3 convection and log q(He) = −6 (*dotted curve*). In the latter case, significant effects are observed only at the cooler end of the temperature interval illustrated; as for the DA models, the deeper ML3 convection zones reduce the extent of the radiative regions, which causes $\int(N/r)\,dr$ to become smaller as compared with ML1 models. For the same reasons discussed previously, Π_0 is quite insensitive to q(He), varying by only 1 s in the range $-12 \lesssim \log q(\mathrm{He}) \lesssim -2$ at a typical temperature of $T_e \simeq 25{,}000$ K. We note that there is a hint of a very weak dependence of the characteristic period spacing on the mass of the outer helium layer. Indeed, Π_0 decreases very slightly but monotonically with decreasing q(He) in the range $-6 \lesssim \log q(\mathrm{He}) \lesssim -2$ for all effective temperatures of interest. However, this trend is reversed if q(He) keeps decreasing because of the presence of an increasingly significant carbon convection zone under the He/C transition zone in such cases. Overall, this tends to wash out any (if very small) sensitivity of Π_0 to q(He).

In this subsection we have thus determined that the asymptotic period spacing Π_0 is mostly sensitive to total mass,

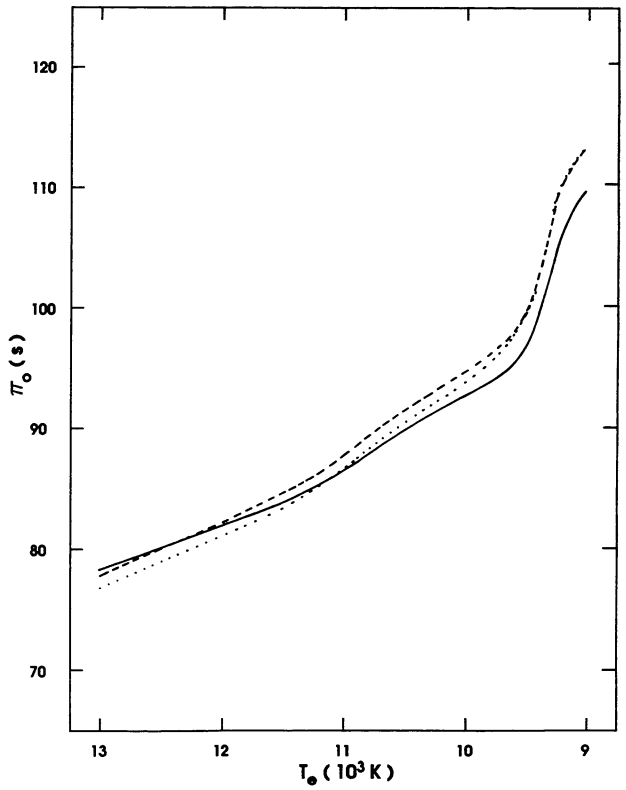

FIG. 40*a*

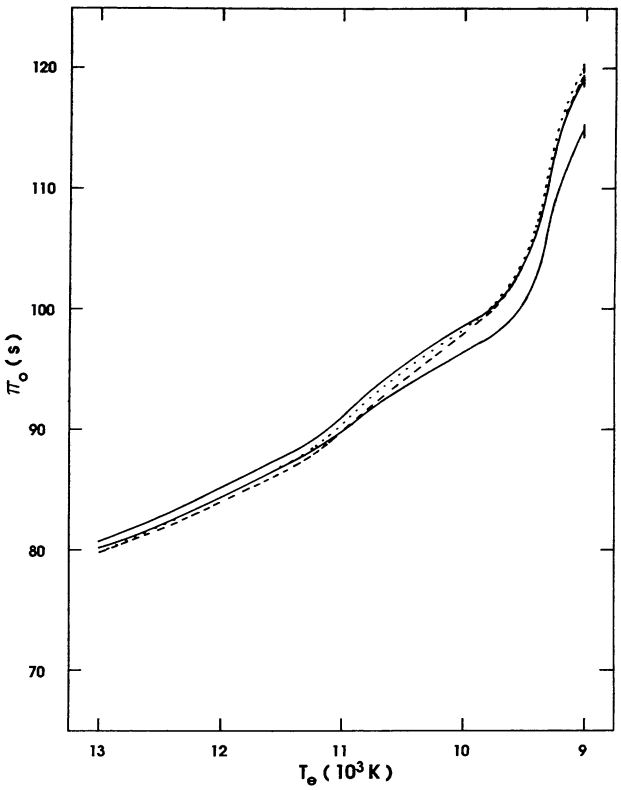

FIG. 40*b*

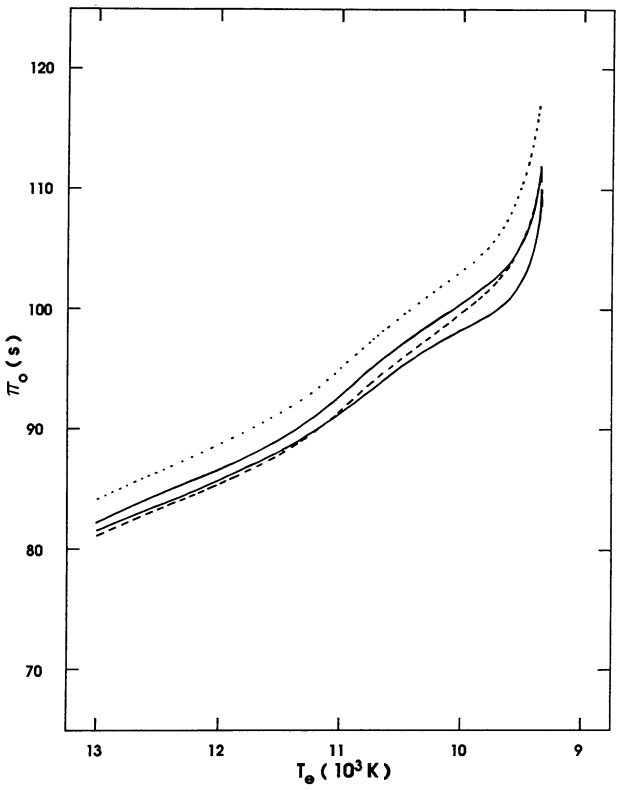

FIG. 40*c*

FIG. 40.—(*a*) Characteristic period spacing vs. effective temperature for evolving 0.6 $M_\odot$ DA models computed with ML1 convection near the DAV instability strip. The models have the same value of the mass of the outer hydrogen layer [log q(H) = −8], and the effects of varying the mass of the helium layer are shown. The continuous, dashed, and dotted curves correspond respectively to models with log q(He) = −2, −4, and −6. (*b*) Same as (*a*), but for models with log q(H) = −10. The lower continuous curve corresponds to models with log q(He) = −2, the upper continuous curve to models with log q(He) = −4, the dashed curve to models with log q(He) = −6, and the dotted curve to models with log q(He) = −8. (*c*) Same as (*a*), but for models with log q(H) = −12. The lower continuous curve corresponds to models with log q(He) = −2, the upper continuous curve to models with log q(He) = −4, the dashed curve to models with log q(He) = −6, and the dotted curve to models with log q(He) = −10.

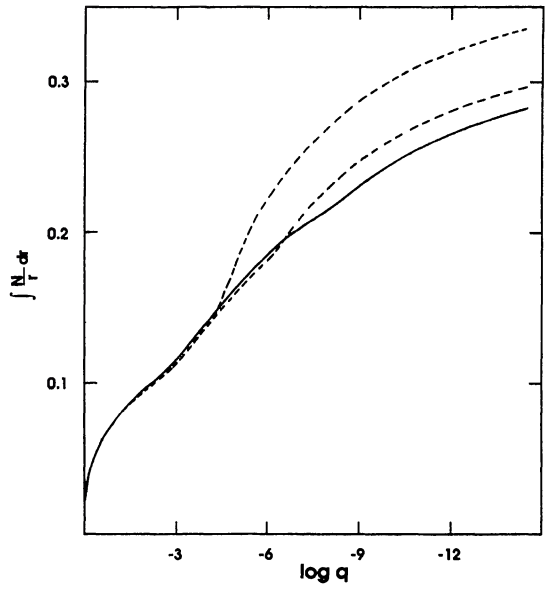

FIG. 41.—Running integral $\int(N/r)\,dr$ vs. mass fraction from the center to the base of the superficial convection zone for three different 0.8 $M_\odot$ DA models computed with ML1 convection. The models have similar effective temperatures and differ by the mass of the outer hydrogen layer. The upper dashed curve corresponds to a model with a thick hydrogen layer [log q(H) = −4], the lower dashed curve to a model with a thinner hydrogen layer [log q(H) = −6], and the continuous curve to a model with yet an even thinner hydrogen layer [log q(H) = −8].

effective temperature, and hydrogen layer mass in models of DA stars. At first sight, this may seem too many parameters for Π_0 to be a useful seismological probe of DAV objects. After all, it was because Π_0 is, by and large, sensitive only to the total mass in DOV stars that Kawaler (1986) was able to obtain a most useful determination of the mass of PG 1159−035. However, in contrast to DO stars, classical model atmosphere techniques coupled to photometry and spectrophotometry (especially in the UV range) can confidently be used to derive quite accurate values of the effective temperatures and surface gravities of DA stars (see, e.g., Holberg, Wesemael, and Basile 1986). Given some reasonable assumption as to the interior composition of these stars, their masses can then be derived from the gravities through the mass-radius relationship. The same considerations apply to DAV stars, which, apart from their pulsations, are quite ordinary DA objects; suitable time-averaged observations are simply required in the determination of their atmospheric parameters. Thus, the potential of Π_0 as a useful seismological probe of DAV stars resides in its sensitivity to q(H). Given a mass and effective temperature, Π_0 (and, in general, the whole period structure of the model) bears essentially the signature of q(H).

As for the DBV stars, our results show that Π_0 is mostly sensitive to two parameters: the effective temperature and the total mass. By contrast to the DA stars, however, atmospheric parameters for these objects are not as well determined. In particular, the temperature scale near the DBV instability strip is still being disputed (see Liebert *et al.* 1986 for a discussion of this). At the same time, evidence has accumulated that DA and DB white dwarfs are two faces of the same objects as surface processes change the dominant atmospheric composition during the evolution (Fontaine and Wesemael

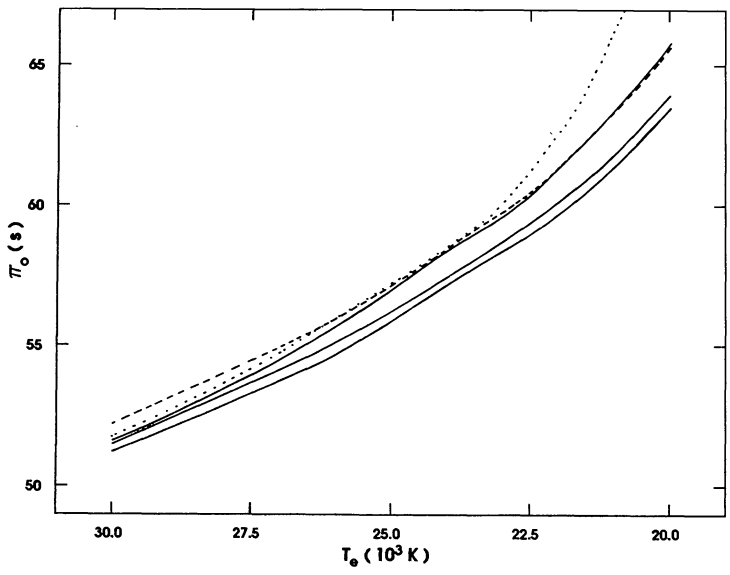

FIG. 42.—Characteristic period spacing vs. effective temperature for evolving 0.6 $M_\odot$ DB models near the DBV instability strip. The continuous curves refer, respectively, to ML1 models with log q(He) = −2, −4, and −6, from top to bottom. The dashed curve refers to ML1 models with log q(He) = −12. The effects of changing the convective efficiency are illustrated by the dotted line, which corresponds to models with log q(He) = −6 and computed with ML3 convection. Note that the vertical scale has been expanded as compared with the previous figures.

1987). The implication is that DB white dwarfs must have the same mass distribution as DA white dwarfs. In that case, the potential usefulness of Π_0 for DBV stars rests with the establishment of a reliable temperature scale for these objects.

IV. CONCLUSION

We have computed a large grid of equilibrium models suitable for seismological investigations of pulsating white dwarfs. Our aim has been to provide a bank of models which can be used to investigate the effects of various parameters on the pulsation properties of the models. By a very large margin over previous efforts, the present investigation remains the most extensive study that has been carried out so far to provide models of pulsating white dwarfs which are as realistic as possible. In essence, our effort is an answer to the need clearly expressed by McGraw (1977, 1979), who was the first to recognize observationally the class of DAV stars. Our models also remain among the few obtained from full evolutionary calculations. As such, they are particularly suited for studies of rates of period change across the white dwarf instability strips. A subset of the present models has already been used by our collaborators and ourselves in various adiabiatic and nonadiabatic pulsation studies of both DAV and DBV stars. However, the grid of models has still not been fully exploited and is being used in further, ongoing, investigations of the properties of these stars. The models are also available to other interested researchers upon request.

Our strategy has been to use a specialized evolution code (employed in the computations of a minimum amount of data) coupled to an interpolation code (used to generate an arbitrary number of shells and compute all the variables needed in adiabatic and nonadiabatic pulsation codes). We have particularly concentrated on the DAV phenomenon by exploring a large volume of parameter space appropriate for DA models. In the process, we have idealized DA white dwarfs as cooling objects with an almost pure carbon core surrounded by an almost pure helium layer, itself surrounded by an almost pure hydrogen layer. It was assumed that diffusive equilibrium is reached in the composition transition zones of these models. In the absence of significant mass loss or accretion, this assumption is justified in most of the envelope ($\log q \lesssim -3$) of a star which has lived long enough to have cooled to effective temperatures characteristic of the DAV instability strip. By concentrating on the evolutionary phases near the DAV strip, we have also been able to ignore physical processes such as neutrino cooling (which dominates the evolution of white dwarfs in the high-luminosity phases) and crystallization effects (which become important at very low luminosities). This approach has prevented us from discussing the general problem of cooling white dwarfs from the planetary nebula stage to the black dwarf stage. At the same time, however, it has allowed us to make efficient use of finite computer resources to explore as large as possible a region of parameter space for DAV models. In the range of luminosities of interest, we have explicitly demonstrated that the basic structural and cooling characteristics of our models compare well with the results of modern evolutionary calculations. A total of 48 independent evolutionary sequences have been calculated for potentially interesting DAV models. For each sequence, a number of models have been retained for subsequent pulsation analysis, and, on the average, those models are spaced by $\Delta T_e \sim 280$ K in the DAV instability strip. This provides excellent sampling of the strip. Good coverage of the observed mass spectrum for isolated white dwarfs has also been achieved by computing evolutionary sequences for $M/M_\odot = 0.4$, 0.6, and 0.8. The mass of the crucial outer hydrogen layer has been varied in the range $-14 \leq \log q(\mathrm{H}) \leq -4$ as imposed by observations and evolution theory. Excellent coverage of this parameter was obtained by computing models with $\log q(\mathrm{H}) = -14, -13, -12, -10, -9, -8, -7, -6$, and -4. Likewise, the effects of varying the mass of the outer helium layer were investigated by computing evolutionary models with $\log q(\mathrm{He}) = -10, -8, -6, -5, -4$, and -2. Another important parameter in the context of DAV stars is the assumed convective efficiency, which determines in large part the location of the driving region. We have calculated models with the ML1, ML2, and ML3 versions of the mixing-length theory (see above). This choice is by no means exclusive but is adequate for studying the effects of convection and for accounting for the actual location of the blue edge of the DAV strip. One special sequence (T60510C1) was computed by arbitrarily decreasing the scale heights of the composition transition zones by a factor of 10. This sequence is important in that it acts as a bridge between models in full diffusive equilibrium (such as those computed here) and models with discontinuous transition zones (such as those obtained in all other evolutionary calculations related to pulsating white dwarfs). Finally, other sequences differing by the use of two different radiative opacity sets available to us for the same compositions were also computed to test the effects of this component of the constitutive physics. Future investigations should concentrate on the effects of varying the core composition (almost pure carbon is assumed here) and the conductive opacities (since the new data of Itoh *et al.* 1983, 1984 are now available). Finally, we have also computed a much less extensive grid of models appropriate for DBV stars, as only eight evolutionary sequences were computed. Those models nevertheless remain the most numerous ones available for studying such stars.

In the discussion of the structural and cooling properties of our white dwarf models, we have been able to demonstrate that the hydrogen outer layer [$\log q(\mathrm{H}) \leq -4$] does not play a role in the intermediate-luminosity phase of the evolution of 0.6 $M_\odot$ DA stars down to a luminosity $\log (L/L_\odot) \simeq -2.6$. Below this value, the hydrogen outer layer begins to play an increasingly important insulating role with decreasing luminosity, to the extent that the core temperatures remain larger for the models with the thicker hydrogen layers. The situation is exactly the opposite for the helium outer layer, since helium is more transparent than hydrogen or carbon in the outer layers of white dwarfs. Thus, models with larger values of $q(\mathrm{He})$ have smaller core temperatures in the range of luminosities where the bulk of the white dwarfs are found.

We have also been able to demonstrate explicitly that cooling is not affected by the uncertainties of mixing-length theory. By contrast, the superficial convection zone structure and, in particular, the location of its base can be quite

sensitive to the free parameters of the theory. We have shown that the thermal time scale in the driving region (located near the base of the superficial convection zone) is mostly sensitive to these parameters. This has the happy consequence that a calibration of the mixing-length theory becomes possible in pulsating white dwarfs. Our models can accommodate a blue edge temperature in the range 13,000 K $\gtrsim T_e \gtrsim$ 10,000 K for DAV stars and in the range 30,000 K $\gtrsim T_e \gtrsim$ 20,000 K for DBV stars, where the ML3 treatment of convection yields the hottest values and the ML1 treatment yields the coolest. A comparison with the observations suggests that ML3 is suitable for both types of pulsating white dwarfs (see Winget *et al.* 1982*a*, 1983; Fontaine, Tassoul, and Wesemael 1984).

The convection zone structure of our models also indicates that the potential for mixing (with the resultant change of surface composition) exists for both types of white dwarfs if $\log q(\mathrm{H}) \lesssim -6$ (DA) or $\log q(\mathrm{He}) \lesssim -6$ (DB). The mixing temperature depends on the mass and the assumed convective efficiency. The 0.6 $M_\odot$ DA models described by ML1 convection gradually turn over into He-rich stars in the range 11,000 K $\gtrsim T_e \gtrsim$ 6000 K if they have a hydrogen layer mass $-14 \lesssim \log q(\mathrm{H}) \lesssim -8$. Such mixing events are required to explain the reversal of the ratio of DA to non-DA white dwarfs in favor of He-rich objects at low effective temperatures. By contrast, the observations strongly suggest that mixing episodes of this sort must be extremely rare events in the life of DB stars. The implication is that $\log q(\mathrm{He}) > -6$ in real DB white dwarfs.

Finally, we have described at some length the evolution of the profiles of several important variables in typical cooling white dwarfs. This provides characteristic values for these variables as well as a detailed qualitative understanding of the main properties of cooling white dwarfs. We have concluded our study by discussing in detail the tool of period spacings provided by asymptotic pulsation theory. We have demonstrated that the characteristic period spacing Π_0 in DAV stars is mostly dependent on the total mass, the effective temperature, and the mass of the outer hydrogen layer; the sensitivity to the other model parameters is much weaker. Given the fact that accurate gravities and effective temperatures can be obtained by model atmosphere techniques for DAV stars, Π_0 could be used as a direct measure of $q(\mathrm{H})$ if uniform period spacings are eventually recognized in the Fourier spectrum of the light curve of one of these stars. It is to be noted that the dependence of Π_0 on $q(\mathrm{H})$ immediately suggests that mode propagation in DAV stars *must* have a sensitivity to $q(\mathrm{H})$. It is therefore not surprising that Winget *et al.* (1982*a*) have found a sensitivity of the blue edge temperature to $q(\mathrm{H})$ in their nonadiabatic studies. As for the DBV stars, the usefulness of Π_0 rests primarily on a possibility of accurately determining the effective temperature, which is less directly obtainable from the usual tools, in contrast to H-rich white dwarfs.

We wish to thank P. Brassard, J. T. McGraw, H. M. Van Horn, and F. Wesemael for stimulating discussions, and J.-L. Tassoul for encouraging us to publish this paper. Special thanks are due to S. Courteau for his essential assistance with the plotting subroutines. We are grateful to M. A. Wood and P. A. Bradley for commenting on the manuscript. Thanks are also due to D. Koester for carefully reviewing this paper. We are also thankful to the Centre de Calcul of the Université de Montréal for generous allotments of computer time. Partial financial support for this work has been provided by the NSERC Canada and by NSF grants AST85-52457 and AST86-00507. One of us (M. T.) also wishes to acknowledge a grant through a program that supports unaffiliated researchers and that is sponsored by the funding agency FCAR (Québec).

REFERENCES

Anthony-Twarog, B. J. 1982, *Ap. J.*, **255**, 245.
Arcoragi, J.-P., and Fontaine, G. 1980, *Ap. J.*, **235**, 534.
Beaudet, G., and Salpeter, E. 1969, *Ap. J.*, **155**, 203.
Beaudet, G., and Tassoul, M. 1971, *Astr. Ap.*, **13**, 209.
Bodenheimer, P., Forbes, J. E., Gould, N. L., and Henyey, L. G. 1965, *Ap. J.*, **141**, 1019.
Böhm, K.-H., and Cassinelli, J. 1971, *Astr. Ap.*, **12**, 21.
Böhm, K.-H., and Stuckl, E. 1967, *Zs. Ap.*, **66**, 487.
Böhm-Vitense, E. 1958, *Zs. Ap.*, **46**, 108.
Bradley, P. A., and Winget, D. E. 1987, *Bull. AAS*, **19**, 1115.
Bradley, P. A., Winget, D. E., and Wood, M. A. 1989, in *IAU Colloquium 114, White Dwarfs*, ed. G. Wegner (New York: Springer), p. 286.
Brassard, P. 1986, M.Sc. thesis, Université de Montréal.
Brassard, P., Fontaine, G., Wesemael, F., and Kawaler, S. D. 1989, in *IAU Colloquium 114, White Dwarfs*, ed. G. Wegner (New York: Springer), p. 263.
Brassard, P., Fontaine, G., Wesemael, F., Tassoul, M., and Kawaler, S. D. 1990, in preparation.
Cox, A. N., Starrfield, S. G., Kidman, R. B., and Pesnell, W. D. 1987, *Ap. J.*, **317**, 303.
Cox, A. N., and Stewart, J. N. 1970, *Ap. J. Suppl.*, **19**, 261.
Cox, J. P. 1980, *Theory of Stellar Pulsation* (Princeton: Princeton University Press).
Cox, J. P., and Giuli, R. T. 1968, *Principles of Stellar Structure* (New York: Gordon & Breach).
D'Antona, F., and Mazzitelli, I. 1979, *Astr. Ap.*, **74**, 161.
_____. 1987, in *IAU Colloquium 95, The Second Conference on Faint Blue Stars*, ed. A. G. D. Philip, D. S. Hayes, and J. Liebert (Schenectady: Davis), p. 635.
Dolez, N., and Vauclair, G. 1981, *Astr. Ap.*, **102**, 375.
Dziembowski, W. 1977, *Acta. Astr.*, **27**, 1.
Dziembowski, W., and Koester, D. 1981, *Astr. Ap.*, **97**, 16.
Fontaine, G. 1973, Ph.D. thesis, University of Rochester.
Fontaine, G., Bergeron, P., Lacombe, P., Lamontagne, R., and Talon, A. 1985, *A.J.*, **90**, 1094.
Fontaine, G., Graboske, H. C., Jr., and Van Horn, H. M. 1977, *Ap. J. Suppl.*, **35**, 293.
Fontaine, G., Kawaler, S. D., Pelletier, C., Wesemael, F., and Winget, D. E. 1990, in preparation.
Fontaine, G., McGraw, J. T., Dearborn, D. S. P., Gustafson, J., and Lacombe, P. 1982, *Ap. J.*, **258**, 651.
Fontaine, G., and Michaud, G. 1979, *Ap. J.*, **231**, 826.
Fontaine, G., Tassoul, M., and Wesemael, F. 1984, in *Proc. 25th Liège Astrophysical Colloquium, Theoretical Problems in Stellar Stability and Oscillations*, ed. A. Noels and M. Gabriel (Liège: Université de Liège), p. 328.
Fontaine, G., and Van Horn, H. M. 1976, *Ap. J. Suppl.*, **31**, 467.
Fontaine, G., and Wesemael, F. 1987, in *IAU Colloquium 95, The Second Conference on Faint Blue Stars*, ed. A. G. D. Philip, D. S. Hayes, and J. Liebert (Schenectady: Davis), p. 319.
Greenstein, J. L. 1982, *Ap. J.*, **258**, 661.
Hansen, C. J., Winget, D. E., and Kawaler, S. D. 1985, *Ap. J.*, **297**, 544.
Harris, M. J., Fowler, W. A., Caughlan, G. R., and Zimmerman, B. A. 1983, *Ann. Rev. Astr. Ap.*, **21**, 165.
Holberg, J. B., Wesemael, F., and Basile, J. 1986, *Ap. J.*, **306**, 629.
Hubbard, W. B., and Lampe, M. 1969, *Ap. J. Suppl.*, **18**, 297.
Huebner, W. F. 1980, private communication.
Iben, I., Jr., and Tutukov, A. V. 1984, *Ap. J.*, **282**, 615.
Itoh, N., Kohyama, Y., Matsumoto, N., and Seki M. 1984, *Ap. J.*, **285**, 758.
Itoh, N., Mitake, S., Iyetomi, H., and Ichimaru, S. 1983, *Ap. J.*, **273**, 774.
Kato, S. 1966, *Pub. Astr. Soc. Japan*, **19**, 1.

Kawaler, S. D. 1986, Ph.D. thesis, University of Texas at Austin.
_____. 1987*a*, in *IAU Colloquium 95, The Second Conference on Faint Blue Stars*, ed. A. G. D. Philip, D. S. Hayes, and J. Liebert (Schenectady: Davis), p. 297.
_____. 1987*b*, in *Stellar Pulsations*, ed. A. N. Cox, W. M. Sparks, and S. G. Starrfield (Berlin: Springer-Verlag), p. 367.
_____. 1987*c*, in *IAU Symposium 123, Advances in Helio- and Asteroseismology*, ed. J. Christensen-Dalsgaard and S. Frandsen (Dordrecht: Reidel), p. 329.
_____. 1988, *Ap. J.*, **334**, 220.
Kawaler, S. D., Winget, D. E., Iben, I., Jr., and Hansen, C. J. 1986, *Ap. J.*, **302**, 530.
Koester, D. 1976, *Astr. Ap.*, **52**, 415.
_____. 1989, in *IAU Colloquium 114, White Dwarfs*, ed. G. Wegner (New York: Springer), p. 206.
Koester, D., and Schönberner, D. 1986, *Astr. Ap.*, **154**, 125.
Koester, D., Schulz, H., and Weidemann, V. 1979, *Astr. Ap.*, **76**, 262.
Koester, D., Vauclair, G., Dolez, N., Oke, J. B., Greenstein, J. L., and Weidemann, V. 1985, *Astr. Ap.*, **149**, 423.
Lamb, D. Q. 1974, Ph.D. thesis, University of Rochester.
Lamb, D. Q., and Van Horn, H. M. 1975, *Ap. J.*, **200**, 306.
Lamontagne, R., Wesemael, F., and Fontaine, G. 1987, in *IAU Colloquium 95, The Second Conference on Faint Blue Stars*, ed. A. G. D. Philip, D. S. Hayes, and J. Liebert (Schenectady: Davis), p. 677.
Liebert, J., Wesemael, F., Hansen, C. J., Fontaine, G., Shipman, H. L., Sion, E. M., Winget, D. E., and Green, R. F. 1986, *Ap. J.*, **309**, 241.
Mazzitelli, I., and D'Antona, F. 1986, *Ap. J.*, **308**, 706.
McGraw, J. T. 1977, Ph.D. thesis, University of Texas at Austin.
_____. 1979, *Ap. J.*, **229**, 203.
Mestel, L. 1952, *M.N.R.A.S.*, **112**, 583.
Muchmore, D. O. 1984, *Ap. J.*, **278**, 769.
Oke, J. B., Weidemann, V., and Koester, D. 1984, *Ap. J.*, **281**, 276.
Osaki, Y., and Hansen, C. J. 1973, *Ap. J.*, **185**, 277.
Paquette, C., Pelletier, C., Fontaine, G., and Michaud, G. 1986, *Ap. J. Suppl.*, **61**, 197.
Pelletier, C. 1986, Ph.D. thesis, Université de Montréal.
Pelletier, C., Fontaine, G., Wesemael, F., Michaud, G., and Wegner, G. 1986, *Ap. J.*, **307**, 242.
Pesnell, W. D. 1987, in *Stellar Pulsations*, ed. A. N. Cox, W. M. Sparks, and S. G. Starrfield (Berlin: Springer-Verlag), p. 363.
Reimers, D., and Koester, D. 1988, *Astr. Ap.*, **202**, 77.
Romanishin, W., and Angel, J. R. P. 1980, *Ap. J.*, **235**, 992.
Saio, H, and Cox, J. P. 1980, *Ap. J.*, **236**, 549.
Saio, H., Winget, D. E., and Robinson, E. L. 1983, *Ap. J.*, **265**, 982..
Schatzman, E. 1958, *White Dwarfs* (Amsterdam: North-Holland).
Shaviv, G., and Kovetz, A. 1976, *Astr. Ap.*, **51**, 383.
Shipman, H. L., and Green, R. F. 1980, *Ap. J. (Letters)*, **239**, L111.
Shipman, H. L., and Sass, C. A. 1980, *Ap. J.*, **235**, 177.
Sion, E. M. 1984, *Ap. J.*, **282**, 612.
Sion, E. M., Greenstein, J. L., Landstreet, J. D., Liebert, J., Shipman, H. L., and Wegner, G. 1983, *Ap. J.*, **269**, 253.
Spiegel, E. 1969, *Comm. Ap. Space Sci.*, **1** (No. 2), 57.
_____. 1972, *Ann. Rev. Astr. Ap.*, **10**, 261.
Starrfield, S. G., Cox, A. N., Hodson, S. W., and Pesnell, W. D. 1982, in *Pulsations in Classical and Cataclysmic Variable Stars*, ed. J. P. Cox and C. J. Hansen (Boulder: University of Colorado Press), p. 78.
Sweeney, M. A. 1976, *Astr. Ap.*, **49**, 375.
Tassoul, M. 1974, Ph.D. thesis, Université de Montréal.
_____. 1980, *Ap. J. Suppl.*, **43**, 469.
Tassoul, M., and Tassoul, J.-L. 1983, *Ap. J.*, **267**, 334.
Truran, J. W., Starrfield, S. G., Strittmatter, P. A., Wyatt, S. P., and Sparks, W. M. 1977, *Ap. J.*, **211**, 539.
Van Horn, H. M. 1968, *Ap. J.*, **151**, 227.
_____. 1971, in *IAU Symposium 42, White Dwarfs*, ed. W. J. Luyten (Dordrecht: Reidel), p. 97.
_____. 1984, in *Proc. 25th Liège Astrophysical Colloquium, Theoretical Problems in Stellar Stability and Oscillations*, ed. A. Noels and M. Gabriel (Liège: Université de Liège), p. 307.
Vauclair, G., and Reisse, C. 1977, *Astr. Ap.*, **61**, 415.
Vauclair, G., Vauclair, S., and Greenstein, J. L. 1979, *Astr. Ap.*, **80**, 79.
Vennes, S., Fontaine, G., and Wesemael, F. 1989, in *IAU Colloquium 114, White Dwarfs*, ed. G. Wegner (New York: Springer), p. 368.
Vennes, S., Pelletier, C., Fontaine, G., and Wesemael, F. 1988, *Ap. J.*, **331**, 876.
Wegner, G. 1979, *A.J.*, **84**, 1384.
Weidemann, V. 1975, in *Problems in Stellar Atmospheres and Envelopes*, ed. B. Baschecck, W. H. Kegel, and G. Traving (Berlin: Springer-Verlag), p. 173.
_____. 1987, *Mem. Soc. Astr. Italiana*, **58**, 33.
Weidemann, V., and Koester, D. 1983, *Astr. Ap.*, **121**, 77.
_____. 1984, *Astr. Ap.*, **132**, 195.
Wesemael, F., Lamontagne, R., and Fontaine, G. 1986, *A.J.*, **91**, 1376.
Winget, D. E. 1981, Ph.D. thesis, University of Rochester.
_____. 1986, in *Highlights Astr.*, ed. J. P. Swings (Dordrecht: Reidel), p. 221.
_____. 1988, in *IAU Symposium 123, Advances in Helio- and Asteroseismology*, ed. J. Christensen-Dalsgaard and S. Frandsen (Dordrecht: Reidel), p. 305.
Winget, D. E., and Fontaine, G. 1982, in *Pulsations in Classical and Cataclysmic Variable Stars*, ed. J. P. Cox and C. J. Hansen (Boulder: University of Colorado Press), p. 46.
Winget, D. E., Hansen, C. J., Liebert, J., Van Horn, H. M., Fontaine, G., Nather, R. E., Kepler, S. O., and Lamb, D. Q. 1987, *Ap. J. (Letters)*, **315**, L77.
Winget, D. E., Robinson, E. L., Nather, R. E., and Fontaine, G. 1982*b*, *Ap. J. (Letters)*, **262**, L11.
Winget, D. E., and Van Horn, H. M. 1987, in *IAU Colloquium 95, The Second Conference on Faint Blue Stars*, ed. A. G. D. Philip, D. S. Hayes, and J. Liebert (Schenectady: Davis), p. 363.
Winget, D. E., Van Horn, H. M., and Hansen, C. J. 1981, *Ap. J. (Letters)*, **245**, L33.
Winget, D. E., Van Horn, H. M., Tassoul, M., Hansen, C. J., and Fontaine, G. 1983, *Ap. J. (Letters)*, **268**, L33.
Winget, D. E., Van Horn, H. M., Tassoul, M., Hansen, C. J., Fontaine, G., and Carroll, B. W. 1982*a*, *Ap. J. (Letters)*, **252**, L65.
Wood, M. A., and Winget, D. E. 1989, in *IAU Colloquium 114, White Dwarfs*, ed. G. Wegner (New York: Springer), p. 282.
Wood, M. A., Winget, D. E., and Van Horn, H. M. 1987, in *IAU Colloquium 95, The Second Conference on Faint Blue Stars*, ed. A. G. D. Philip, D. S. Hayes, and J. Liebert (Schenectady: Davis), p. 639.

G. FONTAINE: Département de Physique, Université de Montréal, C.P. 6128, Succ. A, Montréal, Québec, Canada H3C 3J7

M. TASSOUL: 6000 Chemin Deacon, App. J2, Montréal, Québec, Canada H3S 2T9

D. E. WINGET: Department of Astronomy, University of Texas at Austin, Austin, TX 78642